

2013

Quantum simulations on square and triangular Hubbard models

Kuang-Shing Chen

Louisiana State University and Agricultural and Mechanical College, kchen5@lsu.edu

Follow this and additional works at: https://digitalcommons.lsu.edu/gradschool_dissertations



Part of the [Physical Sciences and Mathematics Commons](#)

Recommended Citation

Chen, Kuang-Shing, "Quantum simulations on square and triangular Hubbard models" (2013). *LSU Doctoral Dissertations*. 86.
https://digitalcommons.lsu.edu/gradschool_dissertations/86

This Dissertation is brought to you for free and open access by the Graduate School at LSU Digital Commons. It has been accepted for inclusion in LSU Doctoral Dissertations by an authorized graduate school editor of LSU Digital Commons. For more information, please contact gradetd@lsu.edu.

QUANTUM SIMULATIONS ON SQUARE AND TRIANGULAR
HUBBARD MODELS

A Dissertation

Submitted to the Graduate Faculty of the
Louisiana State University and
Agricultural and Mechanical College

in partial fulfillment of the
requirements for the degree of
Doctor of Philosophy

in

The Department of Physics and Astronomy

by

Kuang-Shing Chen

B.S., National Taiwan University, 2004

M.S., National Taiwan University, 2006

August 2013

Acknowledgments

During the four years in Louisiana and eight months in Göttingen of my PhD life, I have benefited from many people. Here I would like to acknowledge those who gave me their support.

First, I would like to thank my advisor Dr. Mark Jarrell. He taught me the computational skills using Linux on physics, and gave me an unsurpassed educational resource. Most important of all, the resource in the supercomputing centers is unlimited for a student to "burn!" I also want to thank Dr. Juana Moreno. She is always nice and acts as a coordinator in this large group. I also want to thank Dr. Thomas Pruschke. He gave me a carefree environment to learn the coding skills using c++ when I was in Göttingen.

I would also like to thank to my colleagues in this computing condensed matter group: Shuxiang, Ziyang, Ka-Ming, Peng, Unjong, Karlis, Zhaoxin, Herbert, Peter, Majid, Shi-Quan, Bhupender, Val, Hanna, Chinedu, Ryky, Kalani, Jun, Fei, Sean, Conrad, Xiaoyao, Sheng and Anh, and the friends from Germany: Patrick, Shijie, Andreas, Rene, and Stefan.

My thanks also go to my thesis committee members, Dr. Guoli Ding, Dr. David Yang, Dr. Thomas Pruschke, Dr. Juana Moreno, and Dr. Mark Jarrell. Thank you for your patience and advice.

I also want to thank Ms. Carol A Duran for the prompt help in each "emergency."

Finally, I want to thank my family, my two elder brothers, for the continuing psychological support.

Table of Contents

Acknowledgments	ii
Abstract	v
1 Introduction	1
2 Background and Numerical Method	4
2.1 Introduction to Hubbard Model	4
2.1.1 Definition	4
2.1.2 Noninteracting limit $U = 0$	5
2.1.3 Atomic limit $t = t' = 0$	11
2.1.4 Preview of the interacting case at half filling	13
2.2 DMFT, DMFA and DCA	15
2.2.1 Brief review of the dynamical mean field theory (DMFT)	15
2.2.2 Brief review of the dynamical mean field approximation (DMFA)	15
2.2.3 Dynamical cluster approximation (DCA)	15
2.3 Continuous time quantum Monte Carlo (CTQMC)	21
2.3.1 Formalism	22
2.3.2 Measurement	31
2.3.3 Bethe-Salpeter equation	39
2.3.4 Vertex decomposition	45
2.4 Maximum Entropy Method	46
3 Role of the van Hove Singularity in the Quantum Criticality of the Hubbard Model	52
3.1 Introduction	52
3.2 Formalism	56
3.2.1 Calculation of Single-Particle Spectra	56
3.2.2 d -wave Pairing Susceptibility	57
3.2.3 Transport Coefficients	57
3.3 Results	58
3.3.1 Single Particle Properties for $t' = 0$	58
3.3.2 Pairing Susceptibility	63
3.3.3 Effect of negative t'	65
3.3.4 Transport Properties	66
3.4 Discussion	71
3.5 Conclusion	74
4 Lifshitz Transition in the two-dimension Hubbard Model	75
4.1 Introduction	75

4.2	Formalism	77
4.3	Results	78
4.4	Discussion	84
4.5	Conclusion	88
5	Unconventional Superconductivity on the Triangular Lattice Hubbard Model	90
5.1	Introduction	90
5.2	Formalism	91
5.3	Results	92
5.4	Conclusion	96
6	General Conclusion and Outlook	97
	Bibliography	98
	Appendix	113
	Vita	114

Abstract

In this thesis we try to understand the unconventional superconducting mechanism on cuprates and organic superconductors (or sodium cobaltates) which can be modeled by a two-dimensional square- and triangular-lattice Hubbard model respectively. The formation of the superconducting dome requires explanations of feasible scenarios. Generally speaking, pairing strength is provided by magnetic fluctuations in the strongly correlated region and the structure of the Fermi surface in this region will favor superconducting pairings with a certain type of symmetry.

For the cuprate physics, a superconducting dome composed of d -wave pairings has been identified experimentally. We study the Hubbard model on square lattices and find that the pairing strength is originated from antiferromagnetic instabilities, and the nearly nested Fermi surface with the square symmetry further supports the d -wave pairing. Moreover, our results show there is a quantum critical point (QCP) beneath the superconducting dome. The QCP is a zero-temperature instability which separates the Fermi liquid and pseudogap regions and exhibits the quantum fluctuations which may lead to a high superconducting transition temperature. Above the QCP, a V -shape marginal Fermi liquid region associated with the quantum critical phenomena is also identified. Using next-nearest-neighbor hopping t' , chemical potential, and temperature as control parameters, there is a line of Lifshitz transition associated with the change of topology of the Fermi surface. Along the Lifshitz line with $t' \leq 0$, the marginal Fermi liquid region prevails, the peak of density of states crosses the Fermi level, and the bare d -wave pairing susceptibility shows a universal scaling with the exponent consistent with theoretical proposals.

For the triangular-lattice Hubbard model in the strongly correlated region, we find a $d+id$ superconducting pairing on the hole-doped side of the phase diagram. Here the pairing strength comes from the instabilities of the antiferromagnetic order (120° -spin structure), and the nested hexagon-deformed Fermi surface with the triangular symmetry further boosts the $d+id$ symmetry. Due to the strong competition between electronic interactions and geometric frustrations, the superconductivity and other novel features of the system equal to or above half filling requires future studies.

The numerical tool we apply to study these systems is the dynamical cluster approximation with continuous-time quantum Monte Carlo as the solver. Our approach includes nonlocal correlations embedded in a mean field host and is a most up-to-date and reliable approach in dealing with the above mentioned strongly correlated systems valid in the thermodynamic limit. Our findings shine light on future investigations of the nature of the unconventional superconductivity in the Hubbard model.

Chapter 1

Introduction

Conventional Superconductivity Superconductivity was first discovered in mercury (Hg) in 1911[1]. The first successful theory to explain the superconductivity was proposed by J. Bardeen, L. Cooper and B. Schrieffer[2] in 1957 and is called BCS theory. The keystone of the BCS theory is the concept of Cooper pairs[3] in that an s -wave pair of electrons bonds with its time reversed partners, (\mathbf{k}, \uparrow) and $(-\mathbf{k}, \downarrow)$, in the momentum space and changes the statistics from fermionic to bosonic leading to zero resistance. The Cooper pairs are formed due to the significant rearrangement of the Fermi surface induced by an arbitrarily weak attractive interaction between electrons. Although electrons repel each other due to the Coulomb repulsion, Schrieffer et. al[4] illustrated that the electrons can attract each other due to the electron-ion interactions. Because heavier ions move slower than lighter electrons, after the first electron polarizes the surrounding ions, the first electron goes away but the polarized ionic cloud persists to attract a second electron. Such an indirect attraction between electrons induced by the retarded ions effectively projects the electronic energy scale E_F (Fermi energy) down to the phononic energy scale $\hbar\omega_D$ [5] (ω_D is Debye frequency), which limits the transition temperature T_c to an upper bound ($\sim 28K$)[6] and becomes the foundation of the conventional superconductivity.

Unconventional superconductivity Unconventional superconductivity is generally defined without restricting the pairing state to an isotropic s -wave state and the pairing mechanism is other than the conventional electron-ion interaction[7]. There are various classes of unconventional superconductors such as Helium-3 (3He)[8], heavy fermion superconductors[9], cuprates[10], and organic superconductors[11]. Helium-3 is a neutral fermion which motivates scientists to seek its superconducting phase, because the pairing mechanism of 3He is not possibly caused by the conventional electron-ion interaction. Osheroff et. al[8] discovered a new superconducting phase in 3He at a few milli kelvin with a pairing state originated from many complicated factors (density, spin, transverse current interactions), which opens the horizon of theorists that the pairing of the unconventional superconductivity is not only caused by a single mechanism. The conventional superconducting theory also states that the magnetic impurity or field will break the pairing and kill the superconductivity. However, heavy fermion materials such as $CeCu_2Si_2$ and UPt_3 [9, 12] which contain magnetic f electrons exhibit superconductivity with $T_c \sim 0.5K$. It's intriguing to see that the conduction electron becomes "heavy" at $T \sim T_K$ due to the coupling between the magnetic f electrons, which is the so-called Kondo effect. Such heavy fermions can form various ordered states including d -wave unconventional superconductivity. Before the discovery of cuprates superconductors, Bernd Matthias[13] set down empirical rules of searching for a new super-

conductor or maximizing the T_c for a known superconductor in the late 1950s.¹ The discovery of cuprates breaks the Matthias’ rules in that the parent material is a quasi-2D antiferromagnetic insulator, rather than a 3D cubic transition metal. The transition temperature of cuprates also breaks the upper bound of T_c ($\sim 28K$) of the conventional superconductivity and can go up to $164K$ (under pressure)[14] which is much higher than the boiling point ($77K$) of liquid nitrogen. Such a breakthrough in the transition temperature ignites intense interests both on applications in the industry and on researches of the strongly correlated materials emerging unconventional superconductivity. Organic superconductors like κ -(ET)₂ X family which is a quasi-2D triangular lattice with one spin per site exhibit superconductivity under pressure. Such frustrated materials show a close similarity to Anderson’s RVB (Resonating Valence Bond) picture[15] which predicts the existence of the spin-liquid state, no long range magnetic order in a Mott insulator, as well as the long sought “spinon” Fermi surface[16]. Water-intercalated sodium cobaltates $Na_xCoO_2 \cdot yH_2O$ also have a quasi-2D triangular structure. This material also contains unconventional superconductivity[17].

Outscope In this thesis we will only focus on unconventional superconductivity related to cuprates, organic materials and sodium cobaltates, which can be modeled by the square-lattice and triangular-lattice Hubbard models respectively. Although the Hubbard model cannot describe a complete physics of real materials, at least it captures the dominant physics of our interests. We will briefly introduce the Hubbard model in the section 2.1.

The numerical tool we use for the Hubbard model is the dynamical cluster approximation (DCA, section 2.2.3) with interaction-expansion continuous-time quantum Monte Carlo (INT-CTQMC, section 2.3) as the solver. We obtain one- and two-particle Green’s functions as a function of Matsubara frequency or imaginary time from the DCA+INT-CTQMC, then perform analytic continuation on the one-particle Green’s functions to obtain real-frequency Green’s functions using Maximum Entropy Method (MEM, section 2.4) and analyze the two-particle Green’s functions by solving the Bethe Salpeter equations (section 2.3.3).

For the Hubbard model on the square lattice, our work in section 3 focuses on the scenario proposed by C. M. Varma[18] who has explained that the superconducting mechanism on cuprates may be due to a quantum critical point (QCP) at zero temperature around the optimal doping. The QCP is a zero-temperature instability between two phases where quantum fluctuations exhibit long-range correlations both in space and time[19]. Here in cuprates the QCP separates the Fermi liquid and pseudogap phases. Above the QCP, a V-shape marginal Fermi liquid phase displays the quantum critical scale-invariant particle-hole susceptibility which is weakly dependent on momentum. Varma further proposed that the self energy of the single-particle spectrum which can be observed in angle-resolved photoemission experiments (ARPES) also has weak momentum dependence and is proportional to $max(|\omega|, T)$ which has been proved experimentally[20, 21, 22]. In this thesis we use a large-scale DCA with INT-CTQMC as a solver to explore the physics around the QCP in the square-lattice Hubbard model. We discover that the marginal Fermi liquid phenomena is concomitant with

¹Matthias’ rules based on earlier records of high- T_c materials which were transition metal alloys state that superconducting materials (a) must have d electrons (not just s , p nor f), (b) have high symmetry (cubic is the best), and (c) T_c is maximized if the peak in the density of states is at the Fermi level.

the van-Hove singularity passing through the Fermi level (chapter 3 and ref. [23]). Using temperature, chemical potential, and next-nearest-neighbor hopping as control parameters, we further identify a line of Lifshitz transition associated with the topology of Fermi surface changing from electron-like to hole-like. The peak in the density of states also crosses the Fermi level at the Lifshitz transition line (chapter 4 and ref. [24]). We will show that the relation between the superconducting dome and the Lifshitz line is coupled to a subtle competition between the charge, spin particle-hole channels, the fully-irreducible vertex and the bare d -wave susceptibility.

For the Hubbard model on triangular lattice, we focus on the hole-doped side of the phase diagram and identify the unconventional superconductivity with a $d + id$ pairing in the strong coupling region (section 5 and ref. [25]). Here our interests start from the metal insulator transition (MIT) at half-filling as the electronic interaction increases. Recently, considerable theoretical progress has been made in situations where the MIT takes place between a Fermi liquid (FL) metal and a quantum spin liquid (SL) Mott insulator – a Mott insulating state without any symmetry breaking[15]. Such a quantum critical MIT scenario has acquired experimental relevance due to the discovery of quantum spin liquid Mott insulators near the Mott transition in materials, such as the triangular lattice organic charge transfer salts κ -(BEDT-TTF)₂Cu₂(CN)₃ and EtMe₃Sb[Pd(dmit)₂]₂[26, 27, 28, 29, 30, 31]. By applying hydrostatic pressure, these quantum spin liquids become FL metal, and in between FL and SL there emerges a superconducting phase whose properties such as pairing symmetry are still unknown[32]. Also, there is another material – the water-intercalated sodium cobaltates Na_{*x*}CoO₂·*y*H₂O[17, 33, 34], whose underlying lattice structure is also the geometrically frustrated triangular lattice. A very rich phase diagram has been mapped out for a range of Na concentrations[34], and there is a superconducting dome for $x \sim 0.3$, $y \sim 1.3$ at $T_c \sim 5K$ [17, 33, 34]. The nature of this superconducting phase has also remained poorly understood, but since the underlying triangular lattice belongs to the C_{6v} symmetry group, which allows a doubly degenerate E_2 representation of the superconducting order parameter with $d_{x^2-y^2}$ and d_{xy} degenerate states[35, 36, 37], such a superconducting state might belong to the exciting possibility of a time-reversal symmetry breaking chiral $d_{x^2-y^2} \pm id_{xy}$ superconductor. The low-energy properties of the frustrated organic compounds and cobaltate material may be described by the single-band Hubbard model on the triangular lattice. With the high quality data of the spectral function, self energy, quasiparticle fraction and transport measurements, we are able to estimate the MIT transition point at $U_c/t = 9 \pm 0.5$ at half-filling. In the hole-doped side, due to the interplay of electronic correlations, geometric frustration, and Fermi surface topology, we find possible signature of the $d + id$, doubly degenerate, singlet pairing, superconducting state at an interaction strength close to the bare bandwidth. Such an unconventional superconducting state is mediated by antiferromagnetic spin fluctuations along the Γ - K direction, where the Fermi surface is nested. We furthermore performed an exact decomposition of the irreducible particle-particle vertex to confirm the dominant component of the effective pairing interaction comes from the spin channel.

In the last chapter we will conclude the ideas of unconventional superconductivity on square- and triangular-lattice Hubbard models and propose possible future research topics.

Chapter 2

Background and Numerical Method

2.1 Introduction to Hubbard Model

2.1.1 Definition

Hubbard Model[38] is the simplest model in the study of strongly correlated electronic systems. The model consists of two competing terms: kinetic (hopping particles between sites) and potential terms (on-site Coulomb repulsion). In the following we restrict the particle to be fermion and define the Hamiltonian as:

$$H = -t \sum_{\langle ij \rangle \sigma} (c_{i\sigma}^\dagger c_{j\sigma} + h.c.) - t' \sum_{\langle\langle ij \rangle\rangle \sigma} (c_{i\sigma}^\dagger c_{j\sigma} + h.c.) - \mu \sum_i (n_{i\uparrow} + n_{i\downarrow}) + U \sum_i n_{i\uparrow} n_{i\downarrow}, \quad (2.1)$$

where $c_{i\sigma}^\dagger$ ($c_{i\sigma}$) is the creation (annihilation) operator for electrons with spin σ ($=\uparrow$ or \downarrow) on the site i , $h.c.$ means Hermitian conjugate, $\langle \dots \rangle$ and $\langle\langle \dots \rangle\rangle$ indicate the hopping events between nearest-neighbor and next-nearest-neighbor sites with the corresponding hopping amplitudes t and t' , $n_{i\sigma} = c_{i\sigma}^\dagger c_{i\sigma}$ is the number operator, μ is the chemical potential, and U is the on-site Coulomb repulsion (> 0). The parameter U is associated with the metal-insulator transition (MIT) and a large U (depending on the dimension, cluster size, unit of energy, temperature, ...) leads the system to an insulating phase. The filling $n = 1$ means the half-filled case. At large U , with the bipartite assumption of the lattice and in the Hartree mean-field level, $\langle n_\uparrow \rangle \approx \langle n_\downarrow \rangle \approx 0.5$ means an anti-ferromagnetic background on the ground state. Two bands, the upper Hubbard band and lower Hubbard band, are separated by the Coulomb interaction U and a gap is built between them. No states exist at the Fermi level and no Fermi surface can be defined in the first Brillouin zone.

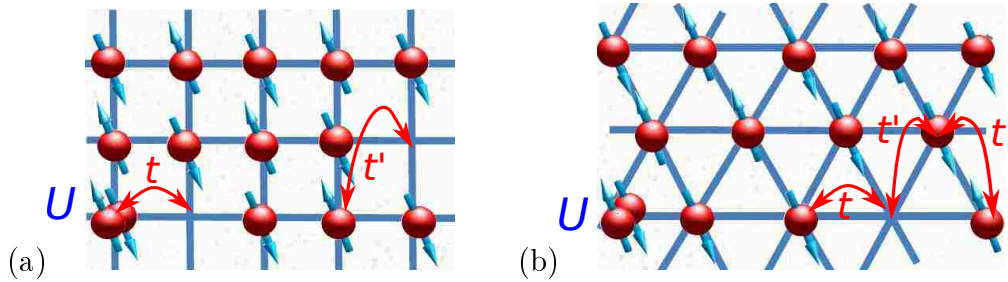


Figure 2.1: Two-dimensional (a) square-lattice and (b) triangular-lattice Hubbard model with U the on-site Coulomb repulsion and t and t' the hopping amplitudes between nearest-neighbor and next-nearest-neighbor sites respectively.

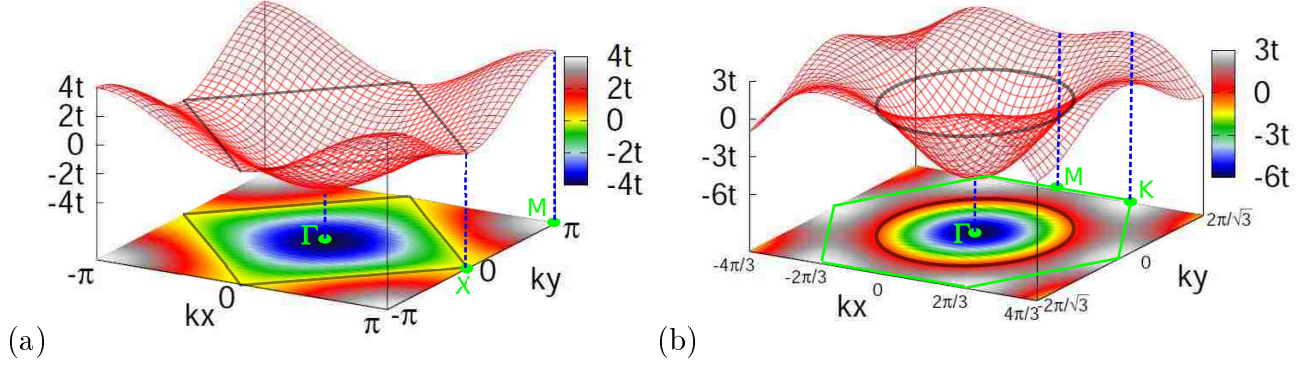


Figure 2.2: Noninteracting dispersions of two-dimensional (a) square-lattice (eq. (2.3) with $t' = 0$) and (b) triangular-lattice (eq. (2.4) with $t' = t$). In (a), $\Gamma = (0,0)$, $M = (\pi, \pi)$, $X = (\pi, 0)$. First Brillouin zone is in the ranges $(k_x, k_y) \in ([-\pi, \pi], [-\pi, \pi])$. The total bandwidth is $8t$, ranges from $-4t$ (at Γ) to $4t$ (at M). The point X is the saddle point with the dispersion value *zero*. In (b), $\Gamma = (0,0)$, $M = (0, \frac{2\pi}{\sqrt{3}})$, and $X = (\frac{2\pi}{3}, \frac{2\pi}{\sqrt{3}})$. First Brillouin zone is the green hexagon. The total bandwidth is $9t$, ranging from $-6t$ (at Γ) to $3t$ (at K). The point M is the saddle point with the dispersion value $2t$. The dark-gray squares in (a) and circles in (b) are the projections of the condition $\epsilon_{\mathbf{k}}^0 = 0$.

2.1.2 Noninteracting limit $U = 0$

If there is no Coulomb interaction ($U = 0$), the Hubbard Hamiltonian depends only on the kinetic term which is associated with the lattice structures. The equation (2.1) in momentum space is

$$H = \sum_{\mathbf{k}\sigma} \epsilon_{\mathbf{k}}^0 c_{\mathbf{k}\sigma}^\dagger c_{\mathbf{k}\sigma} - \mu \sum_i (n_{i\uparrow} + n_{i\downarrow}), \quad (2.2)$$

where $c_{\mathbf{k}\sigma}^\dagger$ ($c_{\mathbf{k}\sigma}$) is the creation (annihilation) operator for electrons with wavevector \mathbf{k} and spin σ , and the bare dispersion is given by (assume lattice constant $a = 1$)

$$\epsilon_{\mathbf{k}}^0 = -2t (\cos k_x + \cos k_y) - 4t' \cos k_x \cos k_y, \quad (2\text{D square lattice}) \quad (2.3)$$

and

$$\epsilon_{\mathbf{k}}^0 = -2t \cos k_x - 4t' \cos\left(\frac{k_x}{2}\right) \cos\left(\frac{\sqrt{3}k_y}{2}\right). \quad (2\text{D triangular lattice}) \quad (2.4)$$

Figure 2.2 shows two-dimensional (2D) square-lattice and triangular-lattice noninteracting dispersions. The filling n is defined as the total states below the Fermi level ($\omega = 0$):

$$\begin{aligned} n &= \frac{2}{L_x L_y} \sum_{\omega \leq 0} \delta(\omega - (\epsilon_{\mathbf{k}}^0 - \mu)) \\ &= \frac{2}{L_x L_y} \sum_{\omega = \epsilon_{\mathbf{k}}^0 - \mu \leq 0} \delta(\omega), \end{aligned} \quad (2.5)$$

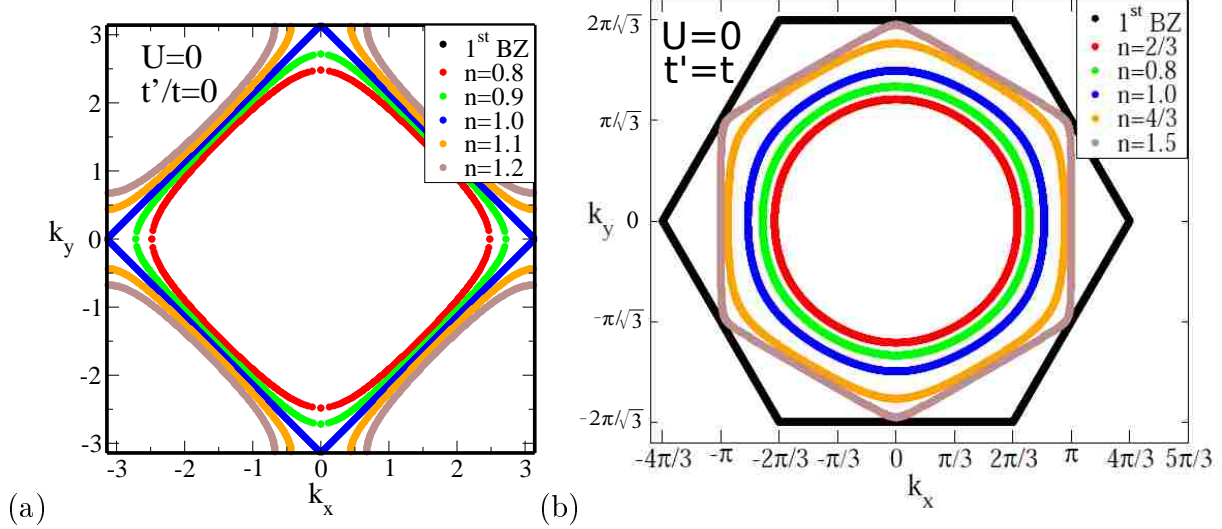


Figure 2.3: Filling dependence of noninteracting Fermi surfaces, or so-called zero-frequency spectra $A(k, \omega = 0)$, for the (a) square lattice with $t'/t = 0$ and the (b) triangular lattice with $t'/t = 1$. In (a), the half-filled Fermi surface is an exact square and the Fermi surfaces become electron-like in the hole-doped ($n < 1$) side and hole-like in the electron-doped ($n > 1$) side. In (b), the Fermi surface grows as the filling increases and starts to deform to a hexagon whose filling is 1.5.

where $L_x L_y$ is the normalization factor, μ is the chemical potential, reference point to the dispersion, and the factor 2 means two spin species. The filling n depends on μ . If $\mu = 0$, according to eq. (2.5), the dark-gray square in Fig. 2.2(a) shows $n = 1$ (half-filled) in the square-lattice dispersion with $t' = 0$ while the dark-gray circle in Fig. 2.2(b) shows $n \approx 0.8$ in the triangular-lattice case with $t'/t = 1$. To obtain a half filling in the triangular-lattice noninteracting dispersion, we need to choose the chemical potential μ roughly equals to $0.8t$. If $\mu \neq 0$, such zero-frequency cuts are the definitions of the Fermi surfaces shown in the Fig. 2.3 with each filling n calculated by the eq. (2.5).

Density of states (DOS) for a single-species spin is defined by

$$N(\omega) = \frac{1}{L_x L_y} \sum_{\mathbf{k} \in BZ} \delta(\omega - (\epsilon_{\mathbf{k}}^0 - \mu)), \quad (2.6)$$

where BZ means the first Brillouin zone defined in the caption of Fig. (2.2). Note that the density of states is normalized to one due to the “single-species” spin. Corresponding to the non-interacting Fermi surfaces in the Fig. 2.3, the DOS with the same parameters are shown in Fig. 2.4. The square-lattice DOS has a particle-hole symmetry at half filling where the peak in the DOS, or so-called van-Hove singularity (vHS), is located at the Fermi level ($\omega = 0$) and the Fermi surface is perfectly nested with the anti-ferromagnetic zone boundary. The peak of DOS in the triangular lattice will pass through the Fermi level when the filling equals to 1.5 with the Fermi surface crossing the saddle point $M = (0, \frac{2\pi}{\sqrt{3}})$.

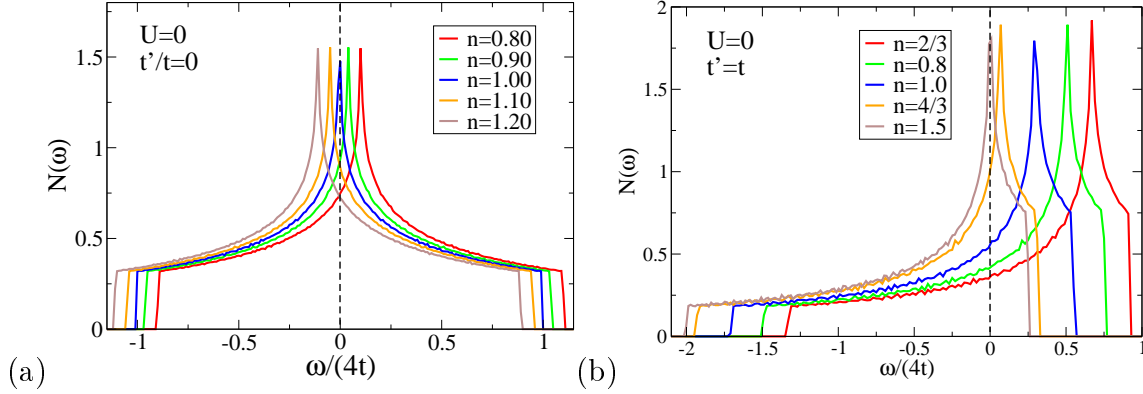


Figure 2.4: Filling dependence of noninteracting density of states for the (a) square lattice with $t'/t = 0$ and (b) triangular lattice with $t'/t = 1$. The peak in the density of states, van-Hove singularity, passes through the Fermi level ($\omega = 0$) at the filling $n = 1$ for the square lattice and $n = 1.5$ for the triangular lattice.

Now we consider the effects of the next-nearest-neighbor hopping t' in the eq. (2.3) and (2.4). We will discuss how t' affects the Fermi surface and DOS both in the square and triangular lattices in a general picture.

Fig. 2.5(a) shows the noninteracting half-filled Fermi surface which changes its topology from hole-like for $t'/t = -0.2$ and -0.1 to electron-like for $t'/t = 0.1$ and 0.2 , and the corresponding DOS in Fig. 2.5(b) displays the vHS moving from left to right of the Fermi level. Physically, the system is energetically favorable for positive t' . The electron prefers next-nearest-neighbor hoppings, and equivalently in the momentum space the electron has a tendency to occupy along $\Gamma - M$ rather than $X(\pi, 0)$, so the Fermi surface becomes “electron-like”. On the flip side, the next-nearest-neighbor hopping of electrons with negative t' costs energy. Relatively speaking, the electron prefers to hop to nearest neighbors, and equivalently the Fermi surface becomes “hole-like” compared to the case with $t' = 0$.

When t' is even larger, the total bandwidth (square: $8t$; triangular: $9t$) of the system also changes, and it is proper to take t' as a new energy unit rather than t . If we increase t'/t from zero, Fig. 2.5(b) shows the DOS becomes asymmetric with its vHS shifting above the Fermi level. When $t'/t = 0.5$ (not shown), the vHS will touch the right edge of the band and bounce back for even larger t'/t with a new bandwidth larger than $8t$. Correspondingly, the Fermi surface in Fig. 2.5(a) changes from a diamond ($t'/t = 0$) to an edge-rounded diamond ($0 < t'/t < 0.5$) and finally becomes a rounded square when $t'/t = 0.5$ shown as the red dotted line in the Fig. 2.5(c). If $t'/t > 0.5$, there is a small Fermi surface centered at $M(\pm\pi, \pm\pi)$ developed because the dispersion energy around M is below the Fermi level. For the extreme case, Fig. 2.5(d) shows the dispersion when $t'/t \rightarrow \infty$ (or $t = 0$) and the first Brillouin zone (BZ) becomes a 45° -rotated smaller square connected by four X points, and the half-filled Fermi surface becomes an even smaller square connected by four X' points. What happens in the real space is that the lattice with only the hopping t' is composed by two independent embedded square lattices with a larger lattice constant $a' = \sqrt{2}a$, and the two independent lattices can be described by two independent and equivalent half-sized BZs

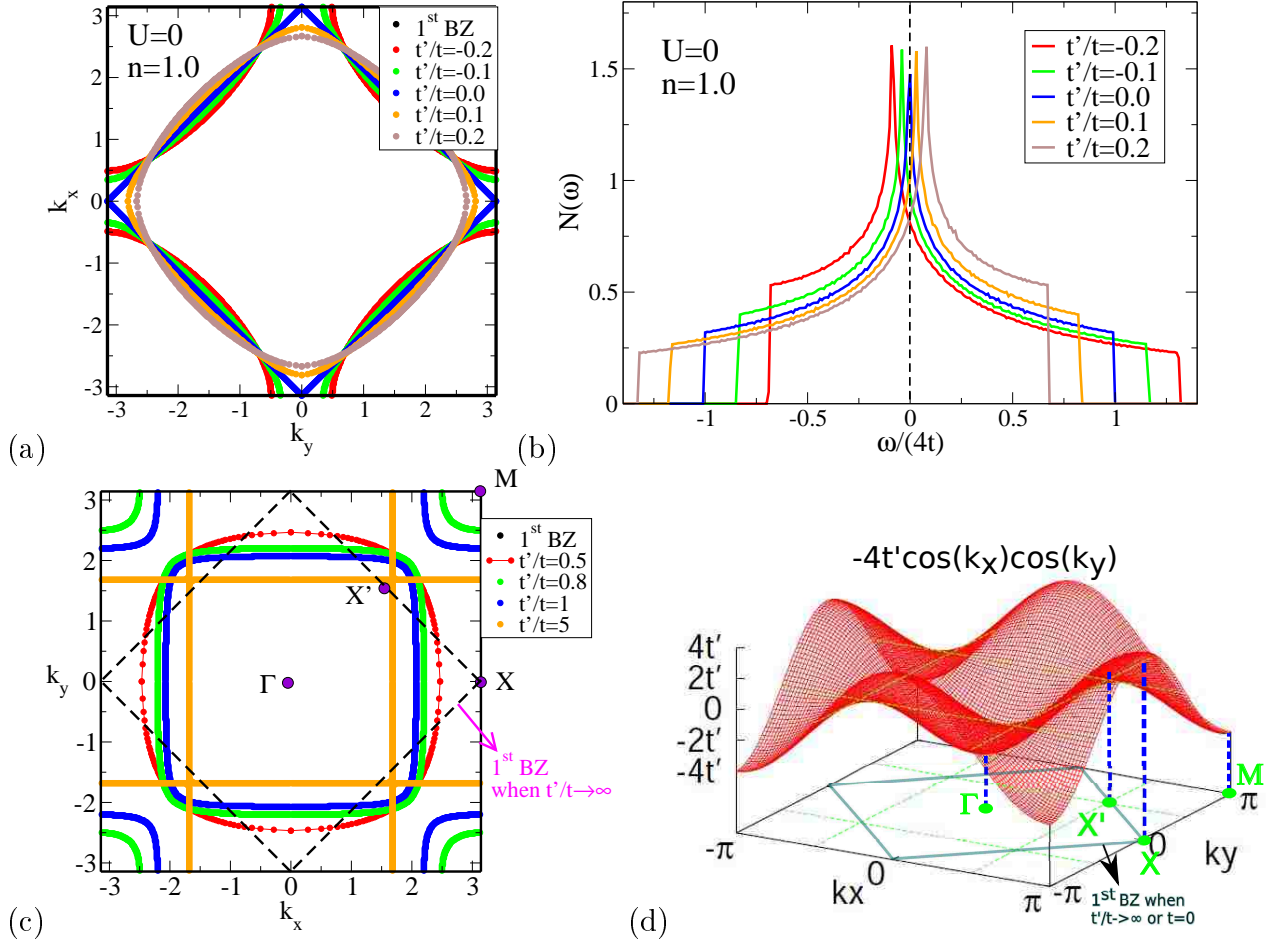
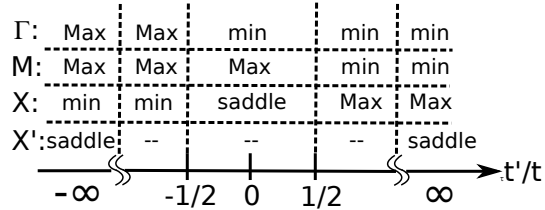


Figure 2.5: Half-filled square-lattice dispersion with the effects of small t' ($= \pm 0.2, \pm 0.1$ and 0) in the (a) Fermi surface and in the (b) density of states and the effects of large and extreme t' in the (c) Fermi surface. The contribution of dispersion solely from the t' term of the eq. (2.3) is plotted in (d).

Table 2.1: Values of noninteracting square-lattice dispersion (eq. (2.3)) and its derivatives at symmetry points $\Gamma(0, 0)$, $M(\pm\pi, \pm\pi)$, $X(\pm\pi, 0)$ or $(0, \pm\pi)$ and $X'(\pm\frac{\pi}{2}, \pm\frac{\pi}{2})$. Footnote \dagger : The values of this column are calculated in a 45° -rotated coordinate $(k'_x, k'_y) = (\frac{k_x - k_y}{\sqrt{2}}, \frac{k_x + k_y}{\sqrt{2}})$, and $X'(\pm\frac{\pi}{2}, \pm\frac{\pi}{2})$ in the coordinate (k_x, k_y) becomes $(\pm\frac{\pi}{\sqrt{2}}, 0)$ and $(0, \pm\frac{\pi}{\sqrt{2}})$ in (k'_x, k'_y) .

	$\Gamma(0, 0)$	$M(\pm\pi, \pm\pi)$	$X(\pm\pi, 0)$	$X(0, \pm\pi)$	$X'(\pm\frac{\pi}{2}, \pm\frac{\pi}{2})^\dagger$
$\epsilon_{\mathbf{k}}^0$	$-4t - 4t'$	$4t - 4t'$	$4t'$	$4t'$	0
$\partial_{k_x}\epsilon_{\mathbf{k}}^0, \partial_{k_y}\epsilon_{\mathbf{k}}^0$	0	0	0	0	$\pm 2\sqrt{2}t$ or 0
$\partial_{k_x}^2\epsilon_{\mathbf{k}}^0$	$2t + 4t'$	$-2t + 4t'$	$-2t - 4t'$	$2t - 4t'$	$\pm 4t'$
$\partial_{k_y}^2\epsilon_{\mathbf{k}}^0$	$2t + 4t'$	$-2t + 4t'$	$2t - 4t'$	$-2t - 4t'$	$\mp 4t'$
$\partial_{k_x}\partial_{k_y}\epsilon_{\mathbf{k}}^0$	0	0	0	0	0



in the momentum space. If we rename $X' \rightarrow X$ and $X \rightarrow M$, rotate the coordinate by 45° , and re-scale lattice constant $a' = 1$ and energy unit $t' \rightarrow t$, the dispersion $-4t' \cos k_x \cos k_y$ becomes $-2t(\cos k_x + \cos k_y)$, which is the eq. (2.3) with $t' = 0$.

Table 2.1 displays how the high symmetry points $\Gamma(0, 0)$, $M(\pm\pi, \pm\pi)$, $X(\pm\pi, 0)$ or $(0, \pm\pi)$ and $X'(\pm\frac{\pi}{2}, \pm\frac{\pi}{2})$ in the square-lattice dispersion change between extreme values and saddle points due to the effect of t'/t . Take an example of $t'/t = 0$ shown in Fig. 2.2(a), the dispersion value in Γ is a minimum, M is a maximum, and X is a saddle point. The other way around the limiting case $t'/t \rightarrow \infty$ in Fig. 2.5(d) shows that the energy value at Γ is still a minimum, M becomes a minimum, X becomes a maximum, and X' is a saddle point. It is when $t'/t = 1/2$ the point M changes its extreme value and X loses the role of saddle point. The point X' becomes a saddle point only when $t = 0$. The value $t'/t = 1/2$ separates two different major properties of the lattice dispersions. When $|t'/t| < 1/2$, the nearest-neighbor hopping t is a dominant hopping strength and the next-nearest-neighbor hopping t' acts as a correction to t' ; when $|t'/t| > 1/2$, t' becomes the major hopping with t being its correction.

The effect of t'/t on the triangular-lattice dispersion is more complicated and interesting. Similar to the square-lattice case, we summarize the results in table 2.2 to show high symmetry points, $\Gamma(0, 0)$, $M_1(0, \pm\frac{2\pi}{\sqrt{3}})$, $M_2(\pm\pi, \pm\frac{\pi}{\sqrt{3}})$, $K_1(\pm\frac{2\pi}{3}, \pm\frac{2\pi}{\sqrt{3}})$ and $K_2(\pm\frac{4\pi}{3}, 0)$, changing their dispersion values as a function of t'/t . Here, there are two special values of $t'/t (= 1/3$ and $2)$ which separate the properties of the dispersion. When $t'/t = 0$, the dispersion (eq. (2.4)) is just $-2t \cos k_x$ which is one-dimensional. When $0 < t'/t < 1/3$, the dispersion is still “1D-like”. It is when $1/3 < t'/t < 2$, the dispersion becomes “triangle-like” with six saddle points (two M_1 and four M_2 points). Especially only when $t'/t = 1$, K_1 and K_2 become maximum and have equal values, and the six saddle points are equivalent in their values as well as their derivatives, in which case it is a so-called isotropic triangular lattice. As

Table 2.2: Values of noninteracting triangular-lattice dispersion (eq. (2.4)) and its derivatives at high symmetry points $\Gamma(0,0)$, $M_1(0, \pm \frac{2\pi}{\sqrt{3}})$, $M_2(\pm\pi, \pm \frac{\pi}{\sqrt{3}})$, $K_1(\pm \frac{2\pi}{3}, \pm \frac{2\pi}{\sqrt{3}})$ and $K_2(\pm \frac{4\pi}{3}, 0)$. Footnote \ddagger : The values of this column are calculated in a $\pm 30^\circ$ -rotated coordinate $(k'_x, k'_y) = (\frac{\sqrt{3}k_x \pm k_y}{2}, \mp k_x + \frac{\sqrt{3}k_y}{2})$, and $M_2(\pm\pi, \pm \frac{\pi}{\sqrt{3}})$ in the coordinate (k_x, k_y) becomes $(\pm \frac{2\pi}{\sqrt{3}}, 0)$ in the corresponding rotated (k'_x, k'_y) .

	$\Gamma(0,0)$	$M_1(0, \pm \frac{2\pi}{\sqrt{3}})$	$M_2(\pm\pi, \pm \frac{\pi}{\sqrt{3}})^\ddagger$	$K_1(\pm \frac{2\pi}{3}, \pm \frac{2\pi}{\sqrt{3}})$	$K_2(\pm \frac{4\pi}{3}, 0)$
$\epsilon_{\mathbf{k}}^0$	$-2t - 4t' < 0$	$-2t + 4t' > 0$	$2t > 0$	$t + 2t' > 0$	$t + 2t' > 0$
$\partial_{k_x} \epsilon_{\mathbf{k}}^0$	0	0	0	$\sqrt{3}(t - t')$	$\sqrt{3}(t' - t)$
$\partial_{k_y} \epsilon_{\mathbf{k}}^0$	0	0	0	0	0
$\partial_{k_x}^2 \epsilon_{\mathbf{k}}^0$	$2t + t' > 0$	$2t - t'$	$-\frac{3}{2}(t + t') < 0$	$-t - \frac{t'}{2} < 0$	$-t - \frac{t'}{2} < 0$
$\partial_{k_y}^2 \epsilon_{\mathbf{k}}^0$	$3t' > 0$	$-3t' < 0$	$\frac{1}{2}(-t + 3t')$	$-\frac{3t'}{2} < 0$	$-\frac{3t'}{2} < 0$

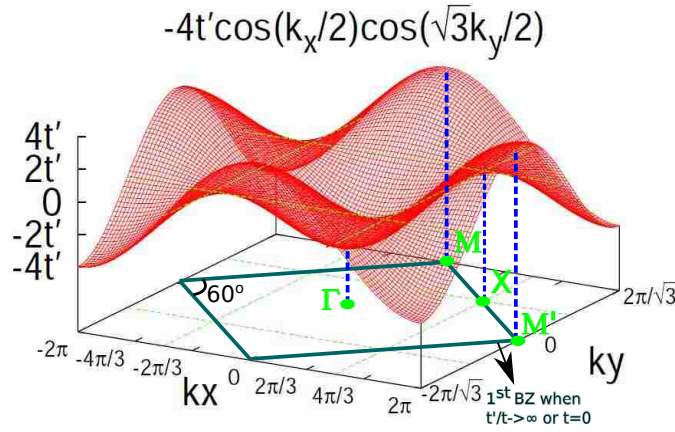
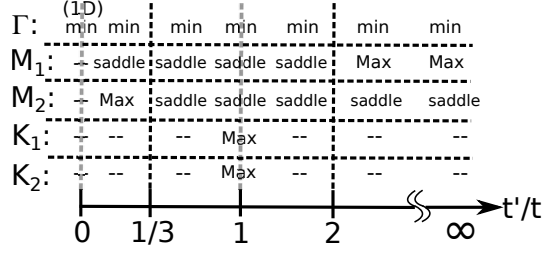


Figure 2.6: Noninteracting triangular dispersion in the case when $t'/t \rightarrow \infty$ with the high symmetry points $\Gamma(0,0)$, $M(0, \pm \frac{2\pi}{\sqrt{3}})$, $M'(\pm 2\pi, 0)$ and $X(\pm\pi, \pm \frac{\pi}{\sqrt{3}})$. The first BZ is the parallelogram with one of the inner angle at 60° .

$t'/t > 2$, we obtain a “square-like” dispersion. Fig. 2.6 shows the dispersion for the extreme case $t'/t \rightarrow \infty$. The first BZ becomes a 60° diamond with high symmetry points defined as $\Gamma(0, 0)$, $M(0, \pm \frac{2\pi}{\sqrt{3}})$, $M'(\pm 2\pi, 0)$ and $X(\pm \pi, \pm \frac{\pi}{\sqrt{3}})$. Note that the bandwidth becomes $8t'$, a bandwidth for the 2D square-lattice dispersion.

In this thesis we will only focus on the effects of small t'/t in the square-lattice Hubbard model with interaction $U = 6t$ (section 3 and 4), and only consider the isotropic case ($t' = t$) in the triangular-lattice Hubbard model (section 5).

2.1.3 Atomic limit $t = t' = 0$

In the atomic limit, the Hubbard Hamiltonian (eq. (2.1)) per site is

$$\frac{H}{N} = U n_\uparrow n_\downarrow - \mu (n_\uparrow + n_\downarrow), \quad (2.7)$$

where N is the number of lattice points. In the following we will take $H/N \rightarrow H$ for simplicity. Choosing $|0\rangle$, $|\uparrow\rangle$, $|\downarrow\rangle$ and $|\uparrow\downarrow\rangle$ as the basis in the Fock space, we can obtain the partition function Z of the Hamiltonian analytically:

$$Z = \text{Tr} e^{-\beta H} = 1 + 2e^{\beta\mu} + e^{-\beta(U-2\mu)}, \quad (2.8)$$

where $\beta = 1/T$, then all the physical quantities such as filling, double occupancy, total energy, local moment, as well as the single-particle Green's function can be obtained. First, the filling is the summation of the particle density for two spin species,

$$\begin{aligned} \langle n \rangle &= \langle n_\uparrow \rangle + \langle n_\downarrow \rangle \\ (\langle n_\uparrow \rangle = \langle n_\downarrow \rangle) &= \frac{2(e^{\beta\mu} + e^{\beta(2\mu-U)})}{1 + 2e^{\beta\mu} + e^{\beta(2\mu-U)}} = \frac{2}{Z} (e^{\beta\mu} + e^{\beta(2\mu-U)}), \end{aligned} \quad (2.9)$$

which increases monotonically as a function of chemical potential μ at high T . The half-filling condition is $\mu = \frac{U}{2}$, resulting in $\langle n \rangle = 1$ which is independent of temperature. When the temperature decreases, $\langle n \rangle$ becomes flat around half filling in the $\langle n \rangle$ - μ curve and finally develops a discontinuity at $\langle n \rangle = 1$ with a jump of μ equal to U when $T \rightarrow 0$.

The double occupancy D is given by

$$D = \langle n_\uparrow n_\downarrow \rangle \quad (2.10)$$

$$= \frac{e^{\beta(2\mu-U)}}{Z} = \frac{1}{e^{-\beta(2\mu-U)} + 2e^{\beta(-\mu+U)} + 1} \quad (2.11)$$

$$= \begin{cases} 0, & \mu < U \\ 1, & \mu > U \end{cases}, T \rightarrow 0. \quad (2.12)$$

The total energy E is just the potential energy, $U \langle n_\uparrow n_\downarrow \rangle = UD$, in the atomic limit because the kinetic energy is zero without the hoppings. The local moment is given by

$$\begin{aligned}
\langle m^2 \rangle &= \langle (n_\uparrow - n_\downarrow)^2 \rangle \\
&= \langle n_\uparrow \rangle + \langle n_\downarrow \rangle - 2 \langle n_\uparrow n_\downarrow \rangle = \langle n \rangle - 2D,
\end{aligned} \tag{2.13}$$

which means that the filling is composed of the local moment and twice of the double occupancy. Finally, the single-particle Green's function under the time translational symmetry is given by (also see eq. (2.33))

$$\begin{aligned}
G^\sigma(\tau) &\equiv -\langle T_\tau c_\sigma(\tau) c_\sigma^\dagger(0) \rangle \\
&= -\frac{1}{Z} (e^{\tau\mu} + e^{\beta\mu + (\mu - U)\tau}),
\end{aligned} \tag{2.14}$$

where $0 \leq \tau < \beta$ and $G^\sigma(0^+) \equiv G^\sigma(0) = 1 - \langle n_\sigma \rangle$ and $G^\sigma(0^-) \equiv -\langle n_\sigma \rangle$. We also obtain the Matsubara Green's function through the Fourier transformation:

$$\begin{aligned}
G^\sigma(i\omega_n) &= \int_0^\beta e^{i\omega_n\tau} G^\sigma(\tau) d\tau \\
&= \frac{1 - \langle n_\sigma \rangle}{i\omega_n + \mu} + \frac{\langle n_\sigma \rangle}{i\omega_n + \mu - U}.
\end{aligned} \tag{2.15}$$

Analytically continuing $G^\sigma(i\omega_n)$ to obtain $G^\sigma(\omega)$ by taking $i\omega_n \rightarrow \omega + 0^+$, and using the definition of spectra $A^\sigma(\omega) \equiv \frac{-1}{\pi} \text{Im} G^\sigma(\omega)$, we obtain the single-species spectra (average over spins) as

$$A(\omega) = \frac{1}{2} (A^\uparrow(\omega) + A^\downarrow(\omega)) \tag{2.16}$$

$$= \frac{1}{2} [(2 - \langle n \rangle) \delta(\omega + \mu) + \langle n \rangle \delta(\omega + \mu - U)]. \tag{2.17}$$

The definition of filling in eq. (2.5) can be defined in terms of the normalized single-species spectra $A(\omega)$:

$$n = 2 \int_{-\infty}^0 d\omega A(\omega) n_F(\omega) \tag{2.18}$$

$$(n_F(\omega) = 1 - \Theta(\omega) \text{ at low } T) = \begin{cases} 0 & \mu < 0 \\ \langle n \rangle = \langle n_\uparrow \rangle + \langle n_\downarrow \rangle = 1, & 0 < \mu < U \\ 2 & \mu > U \end{cases} . \tag{2.19}$$

Here we summarize this section using Fig. 2.7. Eq. (2.13) tells us the filling is composed of the local moment and twice of the double occupancy. We plot those quantities as a function of μ for different temperatures ($T = 10t$, $1t$ and $0.1t$) from left to right of Fig. 2.7. At high temperature ($T = 10t$), the local moment approaches a constant, 0.5. Since

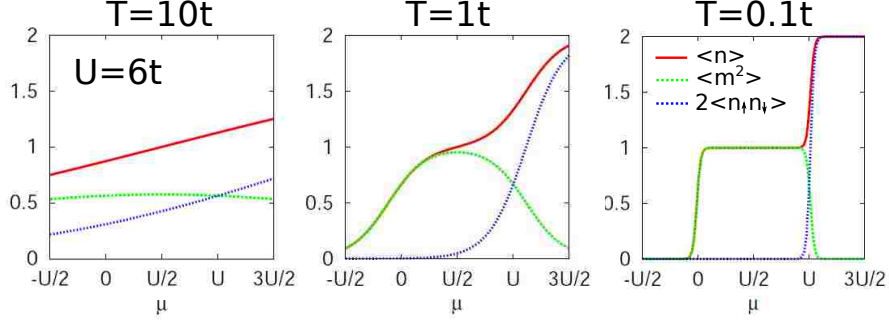


Figure 2.7: Filling $\langle n \rangle$ (eq. (2.9)), local moment $\langle m^2 \rangle$ (eq. (2.13)) and twice of the double occupancy (eq. (2.10)) as a function of chemical potential μ when $T = 10t$, $1t$ and $0.1t$ with an energy unit $t = U/6$.

the eigenvalues of the local moment $\langle m^2 \rangle$ in the basis, $|0\rangle$, $|\uparrow\rangle$, $|\downarrow\rangle$ and $|\uparrow\downarrow\rangle$ are 0, 1, 1, 0 respectively at high T , these four states have equal probability $1/4$ and the local moment equals to $(0+1+1+0)/4 = 0.5$. The filling and the double occupancy increase monotonically with μ at high T . When $T = 1t$, the filling becomes flat around half filling and the local moment starts to increase from 0.5 to 1 near $\mu = U/2$. At low $T(= 0.1t)$, there is a metal-insulator transition (MIT) which is characterized by

- (1) the plateau of μ at half filling with a width of plateau $\Delta\mu = U$,
- (2) the formation of local moment $\langle m^2 \rangle = 1$ when $0 < \mu < U$, and
- (3) zero double occupancy and zero potential energy when $0 < \mu < U$.

In our simulations, we always shift the chemical potential

$$\mu \rightarrow \mu' + U/2 \quad (2.20)$$

to make the Green's function and the normalized spectra symmetric at half filling ($\mu' = 0$, $\langle n_\uparrow \rangle = \langle n_\downarrow \rangle = 1/2$ and $\langle n \rangle = 1$):

$$G^\sigma(\omega) = \frac{1/2}{\omega + \frac{U}{2} + 0^+} + \frac{1/2}{\omega - \frac{U}{2} + 0^+}, \quad (2.21)$$

$$A(\omega) = \frac{1}{2} \left[\delta\left(\omega + \frac{U}{2}\right) + \delta\left(\omega - \frac{U}{2}\right) \right]. \quad (2.22)$$

2.1.4 Preview of the interacting case at half filling

In this section we will combine the results of the noninteracting limit ($U = 0$) in section 2.1.2 and the results of the atomic limit ($t = t' = 0$) in section 2.1.3 to demonstrate the terminology we use in the interacting case with an example in the square-lattice Hubbard model. The Hubbard model with finite Coulomb interaction is

$$H = \sum_{\mathbf{k}\sigma} \epsilon_{\mathbf{k}}^0 c_{\mathbf{k}\sigma}^\dagger c_{\mathbf{k}\sigma} - \mu \sum_i (n_{i\uparrow} + n_{i\downarrow}) + U \sum_i n_{i\uparrow} n_{i\downarrow}. \quad (2.23)$$

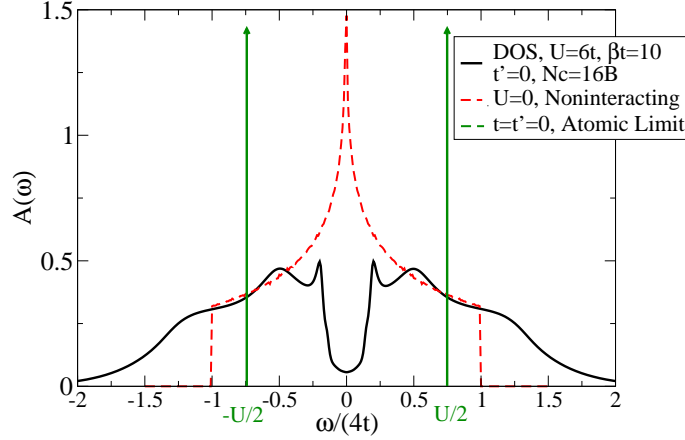


Figure 2.8: Half-filled ($n = 1$) density of states (DOS) for the interacting case with parameters $U = 6t$, $\beta t = 10$, $N_c = 16B$ and $t' = 0$ obtained by DCA+INT-CTQMC (section 2.2.3 and 2.3.1), the noninteracting case with $U = 0$ (section 2.1.2), and the atomic limit ($t = t' = 0$) (section 2.1.3).

And we will use the eq. (2.23) in the formalism part in the sections 3.2, 4.2 and 5.2.

Fig. 2.8 shows the interacting half-filled density of states (DOS) obtained by the DCA+INT-CTQMC (section 2.2.3 and 2.3.1) with parameters $n = 1$, $t' = 0$, $U = 6t$, $\beta t = 10$ and $N_c = 16B$. Together with the noninteracting DOS which exhibits its van Hove singularity at the Fermi level ($\omega = 0$) and the bandwidth $8t$ (also check Fig. 2.3) and the DOS in the atomic limit defined in the eq. (2.22), two delta functions with equal weight separated by the distance U and symmetric with respect to the Fermi level, the interacting DOS is still symmetric with respect to the Fermi level (called particle-hole symmetry), the van Hove singularity at the Fermi level becomes a gap, and two bands, upper Hubbard band (UHB) and lower Hubbard band (LHB), are formed. Note that the chemical potential for the interacting case adopts the convention in the eq. (2.20) for the atomic limit – the chemical potential is zero at half filling.

The filling in the interacting case is twice of the single-species particle density which is defined in the eq. (2.88), and such a filling is similar, in the notion, to the filling for the noninteracting case in the eq. (2.5) and the filling for the atomic limit in the eq. (2.9).

Away from half filling, the chemical potential $\mu \neq 0$, the interacting DOS shifts its center by μ and becomes asymmetric. For the hole-doped ($n < 1$) case, the peak of the LHB becomes a van Hove singularity in the DOS, which is associated with the marginal Fermi liquid phenomena and the quantum critical point (QCP) at $T = 0$, which will be discussed in section 3. Such a crossing peak in the DOS is also associated with the Lifshitz transition, a transition where the Fermi surface changes its topology, and will be discussed in section 4.

2.2 DMFT, DMFA and DCA

2.2.1 Brief review of the dynamical mean field theory (DMFT)

The DMFT[39] is a theory which can treat strongly correlated materials and bridges the gap between the nearly-free electron gas limit (valid for the band theory) and the atomic limit (valid for the density function theory (DFT[40])) of condensed-matter physics. The DMFT maps an original lattice problem into a local impurity problem. Such a mapping is not an approximation. The only approximation comes from the assumption of the momentum-independent (local) self energy. This approximation will become exact in the limit of lattices with an infinite coordination (or dimension).

2.2.2 Brief review of the dynamical mean field approximation (DMFA)

If we assume that the lattice self energy remains local in the finite dimension, the DMFT becomes the DMFA, an “approximation.” The DMFA [41, 42] is a mean-field theory on a single site of a lattice in which the correlations in time are treated explicitly and the correlations in space are taken in a mean-field level, which means that the single-particle self energy is fully local and is independent of the wavevector, $\Sigma \neq \Sigma(k)$. In other words, the DMFA maps the original lattice problem onto a self-consistently embedded and single-site impurity problem. The whole procedure in the self-consistency loop is causal, i.e., it preserves a positive definite spectral weight in the density of states (DOS). This approximation becomes exact in infinite dimensions $D = \infty$ (infinite number of nearest neighbors around a lattice site). Researchers can give numerical results in the thermodynamic limit and in the high dimensional limit[43, 41, 44]. However, in finite dimensions, it is difficult to consider the $1/D$ corrections to the DMFA causally and systematically at the same time. In addition, the physics from the non-local correlations such as pseudo-gap in cuprates, spin waves[45], charge density waves, non-Fermi liquid and d -wave pairing ... etc. cannot be seen in the DMFA. Moreover, the DMFA is not a conserving approximation[45], with violation of the Ward identity associated with current conservation in the equation of continuity in any dimension (including $D \rightarrow \infty$), which leads to a motivation of developing a new theory including the non-local corrections and restores the conservation law.

2.2.3 Dynamical cluster approximation (DCA)

The Dynamical Cluster Approximation (DCA)[46, 47] is a fully causal approach which systematically includes the non-local corrections to the DMFA by mapping the lattice problem onto an embedded periodic cluster of size $N_c = L_c^2$. For $N_c = 1$ the DCA is equivalent to the DMFA and by increasing N_c the dynamic correlation length can be gradually increased while the calculation remains in the thermodynamic limit. For $N_c = \infty$, the DCA becomes exact compared to a real lattice problem. Figure 2.9 shows an example of $N_c = 4$. In the viewpoint of real space (left of Figure 2.9), the total number of the D-dimensional ($D=2$) lattice is N . There are N/N_c clusters with the origin labeled by \tilde{x} , and the $N_c(=4)$ intracluster sites labeled by X . The non-local short-ranged correlations (up to $L_c/2(=1)$ inside a cluster) are treated explicitly, while long-ranged correlations (correlations larger than $L_c/2(=1)$)

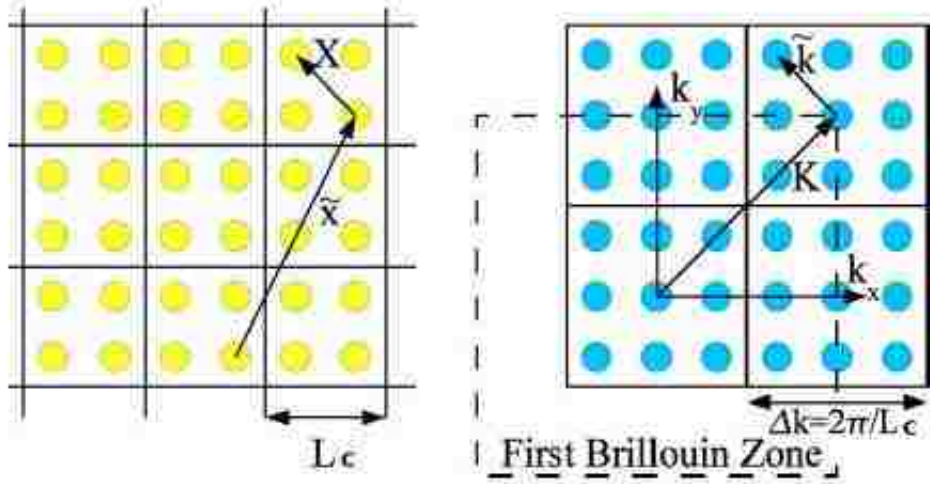


Figure 2.9: Definition of the DCA cluster in the (left) real and (right) reciprocal space for $N_c = 4$. The origin of a cluster is labeled by \tilde{x} , the sites within a cluster by X . The reciprocal space to X is labeled by K , the wave vectors of the superlattice, i.e., within a cell, by \tilde{k} .

are taken as a mean-field (see the coarse-graining procedure in the following text). In the viewpoint of the momentum space (right of Figure 2.9), the first Brillouin zone is divided into $N_c (=4)$ equal cells of linear size $\Delta K (= 2\pi/L_c = \pi)$ labeled by K in their centers, and the momenta within each cell are labeled by \tilde{k} . Non-local correlations of range $\pi/\Delta K (=1)$ are treated explicitly, while correlations smaller than ΔK are coarse-grained like the eq. (2.26). Note that we cannot just take N/N_c clusters composing the original lattice because this statement violates the translational invariance of the lattice. Instead, DCA treats N/N_c clusters composing the first Brillouin zone and what happened in the real space is that the periodic boundary condition is imposed in the cluster. Figure 2.10 demonstrates the example of $N_c = 4$ and large- N_c cases.

Betts[48] selects the cluster geometries according to number of neighbors and the required symmetry. Figure 2.11 shows the examples of square Betts lattices for $N_c=4, 8, 12$ and 16 on the left and triangular Betts lattices for $N_c=3, 4, 6$ and 12 on the right. There are different ways to choose the geometries for a fixed cluster size, and we distinguish them by adding the letter ‘‘A’’, ‘‘B’’, ‘‘C’’... after the cluster number. For example the triangular Betts lattice with $N_c=6C$ contains the high symmetry cluster point $K \equiv (\frac{2\pi}{3}, \frac{2\pi}{\sqrt{3}})$ which is relevant for the anti-ferromagnetic order in the phase diagram. There is no such K point in the lattices with $N_c=6A, 6B$ or $6D$. The reason why we choose the other clusters is similar. According to our purpose, we study $N_c=12A$ and $16B$ for the square-lattice Hubbard model and $N_c=6C$ and $12C$ for the triangular-lattice Hubbard model in this thesis.

The DCA also preserves the translational and point group symmetry of the lattice up to ΔK . Laue function depicts the momentum conservation in each vertex of the Feynman diagram:

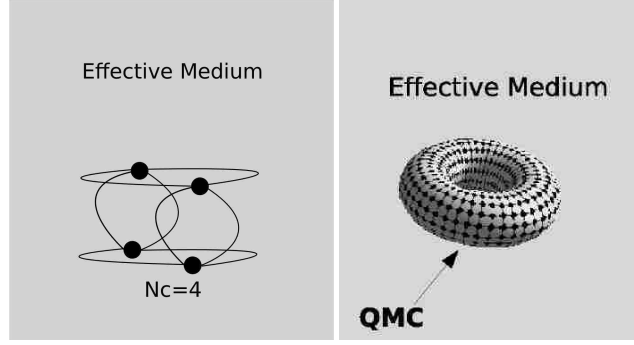


Figure 2.10: DCA maps the infinite lattice problem onto a self-consistently embedded and periodic cluster problem. (left) Example of $N_c = 4$; (right) $N_c \gg 1$.

$$\Delta = \sum_{\mathbf{x}} e^{i\mathbf{x} \cdot (\mathbf{k}_1 - \mathbf{k}_2 - \mathbf{q})} = N \delta_{\mathbf{k}_1, \mathbf{k}_2 + \mathbf{q}}. \quad (2.24)$$

In the DMFA, the Laue function is set to one, $\Delta_{DMFA} = 1$, which means that the incoming and outgoing momentum in each internal vertex becomes independent, and the momentum conservation is completely relinquished. Summing freely over the internal momentum \mathbf{k}_1 and \mathbf{k}_2 does not contain any information about the conservation relation $\mathbf{k}_1 = \mathbf{k}_2 + \mathbf{q}$, but just averages over the first Brillouin zone twice so that the momentum dependent contribution to the free energy is neglected and only the \mathbf{k} -independent (local) term survives. In the DCA, the Laue function is approximated as

$$\Delta_{DCA} = N_c \delta_{\mathbf{K}_1, \mathbf{K}_2 + \mathbf{Q}}, \quad (2.25)$$

which means that the momentum is only conserved and transferred between the N_c cells (with a resolution ΔK), and the N/N_c momentum transferred inside a cell can be summed freely and the conservation relations are neglected (or say, coarse-grained out). In other words, any momentum \mathbf{k} within a momentum cell centered at \mathbf{K} will be mapped to \mathbf{K} , $M(\mathbf{k}) = \mathbf{K}$. Figure 2.12 shows an example of the Feynman diagram in the Hubbard model. Each Green's function leg in the Feynman diagram is replaced by a coarse-grained Green's function:

$$\tilde{G}(M(\mathbf{k})) = \tilde{G}(\mathbf{K}) = \frac{N_c}{N} \sum_{\tilde{\mathbf{k}}} G(\mathbf{K} + \tilde{\mathbf{k}}), \quad (2.26)$$

where $\tilde{\mathbf{k}} = \mathbf{k} - \mathbf{K}$ is the momentum describing the N/N_c sites inside a cell. The DCA also assumes that the self energy depends only on the cluster momentum, $\Sigma(M(\mathbf{k})) = \Sigma_c(\mathbf{K})$. Thus the equation (2.26) can be written as

$$\tilde{G}(\mathbf{K}, z) = \frac{N_c}{N} \sum_{\tilde{\mathbf{k}}} \frac{1}{z - \epsilon_{\mathbf{K} + \tilde{\mathbf{k}}} + \mu - \Sigma_c(\mathbf{K}, z)}, \quad (2.27)$$

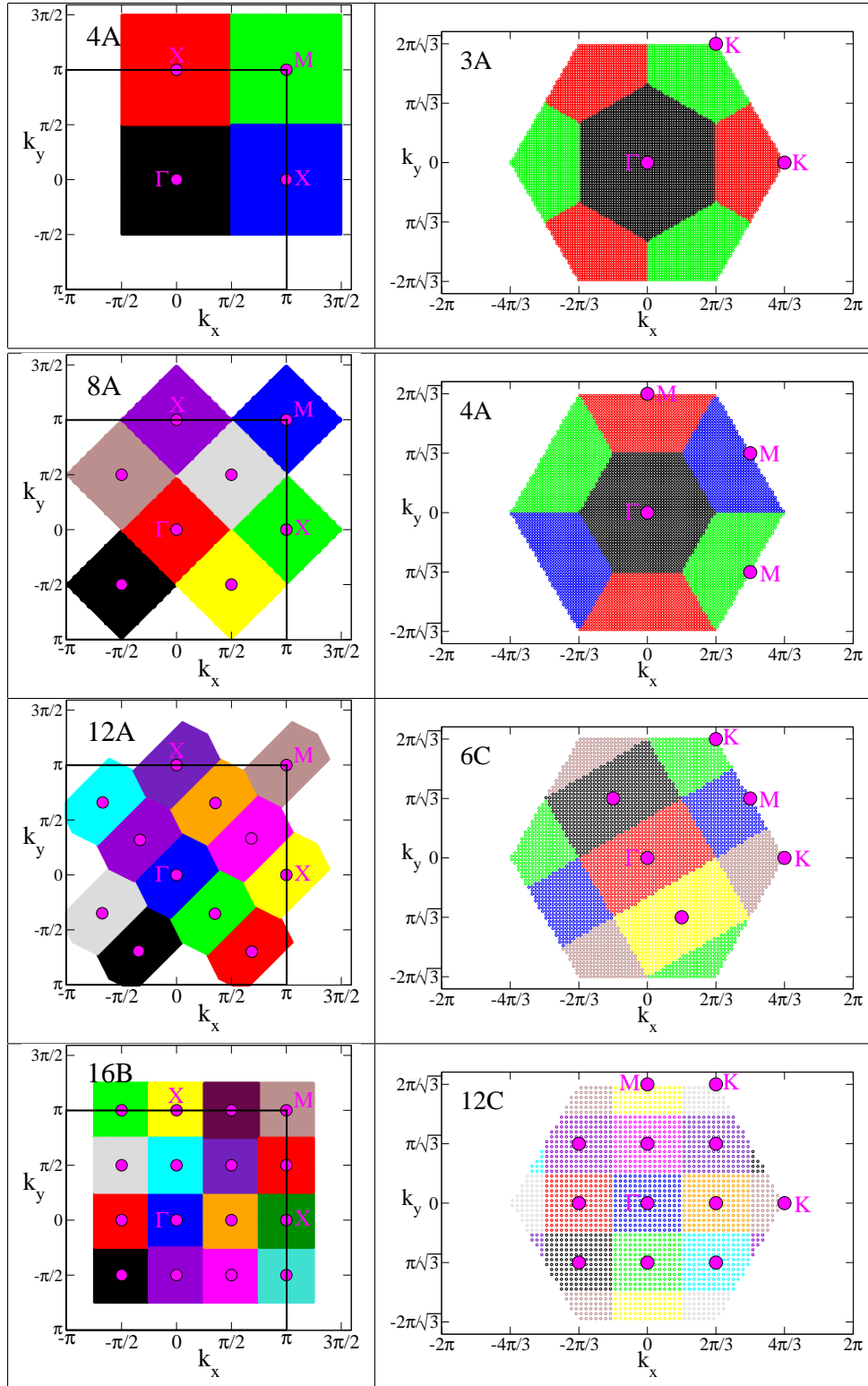


Figure 2.11: (left) Square Betts lattices for $N_c=4A, 8A, 12A$ and $16B$ and (right) triangular Betts lattices for $N_c= 3A, 4A, 6C$ and $12C$.

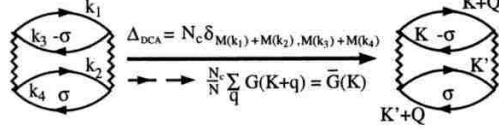


Figure 2.12: A second-order term in the generating functional of the Hubbard model as an example. The wavy line represents the interaction U , and the solid line on the left-hand (right-hand) side is the lattice (coarse-grained) single-particle Green's function G (\bar{G}). With the DCA Laue function, the wave vectors collapse onto those of the cluster and each lattice Green's function is replaced by its coarse-grained average.

which is the self-consistent coarse-graining equation, and z can be the real (ω) or Matsubara frequency ($i\omega_n$).

Figure 2.13 illustrates the procedures in the DCA. The cluster solver sums over all diagrams of Σ_c . To prevent overcounting the diagrams of the cluster self energy, we define the cluster-excluded Green's function

$$g^0(\mathbf{K}, z) = (\bar{G}^{-1}(\mathbf{K}, z) + \Sigma_c(\mathbf{K}, z))^{-1}, \quad (2.28)$$

which excludes the contribution of the cluster self energy from the dressed cluster Green's function. The equilibrium is reached when $|\bar{G}_{n+1} - \bar{G}_n| < \epsilon$, where n is the number of DCA loops. We update the configurations in real space and imaginary time and thus we need to feed $g_R^0(\tau)$ into the cluster solver. In this thesis we choose weak-coupling continuous-time quantum Monte Carlo as the cluster solver shown in section 2.3.

Causal requirement A causal Green's function (or self energy) is defined by its imaginary part being negative definite when the frequency argument is positive, i.e.,

$$\text{Im}G(\mathbf{K}, z) < 0 \text{ (or } \text{Im}\Sigma(\mathbf{K}, z) < 0), \quad (2.29)$$

where $z = \omega > 0$ or $i\omega_n$ with $\omega_n = (2n + 1)\pi T > 0$. The bare or cluster-excluded Green's function also satisfies the causal requirement. For example, the bare Green's function $G^0(\mathbf{K}, i\omega_n) = \frac{1}{i\omega_n - \epsilon_{\mathbf{K}} + \mu}$ and its imaginary part is $\text{Im}G^0(\mathbf{K}, i\omega_n) = \frac{-\omega_n}{(\epsilon_{\mathbf{K}} - \mu)^2 + \omega_n^2} < 0$ when $n \geq 0$, which satisfies the causality. If we perform temporal inverse Fourier transformation (IFT) on the bare Green's function, we obtain

$$\begin{aligned} G^0(\mathbf{K}, \tau) &\equiv T \sum_{n=-\infty}^{\infty} G^0(\mathbf{K}, i\omega_n) e^{-i\omega_n \tau} & (2.30) \\ &= -n_F(-\epsilon_{\mathbf{K}} + \mu) e^{-(\epsilon_{\mathbf{K}} - \mu)\tau}, (0 < \tau < \beta) = n_F(\epsilon_{\mathbf{K}} - \mu) e^{-(\epsilon_{\mathbf{K}} - \mu)\tau}, (-\beta < \tau < 0) \\ &= -\langle c_{\mathbf{K}} c_{\mathbf{K}}^\dagger \rangle_0 e^{-(\epsilon_{\mathbf{K}} - \mu)\tau}, (0 < \tau < \beta) = \langle c_{\mathbf{K}}^\dagger c_{\mathbf{K}} \rangle_0 e^{-(\epsilon_{\mathbf{K}} - \mu)\tau}, (-\beta < \tau < 0) \\ &= -\langle T_\tau c_{\mathbf{K}}(\tau) c_{\mathbf{K}}^\dagger(0) \rangle_0, & (2.31) \end{aligned}$$

which is the corresponding definition of Green's functions in imaginary time with T_τ being the time-ordering operator. After spatially inverse Fourier transforming $G^0(\mathbf{K}, \tau)$, we obtain $G_R^0(\tau)$:¹

$$G_{R=r_i-r_j}^0(\tau-0) \equiv \frac{1}{N_c} \sum_{\mathbf{K}=1}^{N_c} G^0(\mathbf{K}, \tau) e^{-i\mathbf{K}\cdot R} \quad (2.32)$$

$$= - \left\langle T_\tau c_i(\tau) c_j^\dagger(0) \right\rangle_0. \quad (2.33)$$

Unfortunately, the definitions of Green's function in eq. (2.31) and (2.33) are **NOT** the usual conventions in the quantum Monte Carlo (QMC) simulations, because $G^0(\mathbf{K}, \tau)$ and $G_{R=0}^0(\tau)$ are less than zero when $0 < \tau < \beta$. Researchers are getting used to the convention which allows the imaginary-time Green's functions being positive when $\tau \in (0, \beta)$. In this thesis, we adopt such a convention and define the spacial and temporal Green's functions with an extra minus sign shown in eq. (2.47) and (2.48) in the next section. Figure 2.14 gives an example of $g_{R=0}^0(\tau) > 0$ when $0 < \tau < \beta$. At the same time, we also require the Matsubara Green's functions to be causal (eq. (2.29)). Therefore we need to be very careful about the connections between the temporal and Matsubara Green's functions. For example, Fig. 2.13 shows that $G(\mathbf{K}, i\omega_n)$ is measured from the cluster solver based on $g_R^0(\tau)$. In the next section we will show such a measurement is the eq. (2.86), which has an unusual minus sign in front of the matrix derived from $g_R^0(\tau)$. Furthermore, Fig. 2.13 shows that $g^0(K, i\omega_n)$ becomes $g_R^0(\tau)$ under the inverse Fourier transformation. To make up for the different conventions of Green's functions, we add an extra minus sign in the temporal inverse Fourier transformation:

$$g^0(\mathbf{K}, \tau) \equiv -T \sum_{n=-\infty}^{\infty} g^0(\mathbf{K}, i\omega_n) e^{-i\omega_n \tau}. \quad (2.34)$$

Considering the high-frequency condition of $g^0(K, i\omega_n) \sim \frac{1}{i\omega_n}$ (or more precisely $\sim \frac{1}{i\omega_n - \bar{\epsilon}_{\mathbf{K}} + \mu}$, where $\bar{\epsilon}_{\mathbf{K}} \equiv \frac{N_c}{N} \sum_{\tilde{\mathbf{k}}} \epsilon_{\mathbf{K}+\tilde{\mathbf{k}}}$) and also avoiding values overflowed in the exponential, we redefine the temporal inverse Fourier transformation as

$$g^0(\mathbf{K}, \tau \in [0, \beta)) \equiv g_{00} + T \sum_{n=-\infty}^{\infty} e^{-i\omega_n \tau} \left(\frac{1}{i\omega_n - \bar{\epsilon}_{\mathbf{K}} + \mu} - g^0(\mathbf{K}, i\omega_n) \right), \quad (2.35)$$

where

$$g_{00} \equiv \begin{cases} (1 - n_F(\bar{\epsilon}_{\mathbf{K}} - \mu)) e^{-\tau(\bar{\epsilon}_{\mathbf{K}} - \mu)} = \frac{e^{-\tau(\bar{\epsilon}_{\mathbf{K}} - \mu)}}{1 + e^{-\beta(\bar{\epsilon}_{\mathbf{K}} - \mu)}}, & (\bar{\epsilon}_{\mathbf{K}} - \mu \geq 0) \\ n_F(\bar{\epsilon}_{\mathbf{K}} - \mu) e^{(\beta - \tau)(\bar{\epsilon}_{\mathbf{K}} - \mu)} = \frac{e^{(\beta - \tau)(\bar{\epsilon}_{\mathbf{K}} - \mu)}}{1 + e^{\beta(\bar{\epsilon}_{\mathbf{K}} - \mu)}}, & (\bar{\epsilon}_{\mathbf{K}} - \mu < 0) \end{cases}. \quad (2.36)$$

¹The dimension and size of $G_R^0(\tau)$ and $G^0(\mathbf{K}, i\omega_n)$ differ by $\frac{N_c}{T}$ due to the Fourier transformations. If we assume $[G_R^0(\tau)] = 1$, then $[G^0(\mathbf{K}, i\omega_n)] = \frac{N_c}{T}$, which can be taken as inverse of density of energy, m^3/J in the SI unit. This dimensional analysis also applies on G or g^0 . Check footnote 6 for further explanation.

2.3.1 Formalism

A trivial sign problem comes from the positive U : $(-U)^k$ contributes to the k^{th} term in eq. (2.38). To reduce such a sign problem, here we choose $H_b \rightarrow H_{loc}^I$ to be

$$H_{loc}^I = \frac{U}{2} \sum_{i,s=\pm 1} \prod_{\sigma} (n_{i\sigma} - \alpha_{\sigma}(s)), \quad (2.40)$$

where²

$$\alpha_{\sigma}(s) = \frac{1}{2} + \sigma s \left(\frac{1}{2} + 0^+ \right). \quad (2.41)$$

It's easy to see that the difference between eq. (2.39) and eq. (2.40) is only a constant. There is a quick way to check why the equation (2.40) can reduce the sign problem. If we take $s = 1$, then eq. (2.40) becomes $\frac{U}{2}(n_{i\uparrow} - 1 - 0^+)(n_{i\downarrow} + 0^+)$, which is always negative thus it contributes an extra $(-1)^k$ to cancel $(-U)^k$ in the k^{th} term in eq. (2.38). Using this trick, the minus sign problem is completely removed in the one-dimensional case and is highly reduced when the dimension is larger than one.

Let's define the ensemble average $\langle \dots \rangle_o = \text{Tr} [e^{-\beta H_0} \dots] / Z_0$ and $Z_0 = \text{Tr} e^{-\beta H_0}$. A weak coupling diagrammatic expansion yields for the partition function

$$\frac{Z}{Z_0} = \sum_{C_k} \left(\frac{-U}{2} \right)^k \frac{1}{k!} \prod_{\sigma} \langle T_{\tau} (n_{1\sigma} - \alpha_{1\sigma}) (n_{2\sigma} - \alpha_{2\sigma}) \dots (n_{k\sigma} - \alpha_{k\sigma}) \rangle_0, \quad (2.42)$$

$$= \sum_{C_k} \left(\frac{-U}{2} \right)^k \prod_{\sigma} \det D_k^{\sigma}, \quad (2.43)$$

where $C_k = \{[i_1, \tau_1, s_1] \dots [i_k, \tau_k, s_k]\}$, $\sum_{C_k} = \sum_{k=0}^{\infty} \int_0^{\beta} d\tau_1 \sum_{i_1, s_1} \dots \int_0^{\beta} d\tau_k \sum_{i_k, s_k}$, $n_{p\sigma} \equiv n_{i_p\sigma}(\tau_p)$, $\alpha_{p\sigma} \equiv \delta(p-q)\alpha_{p,q\sigma}(s_p) = \delta(i_p - i_q)\delta(\tau_p - \tau_q)\alpha_{\sigma}(s_p) = \delta(i_p - i_q)\delta(\tau_p - \tau_q)(1/2 + \sigma s_p \delta)$ ($p, q \in [1, k]$) and the matrix D_k^{σ} is

$$\begin{pmatrix} \langle T_{\tau} c_{i_1}^{\dagger}(\tau_1) c_{i_1}(\tau_1) \rangle_0 - \alpha_{\sigma}(s_1) & \langle T_{\tau} c_{i_1}^{\dagger}(\tau_1) c_{i_2}(\tau_2) \rangle_0 & \dots & \langle T_{\tau} c_{i_1}^{\dagger}(\tau_1) c_{i_k}(\tau_k) \rangle_0 \\ \langle T_{\tau} c_{i_2}^{\dagger}(\tau_2) c_{i_1}(\tau_1) \rangle_0 & \langle T_{\tau} c_{i_2}^{\dagger}(\tau_2) c_{i_2}(\tau_2) \rangle_0 - \alpha_{\sigma}(s_2) & \ddots & \vdots \\ \vdots & \ddots & \ddots & \vdots \\ \langle T_{\tau} c_{i_k}^{\dagger}(\tau_k) c_{i_1}(\tau_1) \rangle_0 & \dots & \dots & \langle T_{\tau} c_{i_k}^{\dagger}(\tau_k) c_{i_k}(\tau_k) \rangle_0 - \alpha_{\sigma}(s_k) \end{pmatrix}, \quad (2.44)$$

where we assume that D_k^{\uparrow} and D_k^{\downarrow} only differ by α_{σ} , i.e. $\langle T_{\tau} c_i^{\dagger}(\tau) c_j(\tau') \rangle_0$ is spin-independent[50]. Also note that the factorial $k!$ is canceled because we fix a time order $0 \leq \tau_1 < \tau_2 < \dots <$

²Rubtsov et. al[49] found that one should choose $\alpha_{\uparrow} + \alpha_{\downarrow} = 1$ for fermionic systems and $\alpha_{\uparrow} = \alpha_{\downarrow} = \alpha$ for bosonic systems to minimize the minus sign problem. There is no general recipe to give how large the α is when dimension is larger than one.

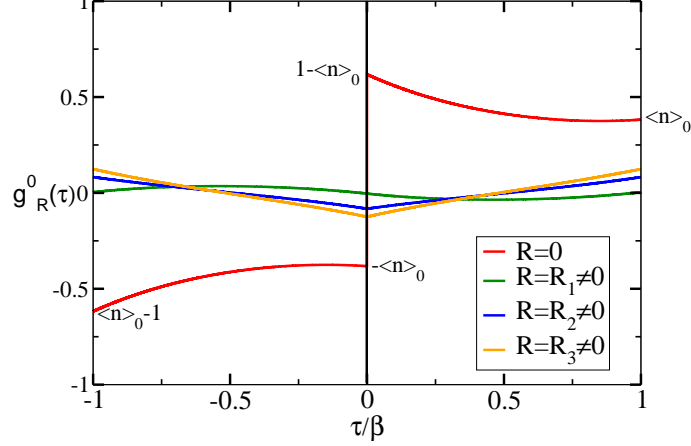


Figure 2.14: Example of the cluster-excluded Green's function $g_R^0(\tau)$ in eq. (2.47). $g_R^0(\tau)$ is discontinuous at $\tau = 0$ only when $R = 0$. All $g_R^0(\tau)$ s satisfy the anti-periodic condition in the eq. (2.49).

$\tau_k \leq \beta$. In other words,

$$\frac{1}{k!} \sum_{C_k} \langle T_\tau \dots \rangle = \frac{1}{k!} \sum_{k=0}^{\infty} \int_0^\beta d\tau_1 \sum_{i_1, s_1} \dots \int_0^\beta d\tau_k \sum_{i_k, s_k} \langle T_\tau \dots \rangle = \sum_{k=0}^{\infty} \int_0^{\tau_2} d\tau_1 \sum_{i_1, s_1} \dots \int_{\tau_{k-1}}^\beta d\tau_k \sum_{i_k, s_k} \langle \dots \rangle. \quad (2.45)$$

Here we define a bare (cluster-excluded) spin-independent Green's function as

$$g_{i,j}^{0\sigma}(\tau_i, \tau_j) = g_{i,j}^0(\tau_i, \tau_j) = \left\langle T_\tau c_i(\tau_i) c_j^\dagger(\tau_j) \right\rangle_0. \quad (2.46)$$

In the following we will write $g_\sigma^0(i, j) \equiv g_{i,j}^{0\sigma}(\tau_i, \tau_j)$ for simplicity. We also define a vertex v_i to be the status of an up and a down electrons doubly occupy at the same space r_i and time τ_i . If two vertexes have equal time, we define the second time argument of Green's function to be slightly greater, i.e. $g_\sigma^0(i, j) \equiv g_{i,j}^{0\sigma}(\tau_i, \tau_j^+)$ if $\tau_i = \tau_j$.³ After applying the translational symmetry in space and time, we obtain

$$g_R^0(\tau) \equiv g_{r_1-r_2}^0(\tau_1 - \tau_2) = \left\langle T_\tau c_R(\tau) c_0^\dagger(0) \right\rangle_0. \quad (2.47)$$

The single-particle Green's function is defined similarly:

³The definition of equal-time Green's function in weak-coupling CTQMC really depends on the expression of the local density. Based on the eq. (2.46), the equal-time Green's function is $g_{i,i}^{0\sigma}(\tau_i, \tau_i^+) = \left\langle T_\tau c_i(\tau_i) c_j^\dagger(\tau_i^+) \right\rangle_0 = - \left\langle c_j^\dagger(\tau_i) c_i(\tau_i) \right\rangle_0$, which equals to $-\langle n_i(\tau_i) \rangle_0$ if $i = j$. In Assaad's and Rubtsov's papers the Green's function is defined as $g_{i,j}^{0\sigma}(\tau_i, \tau_j) \equiv \left\langle T_\tau c_i^\dagger(\tau_i) c_j(\tau_j) \right\rangle_0$. In that case the equal-time Green's function becomes $g_{i,i}^{0\sigma}(\tau_i, \tau_i) \equiv g_{i,i}^{0\sigma}(\tau_i^+, \tau_i) = \left\langle T_\tau c_i^\dagger(\tau_i^+) c_i(\tau_i) \right\rangle_0 = \left\langle c^\dagger(\tau_i) c_i(\tau_i) \right\rangle_0$. These two conventions can be transformed to each other by swapping the space and time indexes (transpose of a matrix) and adding an extra minus sign.

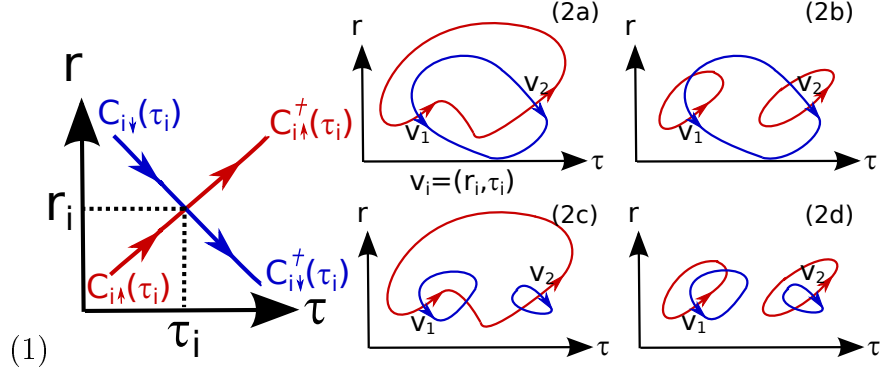


Figure 2.15: Vertices when $k=1$ (1) and $k=2$ (2a)-(2d) in INT-CTQMC.

$$G_R(\tau) \equiv G_{r_1-r_2}(\tau_1 - \tau_2) = \left\langle T_\tau c_R(\tau) c_0^\dagger(0) \right\rangle. \quad (2.48)$$

Both the cluster-excluded (eq. (2.47)) and the single-particle (eq. (2.48)) Green's functions are anti-symmetric in time with period β :

$$g_R^0(\tau) = -g_R^0(\tau + \beta) \quad \text{and} \quad G_R(\tau) = -G_R(\tau + \beta). \quad (2.49)$$

When $R \equiv r_1 - r_2 = 0$, the Green's functions have a discontinuity at $\tau = 0$,

$$g_0^0(0^+) - g_0^0(0^-) = 1 \quad \text{with} \quad g_0^0(0^+) = 1 - \langle n \rangle_0 \quad \text{and} \quad g_0^0(0^-) = -\langle n \rangle_0, \quad (2.50)$$

$$G_0(0^+) - G_0(0^-) = 1 \quad \text{with} \quad G_0(0^+) = 1 - \langle n \rangle \quad \text{and} \quad G_0(0^-) = -\langle n \rangle, \quad (2.51)$$

where $\langle \dots \rangle_0$ denotes the average in the non-interacting bath and n is the local ($r = 0$) density; otherwise when $R \equiv r_1 - r_2 \neq 0$, both Green's functions are continuous at $\tau = 0$, and they still satisfy the anti-periodic condition in the eq. (2.49). Figure 2.14 shows an example of the cluster-excluded Green's function in eq. (2.47). The single-particle Green's functions have similar results.

From the convention of the cluster-excluded Green's function in eq. (2.47), the diagonal elements in the matrix D_k^σ in eq. (2.44) become

$$\begin{aligned} \left\langle T_\tau c_{i_p}^\dagger(\tau_p) c_{i_p}(\tau_p) \right\rangle_0 - \alpha_\sigma(s_p) &= \langle n \rangle_0 - \alpha_\sigma(s_p) \\ &= g_0^0(\beta) - \alpha_\sigma(s_p), \end{aligned} \quad (2.52)$$

where $p \in [1, k]$, and the off-diagonal terms become

$$\left\langle T_\tau c_{i_p}^\dagger(\tau_p) c_{i_q}(\tau_q) \right\rangle_0 = -g_{i_q-i_p}^0(\tau_q - \tau_p), \quad (2.53)$$

Tips for eqs. (2.42)-(2.46): When $k = 1$, there is only one 'vertex', $\langle n_{i\uparrow}(\tau_i) n_{i\downarrow}(\tau_i) \rangle_0$ with $i = 1$, shown in the Fig. 2.15(1). The first contribution Z_1 to the eq. (2.42) can be written as

$\int_0^\beta d\tau_1 \sum_{r_1 s_1 = \pm 1} \left(\frac{-U}{2}\right) \langle T_\tau (n_{1\uparrow}(\tau_1) - \frac{1}{2} - (\frac{1}{2} + 0^+) s_1) \rangle_0 \langle T_\tau (n_{1\downarrow}(\tau_1) - \frac{1}{2} + (\frac{1}{2} + 0^+) s_1) \rangle_0 =$
 $(-U) \int_0^\beta d\tau_1 \sum_{r_1} [\langle n_{1\uparrow}(\tau_1) \rangle_0 \langle n_{1\downarrow}(\tau_1) \rangle_0 - \frac{1}{2} (\langle n_{1\uparrow}(\tau_1) \rangle_0 + \langle n_{1\downarrow}(\tau_1) \rangle_0)] =$
 $(-U) \int_0^\beta d\tau_1 \sum_{r_1} [\langle n_1(\tau_1) \rangle_0 (\langle n_1(\tau_1) \rangle_0 - 1)]$ which is larger than zero because the value in the square bracket is less than zero on the QMC average. In this example we learn that the effect of $\alpha_\sigma(s)$ is really to reduce the minus sign in the odd order (at least $k = 1$) of the partition function.

When $k = 2$, there are two vertexes shown in the Fig. 2.15 and four possible contributions, (2a)-(2d), to the second order partition function Z_2 . Here in terms of the eq. (2.46), (2a) represents $\prod_\sigma (-g^0(1, 2)) (-g^0(2, 1))$, (2b) is

$$\begin{aligned} & - (g_\uparrow^0(1, 1) - \frac{1}{2} - s_1\delta) (g_\uparrow^0(2, 2) - \frac{1}{2} - s_2\delta) (-g_\uparrow^0(2, 1)) (-g_\uparrow^0(1, 2)) \\ = & - (g_{R=0}^0(\beta) - \frac{1}{2} - s_1\delta) (g_{R=0}^0(\beta) - \frac{1}{2} - s_2\delta) (-g^0(2, 1)) (-g^0(1, 2)), \end{aligned}$$

(2c) is

$$\begin{aligned} & - (g_\downarrow^0(1, 1) - \frac{1}{2} + s_1\delta) (g_\downarrow^0(2, 2) - \frac{1}{2} + s_2\delta) (-g_\downarrow^0(2, 1)) (-g_\downarrow^0(1, 2)) \\ = & - (g_{R=0}^0(\beta) - \frac{1}{2} + s_1\delta) (g_{R=0}^0(\beta) - \frac{1}{2} + s_2\delta) (-g^0(2, 1)) (-g^0(1, 2)), \end{aligned}$$

and (2d) is

$$\begin{aligned} & \prod_\sigma (g_\sigma^0(1, 1) - \frac{1}{2} + \sigma s_1\delta) (g_\sigma^0(2, 2) - \frac{1}{2} + \sigma s_2\delta) \\ = & \prod_\sigma (g_{R=0}^0(\beta) - \frac{1}{2} + \sigma s_1\delta) (g_{R=0}^0(\beta) - \frac{1}{2} + \sigma s_2\delta) \end{aligned}$$

where $\delta = \frac{1}{2} + 0^+$, $s_1, s_2 = \pm 1$ and we assume the cluster-excluded Green's function is spin-independent. Note the extra minus sign is shown in (2b) and (2c) because the number of fermion loops is odd (three). These four contributions are the expansion results of the second order in eq. (2.42) based on the Wick's theorem. The summation of these four terms becomes the multiplication of two 2×2 determinants: $\prod_\sigma \det D_2^\sigma$.

where $p, q \in [1, k]$ and if $\tau_p = \tau_q$, the off-diagonal elements are still defined as $g_R^0(\beta^-) \equiv g_R^0(\beta)$ when $R = i_q - i_p$ and $-g_{R'}^0(0^+)$ when $R' = i_p - i_q$ just in case of $R \equiv i_q - i_p = 0$.⁴

Here we are ready to rewrite the matrix D_k^σ in the eq. (2.44) with the notation $g^0(i, j) \equiv g_{i,j}^0(\tau_i, \tau_j)$:

⁴Equal time in the off-diagonal terms (means different vertexes) are rarely happened in the 'continuous' time quantum Monte Carlo. Even if the equal time occurs, there is still no difference for the case of $R \equiv i_q - i_p \neq 0$ because of the continuity of Green's functions at $\tau = 0$ shown in the Fig. 2.14, i.e., $g_R^0(\beta^-) = -g_R^0(0^-) = -g_R^0(0^+)$ for $R \neq 0$. When $R = 0$, it really means that two different vertexes in the expansion order are at the same space and time (almost impossible), and we define the element in the upper-triangular matrix as the local density $\langle n \rangle_0 = g_{R=0}^0(\beta)$ and the element in the lower-triangular matrix as the local density minus one $\langle n \rangle_0 - 1 = -g_{R=0}^0(0^+)$.

$$- \begin{pmatrix} -g_0^0(\beta) + \alpha_\sigma(s_1) & g^0(2,1) & \cdots & g^0(k,1) \\ g^0(1,2) & -g_0^0(\beta) + \alpha_\sigma(s_2) & \ddots & \vdots \\ \vdots & \ddots & \ddots & \vdots \\ g^0(1,k) & \cdots & \cdots & -g_0^0(\beta) + \alpha_\sigma(s_k) \end{pmatrix} \equiv -(\mathbb{D}_k^\sigma)^T, \quad (2.54)$$

where the bold matrix \mathbb{D}_k^σ has elements $(\mathbb{D}_k^\sigma)_{i,i} = -g_0^0(\beta) + \alpha_\sigma(s_i)$ and $(\mathbb{D}_k^\sigma)_{i,j} = g^0(i,j)$ for $i \neq j$. Later we will show that the one-particle and two-particle Green's functions are related to the inversion of the bold matrix \mathbb{D}_k^σ (check the eq. (2.81)).

In the ‘‘Tips for eqs. (2.42)-(2.46)’’ we demonstrate the cases of $k = 1$ and $k = 2$. Generally speaking, $Z_k > 0$ for $U < 0$ for all k . When $U > 0$, $Z_k > 0$ for all k only in the one-dimensional case with the help of the proper α (eq. (2.41)). Some Z_k s are less than zero when the dimension is higher than one. To use the Monte Carlo method, the whole partition function Z is the summation of weights with signs:

$$Z = \sum_{k=0} |Z_k| \text{sgn}_k \quad (2.55)$$

$$= \sum_{k \in \mathcal{C}_k} w(k), \quad (2.56)$$

where $\mathcal{C}_k \equiv \{(r_1, \tau_1, s_1), \dots, (r_k, \tau_k, s_k)\}$ and

$$w(k) = \prod_{i=1}^k d\tau_i \left(\frac{-U}{2}\right)^k \det D_k^\uparrow \det D_k^\downarrow. \quad (2.57)$$

One can update the configuration by adding ($k \rightarrow k+1$) or removing ($k+1 \rightarrow k$) a vertex. Detail balance condition requires

$$P_{add} P(r_{k+1}) P(\tau_{k+1}) P(s_{k+1}) w(k) P_{k \rightarrow k+1} = P_{remove} P(v) w(k+1) P_{k+1 \rightarrow k}, \quad (2.58)$$

where P_{add} and P_{remove} are prior probabilities of adding and removing a vertex and satisfy $P_{add} + P_{remove} = 1$ (Usually we take $P_{add} = P_{remove} = \frac{1}{2}$); $P(r_{k+1})$, $P(\tau_{k+1})$ and $P(s_{k+1})$ are probabilities to add the $(k+1)^{th}$ vertex configuration in space, time, and auxiliary spin, thus we have $P(r_{k+1}) = \frac{1}{N_c}$, $P(\tau_{k+1}) = \frac{d\tau}{\beta}$ and $P(s_{k+1}) = \frac{1}{2}$; $P(v)$ is the probability to remove one vertex among the $(k+1)$ vertexes and thus $P(v) = \frac{1}{k+1}$; $w(k)$ and $w(k+1)$ are according to the eq. (2.57). The Metropolis ratio R_{add} is defined as

$$\begin{aligned} R_{add} &= \frac{P_{k \rightarrow k+1}}{P_{k+1 \rightarrow k}} = \frac{P(v)}{P(r_{k+1}) P(\tau_{k+1}) P(s_{k+1})} \frac{w(k+1)}{w(k)} \\ &= \frac{2N_c \beta}{(k+1) d\tau} \frac{(-U d\tau/2)^{k+1} \det D_{k+1}^\uparrow \det D_{k+1}^\downarrow}{(-U d\tau/2)^k \det D_k^\uparrow \det D_k^\downarrow} \\ &= \frac{-UN_c \beta}{(k+1)} \prod_{\sigma} \frac{\det D_{k+1}^\sigma}{\det D_k^\sigma}. \end{aligned} \quad (2.59)$$

Surprisingly, the factor 2 in the term $(-U/2)$ is canceled by $P(s_{k+1}) = 1/2$. Similarly, the Metropolis ratio to remove $(k \rightarrow k - 1)$ a vertex is

$$R_{rem} = \frac{P_{k \rightarrow k-1}}{P_{k-1 \rightarrow k}} = \frac{-k}{UN_c\beta} \prod_{\sigma} \frac{\det D_{k-1}^{\sigma}}{\det D_k^{\sigma}}. \quad (2.60)$$

We choose a random real number $r \in [0, 1]$. If R_{add} (or R_{rem}) $> r$, we accept the change of adding (or removing) a vertex from order k to $k + 1$ (or $k - 1$); else, we reject the change.

Because it's time consuming to calculate the ratio of determinants. Rubtsov et. al[49] proposed a fast update formula based on the Sherman-Morrison scheme for the determinantal QMC. Such a formula can reduce the computation burden from N^3 to N^2 (N is the linear dimension of a matrix) or less. In the following we will summarize the contents of the fast-update scheme by introducing the identity for the ratio of determinants (assume matrix $M(k) = D(k)^{-1}$ ⁵):

$$\frac{\det D(k+1)}{\det D(k)} = D_{k+1,k+1} - \sum_{i,j=1}^k D_{k+1,i} M(k)_{i,j} D_{j,k+1}, \quad (2.61)$$

and

$$\frac{\det D(k-1)}{\det D(k)} = M_{n,n}, \quad (2.62)$$

where in the eq. (2.62) we remove the n^{th} row and n^{th} column from the $k \times k$ matrix $D(k)$. If we accept the change of adding a vertex, we update the matrix M according to

$$M(k+1) = \begin{pmatrix} & & & -L_{1,k+1}\lambda^{-1} \\ & & & -L_{2,k+1}\lambda^{-1} \\ & & M(k)'_{i,j} & \dots \\ & & & \dots \\ -\lambda^{-1}R_{k+1,1} & \dots & -\lambda^{-1}R_{k+1,k} & \lambda^{-1} \end{pmatrix}, \quad (2.63)$$

where $L_{i,j} = \sum_{l=1}^k M(k)_{i,l} D(k)_{l,j}$, $R_{i,j} = \sum_{l=1}^k D(k)_{i,l} M(k)_{l,j}$, $\lambda = \det D(k+1)/\det D(k) =$ right hand side of eq. (2.61), and $M(k)'_{i,j}$ is defined by

$$M(k)'_{i,j} = M(k)_{i,j} + L_{i,k+1}\lambda^{-1}R_{k+1,j}. \quad (2.64)$$

On the other hand, if we accept the change of removing a vertex, the matrix M is updated by removing the column and row n according to

$$M(k-1)_{i,j} = M(k)_{i,j} - \frac{M(k)_{i,n}M(k)_{n,j}}{M(k)_n}. \quad (2.65)$$

⁵Single argument or one subscript of a matrix means the dimension of the matrix. For example, D_k or $D(k)$ means a $k \times k$ matrix. Double subscripts of a matrix means the index of the matrix. For example, $M(k+1)_{n,m}$ is the matrix element in the n^{th} row and m^{th} column of a $(k+1) \times (k+1)$ matrix M .

Tips for eqs. (2.61) to (2.65): Convince yourself by doing the following example. Let's assume $D(2) = \begin{pmatrix} 1 & 2 \\ -1 & -1 \end{pmatrix}$, so $\det D(2) = 1$ and $M(2) = D(2)^{-1} = \begin{pmatrix} -1 & -2 \\ 1 & 1 \end{pmatrix}$; $D(3) = \begin{pmatrix} 1 & 2 & 1 \\ -1 & -1 & 0 \\ 2 & 0 & 1 \end{pmatrix}$, $\det D(3) = 3$ and $M(3) = D(3)^{-1} = \frac{1}{3} \begin{pmatrix} -1 & -2 & 1 \\ 1 & -1 & -1 \\ 2 & 4 & 1 \end{pmatrix}$. You can see that $D(3)$ is obtained by adding a third column and row to $D(2)$. To test if the eq. (2.61) is true. The left hand side of it is $\det D(3)/\det D(2) = 3$, which is agree with its right hand side:

$$D_{3,3} - (D_{3,1} \ D_{3,2}) \begin{pmatrix} M_{1,1} & M_{1,2} \\ M_{2,1} & M_{2,2} \end{pmatrix} \begin{pmatrix} D_{1,3} \\ D_{2,3} \end{pmatrix} = 1 - (2 \ 0) \begin{pmatrix} -1 & -2 \\ 1 & 1 \end{pmatrix} \begin{pmatrix} 1 \\ 0 \end{pmatrix} = 3 \equiv \lambda.$$

Eqs. (2.63) and (2.64) tell us how to write $M(3)$ in terms of $M(2)$ along with the information from the third column and row of $D(2)$. Since $L_{i,3} = M_{i,l}D_{l,3} = \begin{pmatrix} -1 & -2 \\ 1 & 1 \end{pmatrix} \begin{pmatrix} 1 \\ 0 \end{pmatrix} = \begin{pmatrix} -1 \\ 1 \end{pmatrix}$ and $R_{3,j} = D_{3,l}M_{l,j} = (2 \ 0) \begin{pmatrix} -1 & -2 \\ 1 & 1 \end{pmatrix} = (-2 \ -4)$, thus $M(2)'_{i,j} = M(2)_{i,j} + L_{i,3}\lambda^{-1}R_{3,j} = \begin{pmatrix} -1 & -2 \\ 1 & 1 \end{pmatrix} + \begin{pmatrix} -1 \\ 1 \end{pmatrix} \frac{1}{3} (-2 \ -4) = \frac{1}{3} \begin{pmatrix} -1 & -2 \\ 1 & -1 \end{pmatrix}$. And $M(3)$ can be expressed as

$$M(3) = \begin{pmatrix} \frac{1}{3} \begin{pmatrix} -1 & -2 \\ 1 & -1 \end{pmatrix} & - \begin{pmatrix} -1 \\ 1 \end{pmatrix} \frac{1}{3} \\ - \begin{pmatrix} -2 & -4 \end{pmatrix} \frac{1}{3} & \frac{1}{3} \end{pmatrix} = \frac{1}{3} \begin{pmatrix} -1 & -2 & 1 \\ 1 & -1 & -1 \\ 2 & 4 & 1 \end{pmatrix},$$

which is identical to the known answer $D(3)^{-1}$.

To justify the eq. (2.62), we can start from the $D(3)$ and remove its (a) 1st, (b) 2nd and (c) 3rd column and row. The right hand sites of eq. (2.62) are $M_{1,1} = \frac{-1}{3}$, $M_{2,2} = \frac{-1}{3}$ and $M_{3,3} = \frac{1}{3}$ for the case (a), (b) and (c) respectively, which are agree with the corresponding

left hand sites: (a) $\frac{\det \begin{pmatrix} -1 & 0 \\ 0 & 1 \end{pmatrix}}{\det D(3)} = \frac{-1}{3}$, (b) $\frac{\det \begin{pmatrix} 1 & 1 \\ 2 & 1 \end{pmatrix}}{\det D(3)} = \frac{-1}{3}$ and (c) $\frac{\det \begin{pmatrix} 1 & 2 \\ -1 & -1 \end{pmatrix}}{\det D(3)} = \frac{1}{3}$.

The matrix $M(2)$ in the case (c) is updated, according to eq. (2.65), as

$$\begin{aligned} M(2)_{i,j} &= M(3)_{i,j} - \frac{M(3)_{i,3}M(3)_{3,j}}{M(3)_{3,3}} \\ &= \frac{1}{3} \begin{pmatrix} -1 & -2 & 1 \\ 1 & -1 & -1 \\ 2 & 4 & 1 \end{pmatrix} - \frac{1}{3} \begin{pmatrix} 1 \\ -1 \\ 1 \end{pmatrix} (2 \ 4 \ 1) / 1 = \begin{pmatrix} -1 & -2 & 0 \\ 1 & 1 & 0 \\ 0 & 0 & 0 \end{pmatrix}, \end{aligned}$$

which is agree with the $D(2)^{-1}$. The matrices $M(2)$ s in the case (a) and (b) are obtained in the similar way and the answers are (a) $M(2) = \begin{pmatrix} -1 & 1 \\ 2 & -1 \end{pmatrix}$ and (b) $M(2) = \begin{pmatrix} 1 & 0 \\ 0 & -1 \end{pmatrix}$.

If you don't feel comfortable with the eq. (2.61) to (2.65), please follow "Tips for eqs. (2.61) to (2.65)" for better understandings.

It's also straightforward to generalize the fast update for steps $k \pm 2$ or higher[49]. Here I also summarize all the required formulas and prepare a useful tips in the following. First, the ratio of a $(k + 2) \times (k + 2)$ determinant and a $k \times k$ determinant is

$$\frac{\det D(k+2)}{\det D(k)} \equiv \det \lambda = \det (D_{q,q'} - D_{q,i} M(k)_{i,j} D_{j,q'}), \quad (2.66)$$

where λ is a 2×2 matrix with indexes $q, q' = k + 1, k + 2$ and the matrix $M(k) = D(k)^{-1}$ with index $i, j = 1, 2, \dots, k$. Here summation over repeated indexes is implied. The ratio of a $(k - 2) \times (k - 2)$ determinant and a $k \times k$ determinant is

$$\frac{\det D(k-2)}{\det D(k)} \equiv \det \lambda' = \det M(k)_{q,q'}, \quad (2.67)$$

where $\lambda' \equiv M(k)_{q,q'}$ is also a 2×2 matrix with indexes $q, q' = n, m \in [1, k]$, indicating two columns and rows (n^{th} and m^{th} , $n \neq m$) in the original matrix $D(k)$ are removed. If we would like to add two vertexes, the matrix $M(k + 2)$ is updated according to

$$M(k+2) = \begin{pmatrix} & & & -L_{1,q} \lambda_{q,k+1}^{-1} & -L_{1,q} \lambda_{q,k+2}^{-1} \\ & M(k)'_{i,j} & & \dots & \dots \\ & & & -L_{k,q} \lambda_{q,k+1}^{-1} & -L_{k,q} \lambda_{q,k+2}^{-1} \\ -\lambda_{k+1,q'}^{-1} R_{q',1} & \dots & -\lambda_{k+1,q'}^{-1} R_{q',k} & \lambda_{k+1,k+1}^{-1} & \lambda_{k+1,k+2}^{-1} \\ -\lambda_{k+2,q'}^{-1} R_{q',1} & \dots & -\lambda_{k+2,q'}^{-1} R_{q',k} & \lambda_{k+2,k+1}^{-1} & \lambda_{k+2,k+2}^{-1} \end{pmatrix}, \quad (2.68)$$

$$M(k)'_{i,j} = M(k)_{i,j} + L_{i,q} \lambda_{q,q'}^{-1} R_{q',j}, \quad (2.69)$$

$$L_{i,q} = M(k)_{i,l} D(k)_{l,q}, \quad (2.70)$$

$$R_{q',j} = D(k)_{q',l} M(k)_{l,j}, \quad (2.71)$$

On the flip side, to remove two vertexes ($n \neq m$), the matrix $M(k - 2)$ is updated based on $M(k)$ as

$$M(k-2)_{i,j} = M(k)_{i,j} - \frac{M(k)_{i,q} M(k)_{q',j}}{M(k)_{q,q'}}. \quad (2.72)$$

It's trivial to see that $M(k-2)_{q_1, q_2 = n, m} = 0$ because the right hand side of the eq. (2.72) becomes

$$M(k)_{q_1, q_2} - \frac{M(k)_{q_1, q} M(k)_{q', q_2}}{M(k)_{q, q'}} = M(k)_{q_1, q_2} - \delta_{q_1, q'} M(k)_{q', q_2} = 0. \quad (2.73)$$

Tips for eqs. (2.66) to (2.72): Here we also assume $D(2) = \begin{pmatrix} 1 & 2 \\ -1 & -1 \end{pmatrix}$,

$$\det D(2) = 1 \text{ and } M(2) = D(2)^{-1} = \begin{pmatrix} -1 & -2 \\ 1 & 1 \end{pmatrix}. \quad D(4) = \begin{pmatrix} 1 & 2 & 1 & -1 \\ -1 & -1 & 0 & 1 \\ 2 & 0 & 1 & 0 \\ 1 & -1 & 1 & 2 \end{pmatrix}$$

by adding the 3rd and 4th columns and rows to $D(2)$; $\det D(4) = 3$ and $M(4) =$

$$D(4)^{-1} = \frac{1}{3} \begin{pmatrix} -1 & -3 & 0 & 1 \\ 1 & -3 & -3 & 2 \\ 2 & 6 & 3 & -2 \\ 0 & -3 & -3 & 3 \end{pmatrix}. \quad \text{Again first we test the left hand side of eq.}$$

(2.66): $\det D(4)/\det D(2) = 3$, which is agree with the determinant of the matrix λ :

$$\det \begin{pmatrix} D_{33} - (D_{31} D_{32}) \begin{pmatrix} M_{11} & M_{12} \\ M_{21} & M_{22} \end{pmatrix} \begin{pmatrix} D_{13} \\ D_{23} \end{pmatrix} & D_{34} - (D_{31} D_{32}) \begin{pmatrix} M_{11} & M_{12} \\ M_{21} & M_{22} \end{pmatrix} \begin{pmatrix} D_{14} \\ D_{24} \end{pmatrix} \\ D_{43} - (D_{41} D_{42}) \begin{pmatrix} M_{11} & M_{12} \\ M_{21} & M_{22} \end{pmatrix} \begin{pmatrix} D_{13} \\ D_{23} \end{pmatrix} & D_{44} - (D_{41} D_{42}) \begin{pmatrix} M_{11} & M_{12} \\ M_{21} & M_{22} \end{pmatrix} \begin{pmatrix} D_{14} \\ D_{24} \end{pmatrix} \end{pmatrix}$$

$$= \det \begin{pmatrix} 3 & 2 \\ 3 & 3 \end{pmatrix} = 3. \quad \text{The inversion of } \lambda \text{ is } \frac{1}{3} \begin{pmatrix} 3 & -2 \\ -3 & 3 \end{pmatrix}. \quad \text{Before updating } M(4), \text{ we}$$

need to construct the matrices $L_{i,q}$ and $R_{q',j}$ defined in eqs. (2.70) and (2.71): $L_{i,q} =$

$$M(2)_{i,l} D(2)_{l,q} = \begin{pmatrix} -1 & -2 \\ 1 & 1 \end{pmatrix} \begin{pmatrix} 1 & -1 \\ 0 & 1 \end{pmatrix} = \begin{pmatrix} -1 & -1 \\ 1 & 0 \end{pmatrix} \text{ and } R_{q',j} = D(2)_{q',l} M(2)_{l,j} =$$

$$\begin{pmatrix} 2 & 0 \\ 1 & -1 \end{pmatrix} \begin{pmatrix} -1 & -2 \\ 1 & 1 \end{pmatrix} = \begin{pmatrix} -2 & -4 \\ -2 & -3 \end{pmatrix}. \quad \text{thus } M(2)' \text{ in eq. (2.69) becomes } M(2)_{i,j} +$$

$$L_{i,q} \lambda_{q,q'}^{-1} R_{q',j} = \begin{pmatrix} -1 & -2 \\ 1 & 1 \end{pmatrix} + \begin{pmatrix} -1 & -1 \\ 1 & 0 \end{pmatrix} \frac{1}{3} \begin{pmatrix} 3 & -2 \\ -3 & 3 \end{pmatrix} \begin{pmatrix} -2 & -4 \\ -2 & -3 \end{pmatrix} = \frac{1}{3} \begin{pmatrix} -1 & -3 \\ 1 & -3 \end{pmatrix}.$$

And $M(4)$ is constructed as

$$M(4) = \begin{pmatrix} \frac{1}{3} \begin{pmatrix} -1 & -3 \\ 1 & -3 \end{pmatrix} & - \begin{pmatrix} -1 & -1 \\ 1 & 0 \end{pmatrix} \frac{1}{3} \begin{pmatrix} 3 & -2 \\ -3 & 3 \end{pmatrix} \\ -\frac{1}{3} \begin{pmatrix} 3 & -2 \\ -3 & 3 \end{pmatrix} \begin{pmatrix} -2 & -4 \\ -2 & -3 \end{pmatrix} & \frac{1}{3} \begin{pmatrix} 3 & -2 \\ -3 & 3 \end{pmatrix} \end{pmatrix},$$

equals to the known answer $D(4)^{-1}$.

Next, we start from $D(4)$ and remove its 3rd and 4th columns and rows to demonstrate the eq. (2.67) and (2.72). The left hand site of eq. (2.67) is

$$\det D(2)/\det D(4) = 1/3, \text{ agree with its right hand side: } \det \lambda' = \det \begin{pmatrix} 1 & -2/3 \\ -1 & 1 \end{pmatrix} =$$

$$\frac{1}{3}. \quad \text{Thus } \lambda'^{-1} = M(4)_{q,q'}^{-1} = \begin{pmatrix} 1 & -2/3 \\ -1 & 1 \end{pmatrix}^{-1} = \begin{pmatrix} 3 & 2 \\ 3 & 3 \end{pmatrix}. \quad \text{The matrix } M(2)$$

is updated as (only concern about the first two columns and rows) $\frac{1}{3} \begin{pmatrix} -1 & -3 \\ 1 & -3 \end{pmatrix} -$

$$\begin{pmatrix} \frac{1}{9} (01) \begin{pmatrix} 3 & 2 \\ 3 & 3 \end{pmatrix} \begin{pmatrix} 2 \\ 0 \end{pmatrix} & \frac{1}{9} (01) \begin{pmatrix} 3 & 2 \\ 3 & 3 \end{pmatrix} \begin{pmatrix} 6 \\ -3 \end{pmatrix} \\ \frac{1}{9} (-32) \begin{pmatrix} 3 & 2 \\ 3 & 3 \end{pmatrix} \begin{pmatrix} 2 \\ 0 \end{pmatrix} & \frac{1}{9} (-32) \begin{pmatrix} 3 & 2 \\ 3 & 3 \end{pmatrix} \begin{pmatrix} 6 \\ -3 \end{pmatrix} \end{pmatrix} = \begin{pmatrix} -1 & -2 \\ 1 & 1 \end{pmatrix}, \text{ agree with } D(2)^{-1}.$$

2.3.2 Measurement

All the observables are measured based on the Ensemble average:

$$\langle \mathcal{O} \rangle = \frac{1}{Z} \text{Tr} T_\tau (\exp(-\beta H) \mathcal{O}), \quad (2.74)$$

where $Z = \text{Tr} T_\tau \exp(-\beta H)$. Using the eq. (2.42) we can express the observable \mathcal{O} as

$$\langle \mathcal{O} \rangle = \frac{Z_0 \sum_{C_k} \left(\frac{-U}{2}\right)^k \frac{1}{k!} \prod_\sigma \langle T_\tau (n_{1\sigma} - \alpha_{1\sigma}) (n_{2\sigma} - \alpha_{2\sigma}) \cdots (n_{k\sigma} - \alpha_{k\sigma}) \mathcal{O} \rangle_0}{Z_0 \sum_{C_k} \left(\frac{-U}{2}\right)^k \prod_\sigma \det D_k^\sigma}, \quad (2.75)$$

$$= \frac{Z_0}{Z} \sum_{k=0}^{\infty} \frac{(-1)^k}{k!} \int_0^\beta \cdots \int_0^\beta d\tau_1 \cdots d\tau_k \langle T_\tau H_{loc}^I(\tau_1) \cdots H_{loc}^I(\tau_k) \mathcal{O} \rangle_0, \quad (2.76)$$

where H_{loc}^I is defined in the eq. (2.40).

1. $\mathcal{O} = \text{expansion order } k$: We can calculate the average expansion order $\langle k \rangle$ from the eq. (2.76).

$$\begin{aligned} \langle k \rangle &= \frac{Z_0}{Z} \sum_{k=0}^{\infty} \frac{(-1)^k}{k!} k \int_0^\beta \cdots \int_0^\beta d\tau_1 \cdots d\tau_k \langle T_\tau H_{loc}^I(\tau_1) \cdots H_{loc}^I(\tau_k) \rangle_0 \\ (\text{let } n = k - 1) &= -\frac{Z_0}{Z} \sum_{n=0}^{\infty} \frac{(-1)^n}{n!} \int_0^\beta \cdots \int_0^\beta d\tau_1 \cdots d\tau_n d\tau \langle T_\tau H_{loc}^I(\tau_1) \cdots H_{loc}^I(\tau_n) H_{loc}^I(\tau) \rangle_0 \\ &= -\int_0^\beta d\tau \langle H_{loc}^I(\tau) \rangle. \end{aligned} \quad (2.77)$$

If H_{loc}^I is independent of τ , $\langle k \rangle = -\beta \langle H_{loc}^I \rangle$, which is growing slowly with the interaction U . This result is important because it tells us the expansion order k is finite in the thermal average once the system size, $\beta N_c U$, is known.

2. $\mathcal{O} = \text{one-particle Green's function}$

Single-particle Green's function (also see eq. (2.48)) is defined as

$$G_{i,j}^\sigma(\tau, \tau') \equiv \left\langle T_\tau c_{i\sigma}(\tau) c_{j\sigma}^\dagger(\tau') \right\rangle = - \left\langle T_\tau c_{j\sigma}^\dagger(\tau') c_{i\sigma}(\tau) \right\rangle. \quad (2.78)$$

Replacing the \mathcal{O} in eq. (2.75) by $c_{j\sigma}^\dagger(\tau') c_{i\sigma}(\tau)$, the curly bracket in the numerator can be written in terms of a determinant and has one extra column and row adding to the end of the matrix $D^\sigma(k)$ in the eq. (2.44) and becomes $D^\sigma(k+1)$ (Here we assume that cluster-excluded Green's function is spin-independent. Check eq. (2.46)):

$$\begin{pmatrix} & & & \langle T_\tau c_{i_1}^\dagger(\tau_1) c_i(\tau) \rangle_0 \\ & D^\sigma(k) & & \vdots \\ & & & \langle T_\tau c_{i_k}^\dagger(\tau_k) c_i(\tau) \rangle_0 \\ \langle T_\tau c_j^\dagger(\tau') c_{i_1}(\tau_1) \rangle_0 & \cdots & \langle T_\tau c_j^\dagger(\tau') c_{i_k}(\tau_k) \rangle_0 & \langle T_\tau c_j^\dagger(\tau') c_i(\tau) \rangle_0 \end{pmatrix}. \quad (2.79)$$

Note the extra minus sign in the eq. (2.78) and we can write the Green's function as

$$\begin{aligned} G_{i,j}^\sigma(\tau, \tau') &= -\frac{\det D^\sigma(k+1)}{\det D^\sigma(k)} \quad (2.80) \\ (\text{using eq. (2.61)}) &= -\langle T_\tau c_j^\dagger(\tau') c_i(\tau) \rangle_0 + \langle T_\tau c_j^\dagger(\tau') c_{i_p}(\tau_p) \rangle_0 M_{p,q}^\sigma(k) \langle T_\tau c_{i_q}^\dagger(\tau_q) c_i(\tau) \rangle_0 \\ &= g_{i,j}^0(\tau, \tau') + (-1)^2 g_{i_p,j}^0(\tau_p, \tau') M_{p,q}^\sigma(k) g_{i,i_q}^0(\tau, \tau_q) \\ &= g_{i,j}^0(\tau, \tau') - g_{i,i_q}^0(\tau, \tau_q) (-M^\sigma(k)^T)_{q,p} g_{i_p,j}^0(\tau_p, \tau'), \quad (2.81) \end{aligned}$$

where the matrix $(-M^\sigma(k)^T)$ is the inversion of the bold matrix $\mathbb{D}_{p,q}^\sigma(k)$ in the (2.54) and summation over repeated indexes is implied. To sum up, in the beginning we prepare the matrix

$$\mathbb{D}^\sigma(k) = -D^\sigma(k)^T = \begin{pmatrix} -g_0^0(\beta) + \alpha_\sigma(s_1) & g^0(1, 2) & \cdots & g^0(1, k) \\ g^0(2, 1) & -g_0^0(\beta) + \alpha_\sigma(s_2) & \ddots & \vdots \\ \vdots & \ddots & \ddots & \vdots \\ g^0(k, 1) & \cdots & \cdots & -g_0^0(\beta) + \alpha_\sigma(s_k) \end{pmatrix}, \quad (2.82)$$

and invert $\mathbb{D}^\sigma(k)$ to obtain $\mathbb{M}^\sigma(k) = -M^\sigma(k)^T$, which is the required matrix in the eq. (2.81). After applying the translational symmetry in space and time, the single-particle Green's function is measured as

$$G_R^{\sigma \geq}(\tau) \equiv \frac{1}{2N_c N_L} \sum_{\sigma=\uparrow, \downarrow} \sum_{i,j=1}^{N_c} \sum_{\tau_i, \tau_j=0}^{N_L-1} \left\langle G_{i,j}^\sigma \left((\tau_i - \tau_j) \frac{\beta}{N_L} \right) \right\rangle_{QMC}, \quad (2.83)$$

$$R \equiv r_i - r_j \quad \tau \equiv (\tau_i - \tau_j) \frac{\beta}{N_L} \geq 0$$

$$G_R^{\sigma <}(\tau) \equiv \frac{1}{2N_c N_L} \sum_{\sigma=\uparrow, \downarrow} \sum_{i,j=1}^{N_c} \sum_{\tau_i, \tau_j=0}^{N_L-1} \left\langle -G_{i,j}^\sigma \left((\tau_i - \tau_j + N_L) \frac{\beta}{N_L} \right) \right\rangle_{QMC}, \quad (2.84)$$

$$R \equiv r_i - r_j \quad \tau \equiv (\tau_i - \tau_j) \frac{\beta}{N_L} < 0$$

$$G_R^\sigma(\tau) = G_R^{\sigma \geq}(\tau) + G_R^{\sigma <}(\tau). \quad (2.85)$$

where N_c is the size of cluster and N_L is the number of time slices measured in $[0, \beta]$, and $\langle \dots \rangle_{QMC}$ denotes the QMC average.. The space index R and time index τ of the Green's function also have size N_c and N_L respectively. After Fourier transformation both in space and time, we obtain the Matsubara Green's function in momentum space:

$$G(\mathbf{K}, i\omega_n) = g^0(\mathbf{K}, i\omega_n) - g^0(\mathbf{K}, i\omega_n) \left[\frac{T}{N_c} \left\langle - \sum_{i,j}^k \mathbb{M}_{i,j} e^{i\omega_n(\tau_i - \tau_j)} e^{i\mathbf{K}(r_i - r_j)} \right\rangle_{QMC} \right] g^0(\mathbf{K}, i\omega_n), \quad (2.86)$$

where $\mathbb{M}_{i,j} = \frac{1}{2}(\mathbb{M}^\uparrow + \mathbb{M}^\downarrow)_{i,j}$, $\mathbb{M}^\sigma(k) = -M^\sigma(k)^T$ which is explained after the eq. (2.82), and \mathbf{K} is the cluster momentum. The factor T/N_c is to balance the dimension and size on both hand sides of eq. (2.86).⁶ Note there is an extra minus sign inside the QMC average because we require both $G(\mathbf{K}, i\omega_n)$ and $g^0(\mathbf{K}, i\omega_n)$ to be causal, $ImG(\mathbf{K}, i\omega_n) < 0$ and $Img^0(\mathbf{K}, i\omega_n) < 0$.⁷

Single-species local density or particle occupancy is defined by

$$\begin{aligned} \langle n \rangle &= \langle G_{R=0}(\beta) \rangle_{QMC} \quad (2.87) \\ &= \left\langle g_0^0(\beta) - \sum_{i,j}^k \mathbb{M}_{i,j} \frac{1}{N_c} \sum_{p=1}^{N_c} g_{p-i}^0(\beta - \tau_i) g_{j-p}^0(\tau_j - 0) \right\rangle_{QMC} \\ &= \left\langle 1 - g_0^0(0^+) - \sum_{i,j}^k \mathbb{M}_{i,j} \frac{1}{N_c} \sum_{p=1}^{N_c} g_{p-i}^0(\beta - \tau_i) g_{j-p}^0(\tau_j - 0) \right\rangle_{QMC}, \quad (2.88) \end{aligned}$$

where we average over the spacial index for each fixed vertex time and $\mathbb{M}_{i,j} = \frac{1}{2}(\mathbb{M}^\uparrow + \mathbb{M}^\downarrow)_{i,j}$, $\mathbb{M}^\sigma(k) = -M^\sigma(k)^T$. Note that the filling is twice of the particle occupancy.

Double occupancy is defined by

$$\langle D \rangle = \langle n_\uparrow n_\downarrow \rangle_{QMC} = \left\langle G_{R=0}^\uparrow(\beta) G_{R=0}^\downarrow(\beta) \right\rangle_{QMC} \quad (2.89)$$

⁶Here we always assume that the size and dimension of $G_R(\tau)$ is one, and in terms of dimensional analysis we write it as $[G_R(\tau)] = 1$. Thus the matrix \mathbb{M} which is composed of $G_R(\tau)$ also has $[\mathbb{M}] = 1$. We also know $[e^{i\omega_n(\tau_i - \tau_j)}] = [e^{i\mathbf{K}(r_i - r_j)}] = 1$ and thus $[G(\mathbf{K}, i\omega_n)] = [g^0(\mathbf{K}, i\omega_n)] = \frac{N_c}{T}$. Also check footnote 1.

⁷In the beginning we prepare a causal cluster self energy $\Sigma(\mathbf{K}, i\omega_n)$ ($Im\Sigma(\mathbf{K}, i\omega_n) < 0$) by calculating the Feynman diagram in the second order perturbation or read in from the previous QMC output, then obtain the causal $\bar{G}(\mathbf{K}, i\omega_n)$ by doing the coarse-graining. Thus a causal $g^0(\mathbf{K}, i\omega_n)$ is obtained from the Dyson's equation $g^0(\mathbf{K}, i\omega_n) = (\bar{G}(\mathbf{K}, i\omega_n)^{-1} + \Sigma(\mathbf{K}, i\omega_n))^{-1}$.

$$= \left\langle \frac{1}{N_c} \sum_{p=1}^{N_c} \left(1 - g_0^0(0^+) - \sum_{i,j}^k \mathbb{M}_{i,j}^\dagger g_{p-i}^0(\beta - \tau_i) g_{j-p}^0(\tau_j - 0) \right) \right\rangle \quad (2.90)$$

$$\times \left(1 - g_0^0(0^+) - \sum_{i,j}^k \mathbb{M}_{i,j}^\dagger g_{p-i}^0(\beta - \tau_i) g_{j-p}^0(\tau_j - 0) \right) \Bigg\rangle_{QMC} \quad (2.91)$$

3. \mathcal{O} = two-particle Green's function

A. Transverse spin susceptibility:

$$\chi_{i,j}^{+-}(\tau, \tau') = \langle T_\tau S_i^+(\tau) S_j^-(\tau') \rangle = \left\langle T_\tau c_{i\uparrow}^\dagger(\tau) c_{i\downarrow}(\tau) c_{j\downarrow}^\dagger(\tau') c_{j\uparrow}(\tau') \right\rangle \quad (2.92)$$

$$\begin{aligned} &= -\frac{Z_0}{Z} \sum_{C_k} \left(\frac{-U}{2} \right)^k \frac{1}{k!} \left\langle T_\tau c_{i\uparrow}^\dagger(\tau) c_{j\uparrow}(\tau') (n_{1\uparrow} - \alpha_{1\uparrow}) \cdots (n_{k\uparrow} - \alpha_{k\uparrow}) \right\rangle_0 \\ &\quad \times \left\langle T_\tau c_{j\downarrow}^\dagger(\tau') c_{i\downarrow}(\tau) (n_{1\downarrow} - \alpha_{1\downarrow}) \cdots (n_{k\downarrow} - \alpha_{k\downarrow}) \right\rangle_0 \\ &= -G_{j,i}^\uparrow(\tau', \tau) G_{i,j}^\downarrow(\tau, \tau'), \end{aligned} \quad (2.93)$$

where $G_{i,j}^\sigma(\tau, \tau')$ is the single-particle Green's function defined in the eq. (2.81). After applying the translational symmetry in space and time, we obtain

$$\chi_R^{+-}(\tau) = \left\langle \frac{1}{N_c N_L} \sum_{\substack{i,j=1 \\ R \equiv r_i - r_j}}^{N_c} \sum_{\substack{\tau_i, \tau_j=0 \\ \tau'' \equiv (\tau_i - \tau_j) \frac{\beta}{N_L}}}^{N_L-1} \left[-G_{-R}^\uparrow(-\tau'') G_R^\downarrow(\tau'') + \delta_{i,j} \delta_{\tau_i, \tau_j} G_{R=0}^\uparrow(0) \right] \right\rangle, \quad (2.94)$$

where we use

$$G_R^\sigma(\tau'') = G_R^\sigma(\tau) \text{ if } \tau'' \in [0, \beta], \quad (2.95)$$

$$G_R^\sigma(\tau'') = -G_R^\sigma(\tau + \beta) \text{ if } \tau'' \in [-\beta, 0^-], \quad (2.96)$$

to keep the time argument of $\chi_R^{+-}(\tau)$ to be in the range $[0, \beta]$. Note that we add a correction $\delta_{i,j} \delta_{\tau, \tau'} G_{R=0}^\uparrow(0)$ for the case of $R = 0$ and $\tau'' \equiv (\tau_i - \tau_j) \frac{\beta}{N_L} = 0$.⁸

⁸Because the two time indexes in different Green's functions swap their positions in eq. (2.93) and when $\tau \rightarrow \tau'$, one argument is $\tau - \tau' = 0^-$ and the other argument is $\tau - \tau' = 0^+$. When $R = i - j \neq 0$, the Green's functions are continuous at $\tau - \tau' = 0$ and there is no difference for $\tau - \tau' = 0^+$ and 0^- . But when $R = 0$, the Green's function is discontinuous at $\tau - \tau' = 0$ (check eq. (2.51)). What we really need in the spin susceptibility at $R = 0$ and $\tau - \tau' = 0$ is $-G_{R=0}^\uparrow(0^+, 0) G_{R=0}^\downarrow(0, 0^+) = -(1 - \langle n^\uparrow \rangle)(-\langle n^\downarrow \rangle)$, but numerically the local and equal-time Green's function means $G_{R=0}^\sigma(0^+, 0) = (1 - \langle n^\sigma \rangle)$. Thus the local and equal-time spin susceptibility erroneously becomes $-(1 - \langle n^\uparrow \rangle)(1 - \langle n^\downarrow \rangle)$, which needs to add the extra term $(1 - \langle n^\uparrow \rangle) = G_{R=0}^\uparrow(0)$ to fix the error. The correction for $\chi_{i,j}^{+-}(\tau, \tau')$ is $\delta_{i,j} \delta_{\tau, \tau'} G_{R=0}^\uparrow(0)$. There is no correction in the pairing susceptibility (see eq. (2.114)).

B. Longitudinal spin susceptibility:

$$\chi_{i,j}^{zz}(\tau, \tau') \equiv \langle T_\tau S_i^z(\tau) S_j^z(\tau') \rangle \quad (2.97)$$

$$\begin{aligned} &= \left\langle T_\tau \left(c_{i\uparrow}^\dagger(\tau) c_{i\uparrow}(\tau) - c_{i\downarrow}^\dagger(\tau) c_{i\downarrow}(\tau) \right) \left(c_{j\uparrow}^\dagger(\tau') c_{j\uparrow}(\tau') - c_{j\downarrow}^\dagger(\tau') c_{j\downarrow}(\tau') \right) \right\rangle \\ &= \left\langle T_\tau \left(c_{i\uparrow}^\dagger(\tau) c_{i\uparrow}(\tau) c_{j\uparrow}^\dagger(\tau') c_{j\uparrow}(\tau') - c_{i\uparrow}^\dagger(\tau) c_{i\uparrow}(\tau) c_{j\downarrow}^\dagger(\tau') c_{j\downarrow}(\tau') \right. \right. \\ &\quad \left. \left. - c_{i\downarrow}^\dagger(\tau) c_{i\downarrow}(\tau) c_{j\uparrow}^\dagger(\tau') c_{j\uparrow}(\tau') + c_{i\downarrow}^\dagger(\tau) c_{i\downarrow}(\tau) c_{j\downarrow}^\dagger(\tau') c_{j\downarrow}(\tau') \right) \right\rangle. \end{aligned} \quad (2.98)$$

Here we need to use the eq. (2.66) to handle the four Fermionic operators with equal spin. The eq. (2.98) becomes

$$\begin{aligned} \chi_{i,j}^{zz}(\tau, \tau') &= \left(G_{ii}^\uparrow(\tau, \tau) G_{jj}^\uparrow(\tau', \tau') - G_{ij}^\uparrow(\tau, \tau') G_{ji}^\uparrow(\tau', \tau) \right) - G_{ii}^\uparrow(\tau, \tau) G_{jj}^\downarrow(\tau', \tau') \\ &\quad - G_{ii}^\downarrow(\tau, \tau) G_{jj}^\uparrow(\tau', \tau') + \left(G_{ii}^\downarrow(\tau, \tau) G_{jj}^\downarrow(\tau', \tau') - G_{ij}^\downarrow(\tau, \tau') G_{ji}^\downarrow(\tau', \tau) \right) \quad (2.99) \\ &= \chi_{i,j,con}^{zz} + \chi_{i,j,discon}^{zz}, \end{aligned} \quad (2.100)$$

where we define the connected term $\chi_{i,j,con}^{zz}$ with different space and time arguments and the disconnected term $\chi_{i,j,discon}^{zz}$ with the same ones. We also use the equal-time convention that the second time argument is slightly greater:

$$\chi_{i,j,con}^{zz} = - \sum_{\sigma, \sigma'} \delta_{\sigma, \sigma'} \left(G_{ij}^\sigma(\tau, \tau') G_{ji}^\sigma(\tau', \tau) \right), \quad (2.101)$$

$$\chi_{i,j,discon}^{zz} = \sum_{\sigma, \sigma'} \sigma \sigma' \left(G_{ii}^\sigma(\tau, \tau^+) G_{jj}^{\sigma'}(\tau', \tau'^+) \right), \quad (2.102)$$

and $G_{ii}^\sigma(\tau, \tau^+) = 1 - G_{R=0}^\sigma(\tau^+, \tau) = 1 - G_{R=0}^\sigma(0)$. Similar to the correction term in the transverse spin susceptibility in eq. (2.94), here after the QMC average and use the eq. (2.95) and (2.96) the longitudinal spin susceptibility becomes

$$\begin{aligned} \chi_R^{zz}(\tau) &= \left\langle \frac{1}{2N_c N_L} \sum_{\substack{i, j=1 \\ R \equiv r_i - r_j}}^{N_c} \sum_{\substack{\tau_i, \tau_j=0 \\ \tau'' \equiv (\tau_i - \tau_j) \frac{\beta}{N_L}}}^{N_L-1} \left[\chi_{i,j,con}^{zz}(\tau'') + \delta_{i,j} \delta_{\tau, \tau'} \left(G_{R=0}^\uparrow(0) + G_{R=0}^\downarrow(0) \right) \right. \right. \\ &\quad \left. \left. + \chi_{i,j,discon}^{zz}(\tau'') \right] \right\rangle_{QMC} \end{aligned} \quad (2.103)$$

where the extra factor 2 will be explained later. Interestingly, if $G_{i,j}^\sigma(\tau, \tau') = G_{i,j}(\tau, \tau')$ which is independent of spin, we find that the disconnected term is zero:

$$\chi_{i,j,discon}^{zz} = \sum_{\sigma, \sigma'} \sigma \sigma' \left(G_{ii}^\sigma(\tau, \tau^+) G_{jj}^{\sigma'}(\tau', \tau'^+) \right) = 0. \quad (2.104)$$

And the $\chi_{i,j}^{zz}(\tau, \tau')$ has only the connected term $\chi_{i,j,con}^{zz}$ which is twice of the $\chi_{i,j}^{+-}(\tau, \tau')$ in eq. (2.93):

$$\chi_{i,j}^{zz}(\tau, \tau') = 2\chi_{i,j}^{+-}(\tau, \tau') = \chi_{i,j}^{+-}(\tau, \tau') + \chi_{i,j}^{-+}(\tau, \tau'), \quad (2.105)$$

which means that the spin symmetry is not broken and the longitudinal spin susceptibility is just twice of the transverse spin susceptibility. The extra factor 2 in the eq. (2.103) is to re-scale the $\chi_R^{zz}(\tau)$ to be measured per spin species.

To extract the two-particle vertex in the charge channel from the Bethe-Salpeter equations, we need to measure the charge susceptibility in the momentum and frequency spaces. After Fourier transformation both in space and time, we obtain the Matsubara Green's function in momentum space:

$$\begin{aligned} G(\mathbf{K}, i\omega_n, \mathbf{K}', i\omega'_n) &= g^0(\mathbf{K}, i\omega_n)\delta_{\mathbf{K},\mathbf{K}'}\delta_{i\omega_n,i\omega'_n} - g^0(\mathbf{K}, i\omega_n) \\ &\times \left[\frac{T}{N_c} \left(- \sum_{i,j}^k e^{i\mathbf{K}\mathbf{R}_i} e^{i\omega_n\tau_i} \mathbb{M}_{i,j} e^{-i\tau_j\omega'_n} e^{-i\mathbf{R}_j\mathbf{K}'} \right) \right] \\ &\times g^0(\mathbf{K}', i\omega'_n), \end{aligned} \quad (2.106)$$

or rewrite it using a four-momentum index $P \equiv (\mathbf{K}, i\omega_n)$ and $R \equiv (\mathbf{R}, \tau)$:

$$G(P, P') = g^0(P)\delta_{P,P'} - g^0(P)(-\mathbb{M}_{P,P'})g^0(P'), \quad (2.107)$$

$$\mathbb{M}_{P,P'} \equiv \sum_{i,j}^k e^{iP\cdot R_i} \mathbb{M}_{i,j} e^{-iR_j\cdot P'}. \quad (2.108)$$

In momentum and frequency space, the measurement becomes (use $Q \equiv (\mathbf{Q}, i\nu_m)$)

$$\chi_{con}^{zz}(P, P', Q) = - \sum_{\sigma,\sigma'} \delta_{\sigma,\sigma'} G^\sigma(P, P') G^\sigma(P' + Q, P + Q), \quad (2.109)$$

$$\chi_{discon}^{zz}(P, P', Q) = \sum_{\sigma,\sigma'} \sigma\sigma' G^\sigma(P, P + Q) G^{\sigma'}(P' + Q, P'). \quad (2.110)$$

$$\chi_c^{zz}(P, P', Q) = \frac{1}{2} \langle \chi_{con}^{zz}(P, P', Q) + \chi_{discon}^{zz}(P, P', Q) \rangle_{QMC}. \quad (2.111)$$

C. Pair susceptibility:

$$\chi_{i,j}^p(\tau, \tau') = \langle T_\tau \Delta_i^+(\tau) \Delta_j(\tau') \rangle = \langle T_\tau c_{i\uparrow}^\dagger(\tau) c_{i\downarrow}^\dagger(\tau) c_{j\downarrow}(\tau') c_{j\uparrow}(\tau') \rangle \quad (2.112)$$

$$= \prod_{\sigma} G_{j,i}^{\sigma}(\tau', \tau). \quad (2.113)$$

Similarly, we apply the QMC average to recover the translational symmetry in space and time, use the eq. (2.95) and (2.96) and note that there is no correction term for $R = 0$ and $\tau - \tau' = 0$ here:

$$\chi_R^p(\tau) = \left\langle \frac{1}{N_c N_L} \sum_{\substack{i, j = 1 \\ R \equiv r_i - r_j}}^{N_c} \sum_{\substack{\tau_i, \tau_j = 0 \\ \tau'' \equiv (\tau_i - \tau_j) \frac{\beta}{N_L}}}^{N_L - 1} G_{-R}^\uparrow(-\tau'') G_{-R}^\downarrow(-\tau'') \right\rangle_{QMC}. \quad (2.114)$$

In momentum and frequency space, use the property of $G^\sigma(-P, -P') = (G^\sigma(P, P'))^*$, the measurement becomes

$$\chi_c^p(P, P', Q) = G^\uparrow(P + Q, P' + Q) (G^\downarrow(P, P'))^*. \quad (2.115)$$

After we symmetrize the up and down spins in the QMC average, the measurement becomes

$$\chi_c^p(P, P', Q) = \left\langle \frac{1}{2} [G^\uparrow(P + Q, P' + Q) (G^\downarrow(P, P'))^* + G^\downarrow(P + Q, P' + Q) (G^\uparrow(P, P'))^*] \right\rangle_{QMC}. \quad (2.116)$$

D. Charge susceptibility:

$$\chi_{i,j}^C(\tau, \tau') \equiv \langle T_\tau n_i(\tau) n_j(\tau') \rangle - \langle n_i(\tau) \rangle \langle n_j(\tau') \rangle \quad (2.117)$$

$$= \left\langle T_\tau \left(c_{i\uparrow}^\dagger(\tau) c_{i\uparrow}(\tau) + c_{i\downarrow}^\dagger(\tau) c_{i\downarrow}(\tau) \right) \left(c_{j\uparrow}^\dagger(\tau') c_{j\uparrow}(\tau') + c_{j\downarrow}^\dagger(\tau') c_{j\downarrow}(\tau') \right) \right\rangle - \left(G_{R=0}^\uparrow(\beta) + G_{R=0}^\downarrow(\beta) \right)^2 \quad (2.118)$$

$$= \left\langle T_\tau \left(c_{i\uparrow}^\dagger(\tau) c_{i\uparrow}(\tau) c_{j\uparrow}^\dagger(\tau') c_{j\uparrow}(\tau') + c_{i\uparrow}^\dagger(\tau) c_{i\uparrow}(\tau) c_{j\downarrow}^\dagger(\tau') c_{j\downarrow}(\tau') \right. \right. \\ \left. \left. + c_{i\downarrow}^\dagger(\tau) c_{i\downarrow}(\tau) c_{j\uparrow}^\dagger(\tau') c_{j\uparrow}(\tau') + c_{i\downarrow}^\dagger(\tau) c_{i\downarrow}(\tau) c_{j\downarrow}^\dagger(\tau') c_{j\downarrow}(\tau') \right) \right\rangle - \left(G_{R=0}^\uparrow(\beta) + G_{R=0}^\downarrow(\beta) \right)^2 \quad (2.119)$$

$$= \chi_{i,j,con}^C + \chi_{i,j,discon}^C - \chi_{vacumn}^C \quad (2.120)$$

$$\chi_{i,j,con}^C = - \sum_{\sigma, \sigma'} \delta_{\sigma, \sigma'} \left(G_{ij}^\sigma(\tau, \tau') G_{ji}^\sigma(\tau', \tau) \right), \quad (2.121)$$

$$\chi_{i,j,discon}^C = \sum_{\sigma, \sigma'} \left(G_{ii}^\sigma(\tau, \tau^+) G_{jj}^{\sigma'}(\tau', \tau'^+) \right), \quad (2.122)$$

$$\chi_{vacumn}^C = \left(G_{R=0}^\uparrow(\beta) + G_{R=0}^\downarrow(\beta) \right)^2 = [2(1 - G_{R=0}(0^+))]^2 \quad (2.123)$$

Charge and longitudinal spin susceptibility look very similar except that all the disconnected terms of the charge susceptibility are finite ($\chi_{i,j,discon}^C \neq 0$ if $G_{i,j}(\tau, \tau')$ is spin-independent).

However, the disconnected terms subtract by the vacuum term under the QMC average are almost zero at high temperature (small β):

$$\langle \chi_{i,j,discon}^C \rangle_{QMC} - \langle \chi_{vacumn}^C \rangle_{QMC} \approx 0. \quad (2.124)$$

Generally, we cannot neglect any term in the charge susceptibility.

$$\begin{aligned} \chi_R^C(\tau) = & \left\langle \frac{1}{N_c N_L} \sum_{\substack{i,j=1 \\ R \equiv r_i - r_j}}^{N_c} \sum_{\substack{\tau_i, \tau_j = 0 \\ \tau'' \equiv (\tau_i - \tau_j) \frac{\beta}{N_L}}}^{N_L-1} \left[\chi_{i,j,con}^C + \delta_{i,j} \delta_{\tau,\tau'} \left(G_{R=0}^\uparrow(0) + G_{R=0}^\downarrow(0) \right) \right. \right. \\ & \left. \left. + \chi_{i,j,discon}^C \right] \right\rangle_{QMC} - [2(1 - G_{R=0}(0^+))]^2. \end{aligned} \quad (2.125)$$

The charge susceptibility measured in momentum and frequency space is similar to that measured in space and time (eq. (2.119)).

$$\chi_{con}^C(P, P', Q) = - \sum_{\sigma, \sigma'} \delta_{\sigma, \sigma'} G^\sigma(P, P') G^\sigma(P' + Q, P + Q), \quad (2.126)$$

$$\chi_{discon}^C(P, P', Q) = \sum_{\sigma, \sigma'} G^\sigma(P, P + Q) G^{\sigma'}(P' + Q, P'), \quad (2.127)$$

$$\chi_{vacumn}^C(P, P', Q) = (G^\uparrow(P + Q, P) + G^\downarrow(P + Q, P)) (G^\uparrow(P' + Q, P') + G^\downarrow(P' + Q, P')).$$

Under the QMC average, the charge cluster susceptibility becomes

$$\chi_c^C(P, P', Q) = \langle \chi_{con}^C(P, P', Q) + \chi_{discon}^C(P, P', Q) - \chi_{vacumn}^C(P, P', Q) \rangle_{QMC}. \quad (2.128)$$

D. Square local moment:

$$m_{ii}^2(\tau, \tau) = \langle (n^\uparrow - n^\downarrow)^2 \rangle \quad (2.129)$$

$$\begin{aligned} (\text{since } (n^\sigma)^2 = n^\sigma) &= \langle n^\uparrow + n^\downarrow - n^\uparrow n^\downarrow \rangle \\ &= \langle G_{ii}^\uparrow(\tau, \tau) + G_{ii}^\downarrow(\tau, \tau) - G_{ii}^\uparrow(\tau, \tau) G_{ii}^\downarrow(\tau, \tau) \rangle. \end{aligned} \quad (2.130)$$

$$m_{R=0}^2(\tau = 0) = \left\langle \frac{1}{N_c N_L} \sum_{i=1}^{N_c} \sum_{\tau_i=0}^{N_L-1} \left(G_{ii}^\uparrow(\tau, \tau) + G_{ii}^\downarrow(\tau, \tau) - G_{ii}^\uparrow(\tau, \tau) G_{ii}^\downarrow(\tau, \tau) \right) \right\rangle_{QMC}, \quad (2.131)$$

with $\tau = \tau_i \frac{\beta}{N_L}$. In the eq. (2.130), it doesn't matter if we take $n^\sigma = 1 - G_{ii}^\sigma(\tau, \tau)$ or not since the result of the square local moment would be the same.

2.3.3 Bethe-Salpeter equation

Now we focus on the two-particle cluster susceptibilities in the magnetic, pairing and charge channels in the eq. (2.111), (2.116) and (2.128) respectively. Bethe-Salpeter equation, analogous to the Dyson's equation, allows us to extract the irreducible vertex Γ from the two-particle susceptibilities:

$$\chi_c^{0-1}(P, P' = P) - \chi_c^{-1}(P, P', Q) = \Gamma(P, P', Q), \quad (2.132)$$

where χ^{0-1} is the non-interacting susceptibility composed of a pair of fully-dressed single-particle Green's functions and is defined as

$$\chi_c^0(P, P') = -G(P)G(P' + Q)\delta_{P,P'} \text{ (magnetic)} \quad (2.133)$$

$$\chi_c^0(P, P') = +G(-P)G(P' + Q)\delta_{P,P'} \text{ (pairing)} \quad (2.134)$$

$$\chi_c^0(P, P') = -2G(P)G(P' + Q)\delta_{P,P'}, \text{ (charge)} \quad (2.135)$$

which are very similar to the connected terms in the eq. (2.109), (2.115) and (2.126) respectively, and the single-particle Green's function $G(P) \equiv G(\mathbf{K}_c, i\omega_n)$ is defined in the eq. (2.86). Note that there is an extra factor 2 in the eq. (2.135) because we do not divide the charge susceptibility by two in the eq. (2.128).

The real physical quantities, lattice susceptibilities $\bar{\chi}$, are obtained by a coarse-grained non-interacting susceptibility $\bar{\chi}^0$ plus the interacting effects captured from the irreducible vertex Γ' :

$$\bar{\chi} = \frac{\bar{\chi}^0}{1 - \Gamma' \bar{\chi}^0}. \quad (2.136)$$

We always assume that the irreducible vertex Γ' in the lattice susceptibility and the Γ in the cluster susceptibility (eq. (2.132)) are equivalent once they are coarse-grained to the cluster level so that

$$\bar{\chi}^{0-1} - \bar{\chi}^{-1} = \Gamma' = \Gamma = \chi_c^{0-1} - \chi_c^{-1}, \quad (2.137)$$

and the lattice and cluster susceptibilities are obtained by several useful expressions:

$$\begin{aligned} \bar{\chi} &= \frac{1}{\bar{\chi}^{0-1} - \Gamma} & \chi_c &= \frac{1}{\chi_c^{0-1} - \Gamma} \\ &= \frac{\bar{\chi}^0}{1 - \Gamma \bar{\chi}^0} & &= \frac{\chi_c^0}{1 - \Gamma \chi_c^0} \end{aligned} \quad (2.138)$$

$$\begin{aligned} &= \bar{\chi}^0 (1 + \Gamma \bar{\chi}^0 + \Gamma \bar{\chi}^0 \Gamma \bar{\chi}^0 \dots) & &= \chi_c^0 (1 + \Gamma \chi_c^0 + \Gamma \chi_c^0 \Gamma \chi_c^0 \dots) \\ &= \bar{\chi}^0 + \bar{\chi}^0 \Gamma \bar{\chi} & &= \chi_c^0 + \chi_c^0 \Gamma \chi_c \end{aligned} \quad (2.139)$$

$$= \bar{\chi}^0 + \bar{\chi}^0 F \bar{\chi}^0 = \chi_c^0 + \chi_c^0 F_c \chi_c^0. \quad (2.140)$$

where F (F_c) is the lattice (cluster) fully-reducible vertex and is defined by

$$F = \frac{\Gamma}{1 - \bar{\chi}^0 \Gamma} \quad F_c = \frac{\Gamma}{1 - \chi_c^0 \Gamma} \quad (2.141)$$

$$\begin{aligned} &= \Gamma + F \bar{\chi}^0 \Gamma &= \Gamma + F_c \chi_c^0 \Gamma \\ &= \Gamma + \Gamma \bar{\chi}^0 F &= \Gamma + \Gamma \chi_c^0 F_c \\ (\text{from eq. (2.140)}) &= \bar{\chi}^{0-1} (\bar{\chi} - \bar{\chi}^0) \bar{\chi}^{0-1} &= \chi_c^{0-1} (\chi_c - \chi_c^0) \chi_c^{0-1}. \end{aligned} \quad (2.142)$$

And Γ in terms of F ⁹ is

$$\Gamma = \frac{F}{1 + F \bar{\chi}^0} \quad \Gamma = \frac{F_c}{1 + F_c \chi_c^0} \quad (2.143)$$

$$= \frac{F}{1 + \bar{\chi}^0 F} \quad = \frac{F_c}{1 + \chi_c^0 F_c}. \quad (2.144)$$

Experimentally only the lattice susceptibility ($\bar{\chi}$) and the lattice fully-reducible vertex F can be measured and have physical meanings. Plug right formula of eq. (2.144) into left of eq. (2.141), we obtain lattice F in terms of cluster F_c as

$$F = \frac{F_c}{1 - (\bar{\chi}^0 - \chi_c^0) F_c}. \quad (2.145)$$

The eq. (2.145) also determine T_c when the condition $(\bar{\chi}^0 - \chi_c^0) F_c = 1$ is fulfilled. Another way to determine T_c is based on the pairing matrix described in the following.

Now we are ready to define the coarse-grained non-interacting susceptibilities in three different channels (use $P = (\mathbf{K}, i\omega_n)$):

$$\bar{\chi}^0(P, P) = -\frac{N_c}{N} \sum_{\tilde{\mathbf{k}}} \frac{1}{i\omega_n - \epsilon_{\mathbf{K}+\tilde{\mathbf{k}}} + \mu - \Sigma(\mathbf{K})} \frac{1}{i\omega_n - \epsilon_{\mathbf{K}+\mathbf{Q}+\tilde{\mathbf{k}}} + \mu - \Sigma(\mathbf{K} + \mathbf{Q})} \quad (\text{magnetic}) \quad (2.146)$$

$$\bar{\chi}^0(P, P) = \frac{N_c}{N} \sum_{\tilde{\mathbf{k}}} \frac{1}{-i\omega_n - \epsilon_{-\mathbf{K}-\tilde{\mathbf{k}}} + \mu - \Sigma(-\mathbf{K})} \frac{1}{i\omega_n - \epsilon_{\mathbf{K}+\mathbf{Q}+\tilde{\mathbf{k}}} + \mu - \Sigma(\mathbf{K} + \mathbf{Q})} \quad (\text{pairing}) \quad (2.147)$$

$$\bar{\chi}^0(P, P) = -2 \frac{N_c}{N} \sum_{\tilde{\mathbf{k}}} \frac{1}{i\omega_n - \epsilon_{\mathbf{K}+\tilde{\mathbf{k}}} + \mu - \Sigma(\mathbf{K})} \frac{1}{i\omega_n - \epsilon_{\mathbf{K}+\mathbf{Q}+\tilde{\mathbf{k}}} + \mu - \Sigma(\mathbf{K} + \mathbf{Q})} \quad (\text{charge}) \quad (2.148)$$

⁹Be careful about the right or left multiplication. For example, $\frac{F}{1+F\bar{\chi}^0}$ means $(1 + F\bar{\chi}^0)^{-1} F$ and $\frac{F}{1+\bar{\chi}^0 F}$ means $F (1 + \bar{\chi}^0 F)^{-1}$.

Table 2.3: Phases corresponding to the leading eigenvalue of the pairing matrix in eq. (2.149) equals to one in the magnetic, charge and pairing channels. The d - ($d + id$)-wave at $Q = 0$ on the square (triangular) lattice is only for the hole-doped case in this thesis.

Phase for $\lambda = 1$	$Q = 0$ (square)	$Q = 0$ (triangular)	$Q = (\pi, \pi)$ (square)	$Q = K$ (triangular)
magnetic	Ferromagnetic	Ferromagnetic	Anti-ferromagnetic	Anti-ferromagnetic
charge	CDW	CDW	CDW	–
pairing	d -wave	$d + id$ -wave	–	–

Phase transition occurs when the lattice susceptibility $\bar{\chi}$ diverges, i.e., the denominator of the eq. (2.138) goes to zero. If we define a 'pairing matrix' for a fixed $Q = (\mathbf{Q}, i\nu_m = 0)$,

$$M(P, P') \equiv \Gamma(P, P')\bar{\chi}^0(P', P'), \quad (2.149)$$

which is a two-dimensional matrix with size $(N_c N_\omega)^2$, we say if the leading eigenvalue λ of the pairing matrix goes to one, the system is experiencing a second order phase transition. In the pairing channel, the corresponding eigenvectors tell us the pairing structure in the momentum space, which guides us to choose a correct form factor to strengthen the pairing susceptibility after projecting the quantity with a corresponding form factor.

We concern about the pairing mechanism. The Fermionic system requires the parity of total wavefunction to be odd. Table (2.4) shows all possible pairing combinations. In the hole-doped side of square-lattice Hubbard model, we find a d -wave pairing with $T_c = 0.028t$ when $n \approx 0.85$, $t'/t = 0$, $U = 6t$ and $N_c = 16$ (inset of the Fig. 3.1). In the hole-doped side of triangular-lattice Hubbard model, we find a $d_{x^2-y^2} + id_{xy}$ -wave pairing with $T_c = 0.06t$ when $n \approx 0.9$, $t'/t = 1$, $U = 8.5t$ and $N_c = 6$ (Fig. 5.3). The orbitals in both cases are d -wave and their corresponding spin configurations are singlets. The singlet (s) and triplet (t) channels for a fixed $Q = Q^* \equiv (\mathbf{Q}, i\nu_m = 0)$ are defined as

$$\chi_{s/t}(P, P') = \chi(P, P') \pm \chi(P, -P' - Q^*), \quad (2.150)$$

where χ can be the lattice pairing susceptibility $\bar{\chi}$, or the reducible vertex F , or the irreducible vertex Γ . Here we show how to construct a pairing matrix at $Q \equiv (\mathbf{Q} = 0, i\nu_m = 0)$ in the singlet and triplet channels. When the irreducible vertex is symmetrized, the lattice bare bubble has a symmetry factor $\frac{1}{2}$ to prevent the double counting.¹⁰

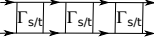
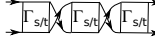
¹⁰When the particle-particle vertex is symmetrized into singlet or triplet, the upper and lower external legs of the vertex are not distinguishable by their spin configurations. For example, the diagram  and  are identical when the second diagram flips the middle irreducible vertex by 180°. To prevent such a double counting, a symmetry factor $\frac{1}{2}$ is added between the pairing bare bubble and the irreducible vertex. Because the eq. (2.151) is part of the eq. (2.138), where both left- and right-hand side of each $\Gamma_{s/t}$ has a $\bar{\chi}_{s/t}^0$, one needs two symmetry factors $\frac{1}{2}$ to avoid the double counting. For the symmetrized particle-hole vertex, no symmetry factor is required.

Table 2.4: Possible pairing combinations in momentum, frequency and spin configuration in s , p , d and f orbitals.

	Momentum	Frequency	Spin	
s	even	even odd	odd (singlet) even (triplet)	
p	odd	even odd	even (triplet) odd (singlet)	
d and $d_{x^2-y^2} + id_{xy}$	even	even odd	odd (singlet) even (triplet)	Chapter (4) and (5)
f	odd	even odd	even (triplet) odd (singlet)	

$$M_{s/t}(P, P') \equiv \frac{1}{2}\Gamma_{s/t}(P, P')\frac{1}{2}\bar{\chi}_{s/t}^0(P', P') \quad (2.151)$$

$$\begin{aligned} \text{(use eq. (2.150))} &= \frac{1}{2}[\Gamma(P, P'') \pm \Gamma(P, -P'')] \frac{1}{2}[\delta_{P'', P'} \pm \delta_{P'', -P'}] \bar{\chi}^0(P', P') \\ &= \frac{1}{4} \times 2[\Gamma(P, P') \pm \Gamma(P, -P')] \bar{\chi}^0(P', P'). \end{aligned} \quad (2.152)$$

We always compare the leading eigenvalues (λ) of the original pairing matrix in eq. (2.149) and the eigenvalues ($\lambda_{s/t}$) of the singlet or triplet pairing matrix in eq. (2.151) to understand the pairing mechanism in the table (2.4). For example, we have $\lambda \approx \lambda_s \gg \lambda_t$ near optimal doping in the square-lattice Hubbard model and the eigenvalues give evidence that the pairing should be a singlet.

In the following we will explain how to identify the possible pairing symmetry by projecting the pairing susceptibility on different form factors. The form factor of each orbital shown in the table (2.4) is defined by

$$|s\rangle = 1, \text{ (square, triangular)} \quad (2.153)$$

$$|p\rangle = \sin k_x + \sin k_y, \text{ (square)} \quad (2.154)$$

$$|d\rangle = \cos k_x - \cos k_y, \text{ (square)} \quad (2.155)$$

$$|d_{x^2-y^2}\rangle = 2\cos k_x - 2\cos\left(\frac{k_x}{2}\right)\cos\left(\frac{\sqrt{3}k_y}{2}\right), \text{ (triangular)} \quad (2.156)$$

$$|d_{xy}\rangle = -2\sin\left(\frac{k_x}{2}\right)\sin\left(\frac{\sqrt{3}k_y}{2}\right), \text{ (triangular)} \quad (2.157)$$

$$|f\rangle = \sin(k_y) - 2\cos\left(\frac{\sqrt{3}k_x}{2}\right)\cos\left(\frac{k_y}{2}\right). \text{ (triangular)} \quad (2.158)$$

The physical quantities we care about are the lattice pairing susceptibility and irreducible vertex projected with different form factors of interest. For example, the d -wave susceptibility $\bar{\chi}_d \equiv \langle d|\bar{\chi}|d \rangle / \langle d|d \rangle$ diverges at a finite T_c near optimal doping ($n = 0.85$, $t'/t = 0$) in the square-lattice Hubbard model and the $d + id$ -wave susceptibility $\chi_{d+id} \equiv \langle d + id|\bar{\chi}|d + id \rangle / \langle d + id|d + id \rangle$, where $d+id \equiv d_{x^2-y^2} + id_{xy}$, diverges at the hole-doped side ($n = 0.9$, $t'/t = 1$) in the triangular-lattice Hubbard model. The irreducible vertex projected with the corresponding form factor is called pairing strength. For example, we will show the d -wave pairing strength $V_d \equiv \langle d|\Gamma|d \rangle / \langle d|d \rangle$ as a function of doping in the square-lattice Hubbard model and the $d + id$ -wave pairing strength $V_{d+id} \equiv \langle d + id|\Gamma|d + id \rangle / \langle d + id|d + id \rangle$ in the triangular-lattice Hubbard model in the following sections.

Here we will demonstrate how to project the form factors on a lattice susceptibility in a singlet or triplet channel. We start from the eq. (2.140), and define its singlet and triplet channels according to the eq. (2.150):

$$\bar{\chi}_{s/t} = \bar{\chi}_{s/t}^0 + \bar{\chi}_{s/t}^0 F_{s/t} \bar{\chi}_{s/t}^0. \quad (2.159)$$

According to the table (2.4), we need to consider the even or odd form factors in the momentum space and denoting them as $|k_{e/o}\rangle$ (eq. (2.153) to eq. (2.158)). The odd frequency form factor is defined by

$$f_{odd}(\omega_n) = \begin{cases} 1, & \omega_n > 0 \\ 0, & \omega_n = 0 \\ -1, & \omega_n < 0 \end{cases}. \quad (2.160)$$

Of course, $f_{even}(\omega_n) = 1$ for all ω_n . In fact, the eq. (2.159) is the coarse-grained susceptibility projected with the s -wave form factor in eq. (2.153). Considering other form factors, we need to project the lattice $\chi_{s/t}$ with the form factor before coarse-graining. Here we define the bare lattice $\chi_{s/t}^0$ is just the eq. (2.133) to (2.135) replaced the cluster momentum by a lattice momentum with the notation $p \equiv (\mathbf{k}, i\omega_n)$ with $\mathbf{k} \equiv \mathbf{K} + \tilde{\mathbf{k}}$. First we consider the even frequency case, where the combination (momentum, spin) equals to (even, singlet) or (odd, triplet), and the lattice bare bubble projected by the form factors becomes

$$\begin{aligned} \overline{\langle k_{e/o} | \chi_{s/t}^0 | k_{e/o} \rangle} &= \overline{\langle k_{e/o} | [\delta_{p'', p'} \pm \delta_{p'', -p'}] \chi^0(p', p') | k_{e/o} \rangle} \\ &= 2\bar{\chi}^0(P, P), \end{aligned} \quad (2.161)$$

where the overbar of the curly bracket means the coarse-graining, the odd parity in momentum cancels the minus sign between the delta functions and thus we obtain the coarse-grained lattice bubble which is defined as

$$\bar{\chi}^0(P, P) \equiv \frac{N_c}{N} \sum_{\tilde{\mathbf{k}}} \langle k_{e/o}(\mathbf{K} + \tilde{\mathbf{k}}) | \chi^0(\mathbf{K} + \tilde{\mathbf{k}}, i\omega_n, \mathbf{K} + \tilde{\mathbf{k}}, i\omega_n) | k_{e/o}(\mathbf{K} + \tilde{\mathbf{k}}) \rangle. \quad (2.162)$$

With the help of the symmetry factor $\frac{1}{2}$ between $\chi_{s/t}^0$ and F (see footnote 10), the second term on the right hand side of eq. (2.159) becomes

$$\begin{aligned} \overline{\left\langle k_{e/o} \left| \chi_{s/t}^0 \frac{1}{2} F_{s/t} \frac{1}{2} \chi_{s/t}^0 \right| k_{e/o} \right\rangle} &= \overline{\left\langle k_{e/o} \left| \frac{1}{4} \chi^0(p, p) (\delta_{p, p_1} \pm \delta_{p, -p_1}) [F(P_1, P_2) \right. \right.} \\ &\quad \left. \left. \pm F(P_1, -P_2)] \chi^0(p_2, p_2) (\delta_{p_2, p'} \pm \delta_{p_2, -p'}) \right| k_{e/o} \right\rangle} \\ &= \frac{1}{2} \overline{\left\langle k_{e/o} \left| \chi^0(p, p) [F(P, P') \pm F(P, -P') \right. \right.} \\ &\quad \left. \left. \pm F(-P, P') + F(-P, -P')] \chi^0(p', p') \right| k_{e/o} \right\rangle}. \end{aligned} \quad (2.163)$$

Thus the even-frequency lattice pairing susceptibility in the singlet or triplet channel projected and normalized by the corresponding form factor is obtained by

$$\frac{\overline{\langle k_{e/o} | \chi_{s/t} | k_{e/o} \rangle}}{\langle k_{e/o} | k_{e/o} \rangle} = \frac{1}{\langle k_{e/o} | k_{e/o} \rangle} \{ \text{eq. (2.161)} + \text{eq. (2.163)} \}. \quad (2.164)$$

Next we consider the odd frequency case. Now the combination (momentum, spin) can be (even, triplet) or (odd, singlet) and here we need to take the frequency form factor, eq. (2.160), into consideration. The lattice bare bubble becomes

$$\begin{aligned} f_{odd}(\omega_n) \overline{\langle k_{e/o} | \chi_{t/s}^0 | k_{e/o} \rangle} f_{odd}(\omega'_n) &= f_{odd}(\omega_n) \overline{\langle k_{e/o} | [\delta_{p'', p'} \mp \delta_{p'', -p'}] \chi^0(p', p') | k_{e/o} \rangle} f_{odd}(\omega'_n) \\ &= 2 \overline{\chi^0(P, P)}, \end{aligned} \quad (2.165)$$

where the odd parity in frequency compensates the minus sign between the delta functions and we again obtain the coarse-grained lattice bubble. Similarly, the reducible vertex contribution becomes

$$\begin{aligned} f_{odd}(\omega_n) \overline{\left\langle k_{e/o} \left| \chi_{t/s}^0 \frac{1}{2} F_{t/s} \frac{1}{2} \chi_{t/s}^0 \right| k_{e/o} \right\rangle} f_{odd}(\omega'_n) &= \frac{1}{2} f_{odd}(\omega_n) \overline{\langle k_{e/o} | \chi^0(p, p) [F(P, P') \mp F(P, -P') \right.} \\ &\quad \left. \mp F(-P, P') + F(-P, -P')] \chi^0(p', p') \right| k_{e/o} \rangle} f_{odd}(\omega'_n). \end{aligned} \quad (2.166)$$

Thus the odd-frequency lattice pairing susceptibility becomes

$$\frac{f_{odd}(\omega_n) \overline{\langle k_{e/o} | \chi_{s/t} | k_{e/o} \rangle} f_{odd}(\omega'_n)}{\langle k_{e/o} | k_{e/o} \rangle} = \frac{1}{\langle k_{e/o} | k_{e/o} \rangle} \{ \text{eq. (2.165)} + \text{eq. (2.166)} \}. \quad (2.167)$$

To reduce the computational burden in the eqs. (2.163) and (2.166), we can coarse-grain the lattice bare bubble with one form factor first:

$$\overline{\overline{\overline{\chi^0(P, P)}}} \equiv \frac{N_c}{N} \sum_{\tilde{\mathbf{k}}} \chi^0(\mathbf{K} + \tilde{\mathbf{k}}, i\omega_n, \mathbf{K} + \tilde{\mathbf{k}}, i\omega_n) \left| k_{e/o} \left(\mathbf{K} + \tilde{\mathbf{k}} \right) \right\rangle}. \quad (2.168)$$

Next we replace $\overline{\langle k_{e/o} | \chi^0(p, p) \rangle}$ and $\overline{\langle \chi^0(p', p') | k_{e/o} \rangle}$ in eqs. (2.163) and (2.166) with $\chi^{\ddot{0}}(P, P)$ with proper indexes, then the momentum calculations in those equations are restricted to the cluster momentum.

The pairing matrix in the eq. (2.149) under a “correct” form factor projection explains the formation of a superconducting dome. For example, the d -wave projected pairing matrix in the square-lattice Hubbard model is

$$M_d = V_d \bar{\chi}_d^0, \quad (2.169)$$

where $\bar{\chi}_d^0 \equiv \langle d | \bar{\chi}^0 | d \rangle / \langle d | d \rangle$. As doping increases from the half filling and $T \sim T_c$, the pairing strength V_d decreases while the bare bubble $\bar{\chi}_d^0$ increases and becomes more diverged near the optimal doping ($n = 0.85$, $t'/t = 0$) then the over-doped region. Theoretically the quantity M_d as function of doping when $T < T_c$ gives the shape of superconducting dome, but we can hardly reach the temperature below T_c due to the minus sign problem in the QMC simulations. Practically we extrapolate $1/\bar{\chi}_d(T)$ to obtain T_c , show doping dependence of V_d and $\bar{\chi}_d^0$ at low enough temperature to see a qualitative behavior of the dome shape, and show temperature dependence of $\bar{\chi}_d^0$ to see how the bare bubble diverges at low T at different doping regions.

2.3.4 Vertex decomposition

The particle-particle vertex can be decomposed into a fully irreducible vertex Λ , a particle-hole ($S = 0$) charge contribution Φ_C and a particle-hole ($S = 1$) spin contribution Φ_S in the even frequency case:[51]¹¹

$$\Gamma^{pp} = \Lambda + \Phi_C + \Phi_S, \quad (2.170)$$

where

$$\Gamma^{pp} = \frac{1}{2} \frac{N_c}{T} \sum_{P, P'} (\Gamma(P, P') + \Gamma(P, -P')), \quad (2.171)$$

with the Γ obtained from the pairing channel of the Bethe-Salpeter equation in eq. (2.132), and

$$\begin{aligned} \Phi_{C/S} &= a \times b \times \frac{1}{2} \frac{N_c}{T} \sum_{P, P'} [(F_{C/S}(-P', P, Q) - \Gamma_{C/S}(-P', P, Q)) \delta_{P-P', -Q} \\ &\quad + (F_{C/S}(-P', -P, Q) - \Gamma_{C/S}(-P', -P, Q)) \delta_{P+P', Q}], \end{aligned} \quad (2.172)$$

where the factor $a = 2$ for charge and $a = 1$ for magnetic (spin) in order to adjust the different definitions of charge and magnetic channels (see the discussion after the eq. (2.135)), and the factor $b = \frac{1}{2}$ for charge and $b = -\frac{3}{2}$ for spin, which are the coefficients from the parquet equations. Now we can project the form factors of interest on the eq. (2.170) to check how the individual component under a specific symmetry contributes to the particle-particle vertex.

¹¹The formula (6) in Maier’s paper[51] has a typo in the sign of Φ_S .

2.4 Maximum Entropy Method

Quantum Monte Carlo (QMC) simulations produces Green's functions G as a function of imaginary time τ or Matsubara frequency $i\omega_n$. To analytic continue $G(\tau)$ or $G(i\omega_n)$ to obtain a real-frequency $G(\omega)$, one needs to invert the integral

$$G(\tau) = \int d\omega A(\omega)K(\tau, \omega), \quad (2.173)$$

or equivalently

$$G(i\omega_n) = \int d\omega A(\omega)K(i\omega_n, \omega), \quad (2.174)$$

where $A(\omega) = -\frac{1}{\pi}ImG(\omega)$ (Fermion) or $A(\omega) = -\frac{1}{\pi\omega}ImG(\omega)$ (Boson), and the kernels K are defined as

$$K(\tau, \omega) = \frac{e^{-\tau\omega}}{1 + e^{-\beta\omega}} \text{ (Fermion) and } K(\tau, \omega) = \frac{\omega [e^{-\tau\omega} + e^{-(\beta-\tau)\omega}]}{1 - e^{-\beta\omega}} \text{ (Boson)}, \quad (2.175)$$

or equivalently

$$K(i\omega_n, \omega) = \frac{1}{i\omega_n - \omega} \text{ (Fermion) and } K(i\omega_n, \omega) = \frac{\omega^2}{\omega^2 + \omega_n^2} \text{ (Boson)}. \quad (2.176)$$

First, this inversion is an ill-posed problem because the small value in the high-frequency tail of kernels gives little information of the spectrum A to G . In other words, infinite solutions exist to find A for a given G . Second, the left hand sides of the integral equations (2.173) and (2.174) are obtained from the QMC and thus have error bars: $\{\langle G_i \rangle \pm \sigma_i\}$. It's intuitive to guess a trial spectrum $A^{trial}(\omega_i)$ in eq. (2.173) and (2.174) to obtain G_i^{trial} and then apply the least-squares method on the QMC data:

$$\chi^2 = \sum_i \frac{(\langle G_i \rangle - G_i^{trial})^2}{\sigma_i^2}. \quad (2.177)$$

However, this least-squares method does not work in general because the values of A^{trial} in all frequencies ω_i are allowed to move independently to minimize χ^2 , and the best estimate A^{trial} may violate causalities (spectrum should be positive in all frequencies $A^{trial}(\omega_i) \geq 0$). Even if we restrict the spectrum to be causal, when $\chi^2 \ll N$ (total number of imaginary time or Matsubara frequency measured in QMC), the spectrum still display artificial noise and oscillations to "over-fit" the QMC data. To solve the problems above, one introduces the concept of default model which is the keystone leads to the success of the Maximum Entropy Method. In the following I will briefly summarize the Maximum Entropy Method based on many theoretical works[52, 53, 54, 55, 56, 57, 58, 59].

Maximum Entropy Method is a method tries to maximize the conditional probability $P(A|G)$, where A is the solution of spectrum to the integral eq. (2.173) and (2.174) based on a given G from the QMC measurement. Use the identity of conditional probability,

$$P(A|G) = P(G|A) \frac{P(A)}{P(G)}, \quad (2.178)$$

where we define $P(A|G)$ as *posterior probability*, $P(G|A)$ as *likelihood function*, $P(A)$ as *prior probability*, and $P(G)$ as *evidence* which is constant because G is measured from the QMC process and is assumed to be equally probably determined.

The likelihood function tells us how precisely the data is measured under a given A^{trial} . $P(G|A^{trial}) = 1$ if and only if $\chi^2 = 0$ and thus

$$P(G|A^{trial}) \propto \exp\left(-\frac{\chi^2}{2}\right), \quad (2.179)$$

where χ^2 is defined as

$$\chi^2 = \sum_{i,j} (G_i^{trial} - \langle G_i \rangle) (C_{i,j}^{-1}) (G_j^{trial} - \langle G_j \rangle), \quad (2.180)$$

and $C_{i,j}$ is called *covariance matrix* and defined as

$$C_{i,j} = \frac{1}{N_b(N_b - 1)} \sum_{k=1}^{N_b} (\langle G_i \rangle - G_i^k) (\langle G_j \rangle - G_j^k), \quad (2.181)$$

where N_b is the number of bins measured in QMC process, the indexes i and j run over the number of imaginary time or Matsubara frequency, and $\langle G_i \rangle = \frac{1}{N_b} \sum_{k=1}^{N_b} G_i^k$. If the errors at different values of τ or $i\omega_n$ are uncorrelated, $C_{i,j}$ is diagonal and the eq. (2.180) becomes the eq. (2.177), and the deviation σ_i can be derived as

$$\sigma_i = \sqrt{\frac{\sum_k (\langle G_i \rangle - G_i^k)^2}{N_b(N_b - 1)}} = \sqrt{\frac{(\langle G_i^2 \rangle - \langle G_i \rangle^2)}{N_b - 1}}. \quad (2.182)$$

But in general $C_{i,j}$ has off-diagonal terms because one cannot completely eliminate the correlations at different τ and $i\omega_n$. Thus we always need to diagonalize the covariance matrix first:

$$U^{-1}CU = \sigma_i^2 \delta_{ij}. \quad (2.183)$$

Second, we transform the kernel and the data G using the matrix U defined above:

$$K' = U^{-1}K \quad G' = U^{-1}G. \quad (2.184)$$

In this diagonal space we can say each G'_i is measured independently. Therefore, we can define the likelihood function (after normalized) as

$$P(G|A) = \frac{1}{Z_L} \exp\left(-\frac{\chi^2}{2}\right), \quad (2.185)$$

where

$$\chi^2 = \sum_i \frac{(\langle G'_i \rangle - \sum_l K'_{i,l} A_l)^2}{\sigma_i'^2}, \quad (2.186)$$

and Z_L is the normalization factor of the likelihood function and defined as

$$Z_L = (2\pi)^{N/2} \prod_i \sigma_i'. \quad (2.187)$$

Next, we introduce a default model to define the *prior probability* $P(A)$. The default model $m_i \equiv m(\omega_i)$ is introduced based on how good a guess of $A_i \equiv A(\omega_i)$ compared with the prior knowledge. According to the information theory, we use the Shannon entropy:

$$S(A) = \sum_i \left(A_i - m_i - A_i \ln \frac{A_i}{m_i} \right). \quad (2.188)$$

This entropy has its maximum at $S(A = m) = 0$, which means that the spectrum A equals to the default model m . If A and m are not identical, the entropy is less than zero. If the prior probability behaves

$$P(A) \propto \exp(S(A)), \quad (2.189)$$

then $P(A) = 1$ if $A = m$ and $P(A) < 1$ if $A \neq m$, indicating the similar degree between the solution A and a given (prior) m . To normalize $P(A)$, we need to approximate the integral by expanding $S(A)$ to second order around the maximum. $S \approx \frac{1}{2} \delta A^T \nabla \nabla S|_{A=m} \delta A = \frac{1}{2} \delta A^T \{1/\mathbf{m}\} \delta A$, where $1/\mathbf{m}$ is the diagonal matrix with elements $1/m_i$, and $\delta A_i = A_i - m_i$. Performing the functional integral, we have the normalization factor Z_S like (using $\int \mathcal{D}A \equiv \int \frac{d^N A}{\prod_i \sqrt{A_i}}$)

$$\begin{aligned} Z_S &= \int \mathcal{D}A \exp(\alpha S) \\ &\approx \int \mathcal{D}A \exp \left\{ \alpha \left(-\frac{1}{2} \delta A^T \{1/\mathbf{m}\} \delta A \right) \right\} \\ &= (2\pi/\alpha)^{N/2}, \end{aligned} \quad (2.190)$$

where α is a regularization factor and will be discussed later. So far we have

$$P(A) = \frac{1}{Z_S} \exp(\alpha S(A)). \quad (2.191)$$

This default model is a key in solving the inversion problem of the high-frequency tail of kernels in eq. (2.173) and (2.174) for that one can always prepare a good default model (like

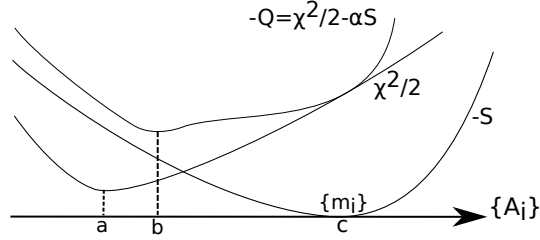


Figure 2.16: Schematic plots for $\chi^2/2$ (eq. (2.186)) and negative entropy $-S$ (eq. (2.188)) and their combination Q (eq. (2.193)) with finite value of α . Point a , c and b show the corresponding minimums, and especially at point c , $S = 0$ and $A = m$.

Gaussian shape) with a well-behaved high-frequency tail. Now if we combine the likelihood function and the prior probability, the posterior probability in eq. (2.178) becomes

$$P(A|G) \propto P(G|A)P(A) \propto \exp(Q), \quad (2.192)$$

with

$$Q = \alpha S - \frac{1}{2}\chi^2, \quad (2.193)$$

where α is a parameter controlling the tendency of data of minimizing the least squares χ^2 and maximizing the information entropy S . If $\alpha \rightarrow \infty$, we force the solution A equals to the default model m ; if $\alpha \rightarrow 0$, there is no prior information from the default model and the whole question goes back to the least-squares method, like eq. (2.177). Figure 2.16 shows three curves representing $\chi^2/2$, $-S$, and $-Q$ curves. Maximum entropy method seeks for maximum solution of $P(A|G)$ or minimum solution of $-Q$. The best estimate spectrum A_i that minimizes $-Q$ is at the point b which is in the range of a to c . The spectrum at the point a corresponds to the guess purely from the least-squares method and may violate causality ($A_i \equiv A(\omega_i) < 0$ for certain ω_i) while the spectrum at the point c does not have extra information compared with the default model. At the point c , the entropy is zero and the spectrum is identical to the default model; while at the point a , the least squares $\chi^2/2$ may not be zero because we choose a causal trial spectrum ($A^{trial}(\omega_i) \geq 0$) such that the QMC data and the guess may not be “best fit”. To obtain a best physical spectrum, one needs to prepare a good default model with a well-behaved high-frequency tail, and set the initial α as large as possible to force the solution spectrum starts to behave similar to the default model so that the spectrum’s high-frequency tail is properly controlled. Next, decrease α to find the maximum value of $P(A|G)$ for each α . For a certain range of α one may find the global maximum of $P(A|G)$ as the solution spectrum. In the following I will summarize three methods to determine α in the literature: *historic*, *classic*, and *Bryan’s* approaches.

Historic approach: Adjust α so that $\chi^2 = N$, where N is the number of imaginary time τ or Matsubara frequency $i\omega_n$. According to eq. (2.186), the right hand side is $O(1)$ for each term and thus $\chi^2 = N$ on average. This approach is just a constraint to prevent $\chi^2 \ll N$, where the solution spectrum is very close to the point a in Fig. 2.16 and the

spectrum, even though it is causal, may display random oscillation and noise especially in the high-frequency region.

Classic approach: Find α that maximizes $P(\alpha|G, m)$. Now we consider α as an extra unknown factor in the posterior probability: $P(A, \alpha|G, m)$. We obtain $P(A|G, m)$ and $P(\alpha|G, m)$ by integrating out α and functional integrating out spectra A . Their relations are

$$\begin{aligned} P(A|G, m) = P(A|G) &= \int d\alpha P(A, \alpha|G) \\ &= \int d\alpha P(A|\alpha, G)P(\alpha|G) \\ &\approx P(A|\hat{\alpha}, G), \end{aligned} \quad (2.194)$$

if $P(\alpha|G)$ is sharply peaked at $\alpha = \hat{\alpha}$ and

$$P(\alpha|G, m) = P(\alpha|G) = \int \mathcal{D}A \left[P(G|A)P(A|\alpha) \frac{P(\alpha)}{P(G)} \right] \quad (2.195)$$

$$= P(\alpha) \int \mathcal{D}A \frac{\exp(Q)}{Z_L Z_S} \quad (2.196)$$

$$= \int \mathcal{D}A \frac{\exp(Q)}{\alpha Z_L Z_S}, \quad (2.197)$$

where we use Jeffrey's prior $P(\alpha) \propto 1/\alpha$, $P(G|A)P(A|\alpha) \propto \exp(Q)$ from the eq. (2.192), $P(G)$ is assumed to be a constant and the normalization factors of likelihood function and entropy are Z_L (eq. (2.187)) and Z_S (eq. (2.190)) respectively. According to eq. (2.194) and eq. (2.195), the spectrum A and α depends on each other and both should be determined iteratively.

Bryan's approach: If $P(\alpha|G)$ is not sharply peaked at $\alpha = \hat{\alpha}$, the classic approach can not be used. Bryan[60] calculates optimal spectrum $\hat{A}(\alpha)$ for each α in a certain range by solving

$$\left. \frac{\delta Q}{\delta A} \right|_{A=\hat{A}} = 0. \quad (2.198)$$

The solution spectrum is taken to be

$$A = \int d\alpha \hat{A}(\alpha) P(\alpha|G, m). \quad (2.199)$$

Analytical continue the self energy of Hubbard model: High-frequency expansion of the self energy of Hubbard model is (Fig. 2.17)

$$\Sigma_\sigma(\mathbf{K}, i\omega_n) = \Sigma_H + \frac{U^2 \chi_{-\sigma, -\sigma}}{i\omega_n} + \mathcal{O}\left(\frac{1}{(i\omega_n)^2}\right) + \dots \quad (2.200)$$

Chapter 3

Role of the van Hove Singularity in the Quantum Criticality of the Hubbard Model

A quantum critical point is found in the phase diagram of the two-dimensional Hubbard model[61]. It is due to the vanishing of the critical temperature associated with a phase separation transition, and it separates the non-Fermi liquid region from the Fermi liquid. Near the quantum critical point, the pairing is enhanced since the real part of the bare d -wave pairing susceptibility exhibits an algebraic divergence with decreasing temperature, replacing the logarithmic divergence found in a Fermi liquid[62]. In this chapter we explore the single-particle and transport properties near the quantum critical point using high quality estimates of the self energy obtained by direct analytic continuation of the self energy from Continuous-Time Quantum Monte Carlo. We focus mainly on a van Hove singularity coming from the relatively flat dispersion that crosses the Fermi level near the quantum critical filling. The flat part of the dispersion orthogonal to the antinodal direction remains pinned near the Fermi level for a range of doping that increases when we include a negative next-nearest-neighbor hopping t' in the model. For comparison, we calculate the bare d -wave pairing susceptibility for non-interacting models with the usual two-dimensional tight binding dispersion and a hypothetical quartic dispersion. We find that neither model yields a van Hove singularity that completely describes the critical algebraic behavior of the bare d -wave pairing susceptibility found in the numerical data. The resistivity, thermal conductivity, thermopower, and the Wiedemann-Franz Law are examined in the Fermi liquid, marginal Fermi liquid, and pseudo-gap doping regions. A negative next-nearest-neighbor hopping t' increases the doping region with marginal Fermi liquid character. Both T and negative t' are relevant variables for the quantum critical point, and both the transport and the displacement of the van Hove singularity with filling suggest that they are qualitatively similar in their effect.

In this work I improved the efficiency of the INT-CTQMC codes, wrote the checkpoint in each DCA iteration to make low-temperature calculations possible. I also developed the MEM code which can analytically continue the self energy with the minus sign in the QMC measurement. I also calculated the transport properties such as resistivity, thermal conductivity, and thermopower using the Kubo's formula. This chapter has been published in the journal of Phys. Rev. B, **84**, 245107 (2011)[23].

3.1 Introduction

A plausible scenario for the high temperature superconductivity in cuprates is based upon the presence of a van Hove singularity corresponding to the saddle points in the single particle energy dispersion[63, 64, 65, 66]. These flat regions in the energy dispersion are directly observed in ARPES experiments on various cuprate compounds[67, 68, 69, 70, 71]. Recently, it was also observed in the tunneling spectra of Bi-2201[72]. The presence of saddle points in the energy dispersion is also argued to lead to a superconducting instability in other

correlated systems, e.g. graphene[73]. If the Fermi level is doped to coincide with the van Hove singularity, then the superconducting transition temperature can be greatly enhanced.

The van Hove scenario is also argued[74, 75, 76] to be responsible for the *marginal Fermi liquid* behavior[77] in which the lifetime broadening of the quasiparticles is of the order of its energy. Thus the van Hove scenario is argued to account for the linear- T resistivity[76, 75, 78], T -independent thermopower[75], anomalous isotope effect[76], etc.

There is numerical evidence for the presence of van Hove singularities in models of strongly correlated systems. The energy dispersion of one hole in an antiferromagnetic background has been considered in studies of the Hubbard model[79, 80] and t - J model[81]. These studies report the presence of extended saddle points. Assaad et al.[79] found that the dispersion has a quartic dependence with momentum near the anti-nodal point $(\pi, 0)$.

These examples of extended saddle points in various correlated superconducting systems, and their proximity to the Fermi level at the doping where the maximum transition temperature occurs, demonstrate that it is extremely important to understand the role played by these singularities. A plethora of scientific efforts have been devoted towards achieving this understanding[82, 83, 84, 85, 86, 87, 88, 89, 90, 91, 92, 93, 94, 95, 96, 97, 98, 99, 100, 101, 102, 103]. At the simplest level, the role of the van Hove singularity may be interpreted within the BCS formalism. Here, the superconducting transition temperature, T_c , is determined by the condition $V\chi'_0(\omega = 0) = 1$, where χ'_0 is the real part of the $\mathbf{q} = 0$ bare pairing susceptibility, and V is the strength of the pairing interaction. In a BCS superconductor, $\chi'_0(\omega = 0)$ displays a logarithmic divergence as $T \rightarrow 0$, yielding the BCS exponential form for T_c . The van Hove singularity enhances the divergence of $\chi'_0(\omega = 0)$, yielding higher transition temperatures.

There is also strong evidence for a quantum critical point located beneath the superconducting dome in the cuprates, and in close proximity to the doping with the maximum T_c [104, 105]. Above the quantum critical point, in a range of doping associated with marginal Fermi liquid behavior, the in-plane resistivity is known to vary linearly with T over a wide range of temperatures[106, 107, 108, 109, 110, 111, 112]. In the Fermi liquid region the low temperature resistivity varies as T^2 . The resistivity increases as the doping decreases from the Fermi liquid into the pseudogap region. Moreover, the thermal conductivity κ [113, 114], the thermopower S [104, 105] and the tunneling conductance g [115] have been investigated near the quantum critical point of the cuprates. κ is observed to be nearly independent of temperature in the marginal Fermi liquid state[116] and depends on $1/T$ in the Fermi liquid region. This is consistent with the Wiedemann-Franz Law[117], $\kappa\rho \propto T$. Chakraborty et al.[104] suggested that the thermopower changes sign abruptly near the optimal doping in most of the cuprate materials, signaling a state with particle-hole symmetry. Also in the marginal Fermi liquid, the tunneling conductance $g(V) \sim g_0 + g_1|V|$, where g_0 and g_1 weakly depend on T and V .

A recent study[61] reported the presence of a quantum critical point in the two-dimensional Hubbard model, where the quasiparticle spectral weight becomes zero. This quantum critical point separates the non-Fermi liquid pseudogap from the Fermi liquid region, and is surrounded by a superconducting dome (c.f. the inset in Fig. 3.1). At finite temperatures, the Fermi liquid and pseudogap regions are separated by the marginal Fermi liquid. Interest-

ingly, at the quantum critical point, the density of states is found to be nearly particle-hole symmetric at low frequencies with a sharp peak at $\omega = 0$. This filling is tantalizingly close to the optimal doping where the superconducting transition temperature T_c attains its maximum. The proximity of the superconducting dome to the quantum critical point was recently investigated by [62]. Unlike the BCS case, they found that the bare d -wave pairing susceptibility $\chi'_{0d}(\omega = 0)$ diverges algebraically as $\frac{1}{\sqrt{T}}$ at the quantum critical point, thus leading to a strongly enhanced T_c . Using the Kramers-Krönig relation between the real part and the imaginary part of the susceptibility, $\chi'_{0d}(T) = \frac{1}{\pi} \int \frac{\chi''_{0d}(\omega)}{\omega} d\omega$, the algebraic divergence of $\chi'_{0d}(T)$ was found to come from a scaling behavior of the imaginary part $\chi''_{0d}(\omega)$. When $T^{3/2}\chi''_{0d}(\omega)/\omega$ is plotted against ω/T , the different temperature curves fall on top of each other when $\omega \geq T_s \equiv 4tT/J$, determining a scaling function $H(x)$ such that $T^{3/2}\chi''_{0d}(\omega)/\omega = H(\omega/T) \approx (\omega/T)^{-3/2}$ (see Fig. 3.1). The contribution from H to $\chi'(T) = \frac{T^{-3/2}}{\pi} \int H(\omega/T) d\omega \propto T^{-1/2}$ which will dominate at low T .

Since this enhanced behavior is expressed in the bare pairing bubble, dressed by the self energy but with no vertex corrections, this discussion naturally raises the question about the role played by the van Hove singularity in the quantum criticality and its possible connection to the superconducting T_c . In this chapter, we use the dynamical cluster quantum Monte Carlo method to explore the relationship between the quantum critical point and the van Hove singularity for high-temperature superconductivity in the Hubbard model. We obtain high quality estimates of the real-frequency single-particle self energy $\Sigma(\mathbf{K}, \omega)$ at the cluster momenta \mathbf{K} by direct analytic continuation of the Matsubara frequency self energy $\Sigma(\mathbf{K}, i\omega_n)$ using the maximum entropy method [57, 118]. This direct method avoids the artifacts on the self energy that come about by inverting the coarse-grained Dyson's equation [57] (eq. (2.27)). In the model without next-nearest-neighbor hopping ($t' = 0$), we find that, as we dope the system across the quantum critical filling, a flat region in the dispersion crosses the Fermi level, accompanied by a sharp nearly symmetric peak in the density of states which also passes through the Fermi level. We find that the resistivity follows a linear- T dependence over a wide range of temperatures yet a narrow range of doping (see Fig. 3.14). We use these high quality estimates of the self energy to calculate the bare pairing susceptibility, we again find the collapse of the data found in Fig. 3.1. To understand the role played by the van Hove singularity in determining this critical behavior, we have calculated the pairing susceptibility in the d -channel for two non-interacting models at half filling - the standard quadratic dispersion and a hypothetical quartic dispersion. While the quartic dispersion can yield the observed algebraic divergence of $\chi'_{0d}(\omega = 0)$, neither dispersion produces the collapse of the data found in Fig. 3.1, suggesting that a van Hove singularity alone does not capture this phenomena. For negative t' , the resistivity follows a linear- T behavior over a wider range of doping, and the sharp peak in the density of states and the flat region of the dispersion linger near the Fermi level for the same wider range of doping. These results suggest that the doping region affected by quantum criticality at low temperature becomes larger when $t' < 0$. We also show that the zero-frequency imaginary part of the self energy

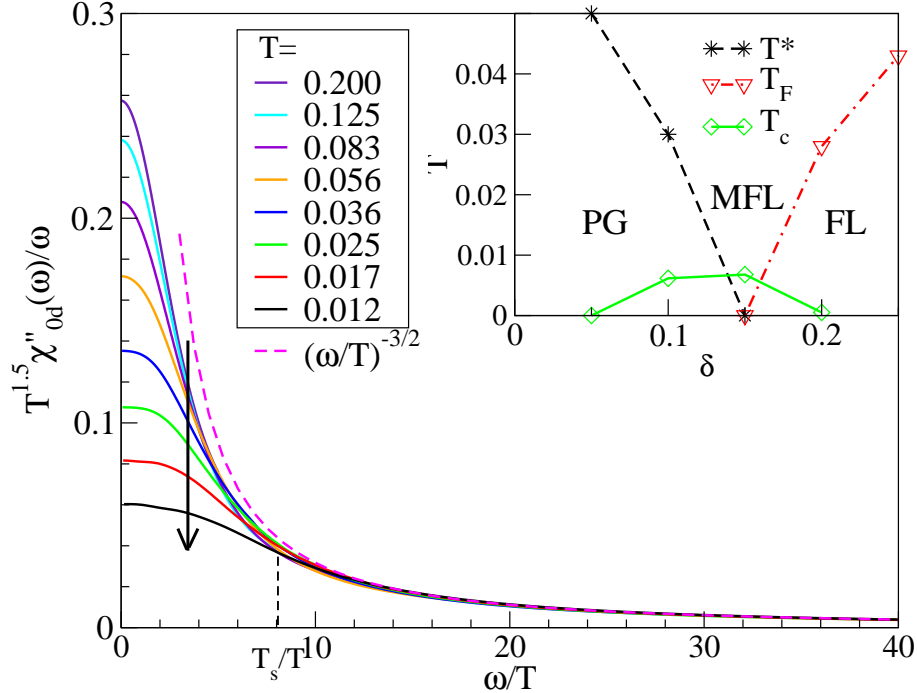


Figure 3.1: (Color online) Frequency dependence of the imaginary part of the particle-particle d -wave susceptibility obtained from the Dynamical Cluster Approximation for various temperatures at the critical filling $n = 0.85$ when $U = 6t$, $t' = 0$ and $4t = 1$. The arrow denotes the direction of decreasing temperature. All the curves fall on top of each other for frequencies greater than $T_s/T \approx 4t/J$. The inset shows the phase diagram for the same parameters (t , t' and U) including the Fermi Liquid (FL), Marginal Fermi Liquid (MFL) and Pseudogap (PG) regions. The lines indicate the d -wave transition temperature T_c (determined by extrapolation of data from $N_c = 8, 12$ and 16 site clusters), the pseudogap temperature T^* , and the Fermi liquid temperature T_F . (Taken from Yang et al.[62]) The quasiparticle fraction on the Fermi surface vanishes at the quantum critical point where $T^* = T_F = 0$, and remains zero in the pseudogap region[61].

$\Sigma''(T, \omega = 0)$, the dominant contribution to the resistivity, has a wider range of linear- T behavior for $t' < 0$ than $t' = 0$. All this motivates us to speculate a phase diagram near the quantum critical point in the discussion section.

This chapter has been organized as follows. Section 3.2 briefly outlines the model and methods used in this study. Results are presented in section 3.3. Single particle properties are discussed in section 3.3.1; the pairing susceptibility calculation in section 3.3.2, the effect of t' on the dispersion in 3.3.3, and transport results in 3.3.4. The chapter is concluded with the discussion in section 3.4.

3.2 Formalism

In this work, we look for direct evidence of the van Hove singularity and marginal Fermi liquid behavior in the spectra, electronic dispersion, and transport properties of the two-dimensional Hubbard model which is defined in the eq. (2.1) and (2.23) with the bare dispersion given in the eq. (2.3).

We employ the Dynamical Cluster Approximation (DCA)[119, 45] with a quantum Monte Carlo algorithm as the cluster solver. The DCA is a cluster mean-field theory that maps the original lattice onto a periodic cluster of size $N_c = L_c^2$ embedded in a self-consistently determined host. This many-to-one map is accomplished by dividing the lattice Brillouin zone into cells centered at momenta \mathbf{K} , and coarse graining the lattice Green's functions by summing over the momenta labeled with \tilde{k} within each cell. The coarse grained eq. (2.27) is rewritten as

$$\bar{G}(\mathbf{K}, \omega) = \frac{N_c}{N} \sum_{\tilde{k}} G(\mathbf{K} + \tilde{k}, \omega), \quad (3.1)$$

where \bar{G} and G are the coarse-grained and the lattice single-particle propagators, respectively. The coarse-grained Green's function defines the cluster problem. Spatial correlations up to a range L_c within the cluster are treated explicitly, while those at longer length scales are described at the mean-field level. However the correlations in time, essential for quantum criticality, are treated explicitly for all cluster sizes. To solve the cluster problem, we use continuous-time quantum Monte Carlo[49], which has no Trotter error,[120] and the Hirsch-Fye quantum Monte Carlo method[121, 122] for the charge polarizability in Fig. 3.2. We employ the maximum entropy method[57] to calculate the real-frequency spectra.

3.2.1 Calculation of Single-Particle Spectra

In previous calculations of the single-particle spectra, we analytically continue the quantum Monte Carlo $\bar{G}(\mathbf{K}, \tau)$ to obtain $\bar{G}(\mathbf{K}, \omega)$ then invert the coarse-graining Eq. (3.1) to obtain the self energy $\Sigma(\mathbf{K}, \omega)$. This last step can introduce spurious features in $\Sigma(\mathbf{K}, \omega)$. As observed previously[118], it is better to analytically continue the self energy directly. In this section we paraphrase the paragraph of continuing self energies in the section 2.4. Because the self energy spectra does not share the normalization of $\int d\omega \bar{A}(K, \omega) = 1$, where $\bar{A}(\mathbf{K}, \omega) = -\frac{1}{\pi} \bar{G}''(\mathbf{K}, \omega)$. This normalization is a desirable feature since it allows us to treat the spectrum as a normalized probability distribution. Since the Hubbard self energy $\Sigma(\mathbf{K}, i\omega_n) = \Sigma_H + U^2 \chi_{\sigma,\sigma} / i\omega_n + \dots$, where $\chi_{\sigma,\sigma} = \langle n_\sigma n_\sigma \rangle - \langle n_\sigma \rangle^2 = n_\sigma(1 - n_\sigma)$ is the local polarizability of a single spin species σ , and $\Sigma(\mathbf{K}, i\omega_n) - \Sigma_H = \int d\omega -\frac{1}{\pi} \frac{\Sigma''(\mathbf{K}, \omega)}{i\omega_n - \omega}$. It is easy to see that the integral of $\Sigma(K, i\omega_n) - \Sigma_H$ is $U^2 \chi_{\sigma,\sigma}$. Therefore we will analytically continue

$$\frac{\Sigma(\mathbf{K}, i\omega_n) - \Sigma_H}{U^2 \chi_{\sigma,\sigma}} = \int d\omega \frac{\sigma(\mathbf{K}, \omega)}{i\omega_n - \omega}, \quad (3.2)$$

where $\sigma(\mathbf{K}, \omega) = -\frac{1}{\pi} \Sigma''(\mathbf{K}, \omega) / U^2 \chi_{\sigma,\sigma}$, $\int d\omega \sigma(\mathbf{K}, \omega) = 1$, using $\chi_{\sigma,\sigma}$ calculated in the Monte Carlo process. After that we obtain the lattice self energy $\Sigma(\mathbf{k}, \omega)$ by interpolating the cluster self energy $\Sigma(\mathbf{K}, \omega)$ to get the single-particle spectral function $A(\mathbf{k}, \omega)$.

3.2.2 d -wave Pairing Susceptibility

We calculate the susceptibility in the d -wave channel to the pair field $\mathcal{V} = -f_d b_d^\dagger + \text{h.c.}$ for various models with a van Hove singularity at the Fermi level. Here $b_d^\dagger = \frac{1}{2} \sum (b_{i+\hat{x}}^\dagger - b_{i+\hat{y}}^\dagger)$ is the singlet creation operator, where $b_{i+\hat{\alpha}}^\dagger$ creates a singlet at bond i -($i + \hat{\alpha}$), $\alpha = x, y$, and f_d is a complex constant. The non-interacting d -wave pairing susceptibility χ_{0d} can be computed by calculating the susceptibility bubble

$$\chi_{0d}(T) = T \sum_{\mathbf{k}, i\omega_n} g_d^2(\mathbf{k}) G^0(\mathbf{k}, i\omega_n) G^0(-\mathbf{k}, -i\omega_n), \quad (3.3)$$

where $g_d(\mathbf{k})$ is the d -wave form factor given by $g_d(\mathbf{k}) = \cos k_x - \cos k_y$. $G^0(\mathbf{k}, i\omega_n)$ is the non-interacting Green function given by

$$G^0(\mathbf{k}, i\omega_n) = \frac{1}{i\omega_n - \epsilon_{\mathbf{k}}^0}, \quad (3.4)$$

with $\epsilon_{\mathbf{k}}^0$ the bare band dispersion in Eq.(2.3). χ_{0d} can be evaluated using standard Matsubara summation which gives

$$\chi_{0d}(T) = \sum_{\mathbf{k}} g_d^2(\mathbf{k}) \left(\frac{1 - 2f_{\mathbf{k}}}{2\epsilon_{\mathbf{k}}^0} \right), \quad (3.5)$$

where $f_{\mathbf{k}}$ is the Fermi function.

3.2.3 Transport Coefficients

To explain the anomalous transport properties of the marginal Fermi liquid, Varma et al[77, 123]. postulate that for a wide range of wavevectors \mathbf{q} , excitations make a contribution to the absorptive spin and charge polarizabilities reflected by

$$\chi''(\mathbf{q}, \omega) \propto \min(|\omega/T|, 1) \text{sign}(\omega). \quad (3.6)$$

Electrons scattering from these excitations acquire a self energy

$$\Sigma(\mathbf{k}, \omega) \propto \omega \ln(x/\omega_c) - i\pi x/2, \quad (3.7)$$

where $x = \max(|\omega|, T)$, and ω_c is a cutoff. The marginal Fermi liquid ansatz has several consequences on experimentally relevant quantities, including transport anomalies, such as the linear- T electrical resistivity, the tunneling conductance $g(V) \sim g_0 + g_1|V|$, the photoemission, the nuclear relaxation rate $T_1^{-1} \sim aT + b$, the optical conductivity $\sigma(\omega)$, the Raman scattering, and the superconductive pairing. For the specific heat $C_v(T)$ and thermal conductivity $\kappa(T)$, Varma argued that the normal state's electronic contribution is hard to extract from the experimental data due to the large phonon contribution. The electronic thermal conductivity for the marginal Fermi liquid approximates to a constant because the Wiedemann-Franz law roughly holds.

To calculate the various Onsager transport coefficients we use the Kubo formula[124]:

$$L_{\alpha\beta}^{ij} = \pi \int d\omega \left(-\frac{df}{d\omega} \right) \omega^{i+j-2} \mathcal{D}_{\alpha\beta}(\omega), \quad (3.8)$$

where f is the Fermi function and

$$\mathcal{D}_{\alpha\beta}(\omega) = \frac{1}{N} \sum_{\mathbf{k}} v^{\alpha}(\mathbf{k}) v^{\beta}(\mathbf{k}) A(\mathbf{k}, \omega)^2, \quad (3.9)$$

where $v^{\alpha}(\mathbf{k})$ is the α -component of the electron group velocity and $A(\mathbf{k}, \omega)$ is the single-particle spectral function. The different transport coefficients are given by combinations of L^{ij} . For example, in units where $e = 1$ and the chemical potential $\mu = 0$, the resistivity $\rho(T) = 1/L^{11}$, the thermopower $S = -L^{12}/TL^{11}$, the thermal conductivity $\kappa = \frac{1}{T} (L^{22} - (L^{12})^2/L^{11})$, and the Peltier coefficient $\Pi = L^{21}/L^{11}$.

We note that a simpler estimate exists for the thermopower S . Here, we perform a Sommerfeld expansion of L^{12} at the Fermi level and get an alternative form:

$$S = -\frac{\pi^2}{3} T \frac{\partial \log[\mathcal{D}_{\alpha\beta}(\omega)]}{\partial \omega} \Big|_{\omega=0}. \quad (3.10)$$

If the electron group velocity is a constant, and the square of the single-particle spectra is approximated by $\delta(\omega - \epsilon_{\mathbf{k}})\tau_{\mathbf{k}}$, where $\tau_{\mathbf{k}}$ is the relaxation time, also assumed constant, the thermopower over temperature becomes just the derivative of the logarithm of the density of states at the Fermi level[125].

3.3 Results

3.3.1 Single Particle Properties for $t' = 0$

We first explore the charge polarizability in the marginal Fermi liquid region at $n = 0.85$. The imaginary component of the local charge polarizability $\chi_c''(\mathbf{r} = 0, \omega)$ is plotted in Fig. 3.2. The main plot shows $\chi_c''(\mathbf{r} = 0, \omega)$ divided by its initial slope at zero frequency (determined in the inset), so that the curves coincide for low ω . At higher frequencies, the curves break from this linear rise at a frequency roughly proportional to the temperature. The inset shows that the zero frequency slope, $\chi_c''(\mathbf{r} = 0, \omega)/\omega|_{\omega=0}$, is roughly linear in inverse temperature up to $T \approx 0.2$ or roughly $2J = 8t^2/U$. These features are consistent with the marginal Fermi liquid polarizability in Eq. (3.6). The spin polarization (not shown) does not display such an extended region of marginal Fermi liquid character. This result is consistent with marginal Fermi liquid behavior due to the proximity of a quantum critical point associated with phase separation.

Fig. 3.3 shows the frequency dependence of the imaginary self energy at the Fermi momenta along the anti-nodal ($X\Gamma$) and the nodal (ΓM) directions for three fillings: $n = 0.75$ (Fermi liquid), $n = 0.85$ (marginal Fermi liquid) and $n = 0.95$ (pseudo-gap). For the self energy at $n = 0.75$, the quadratic dashed line (bottom right panel) provides a good fit to $\Sigma''(\mathbf{k}_F, \omega)$ for small ω , as expected from the Fermi liquid theory[126]. The marginal Fermi liquid self energy has a form given by Eq. (3.7), which states that the imaginary self

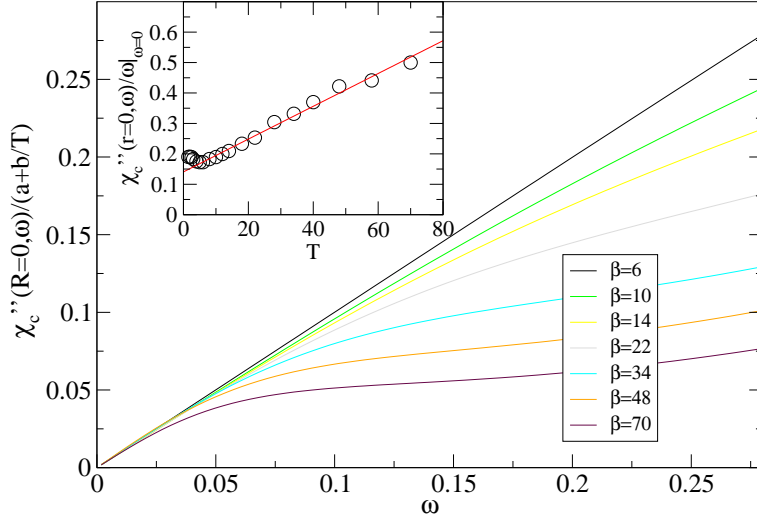


Figure 3.2: (Color online) The local $r = 0$ imaginary part of the dynamical charge polarizability divided by the initial slope at $\omega = 0$, for $n = 0.85$, $U = 6t$, $4t = 1$, $t' = 0$ and $N_c = 16$. It satisfies the marginal Fermi liquid form given by Eq. (3.6). Inset: the zero frequency slope of $\chi_c''(r = 0, \omega)$ is roughly linear in inverse temperature, as expected. The line is a linear fit to the expression $a + b/T$.

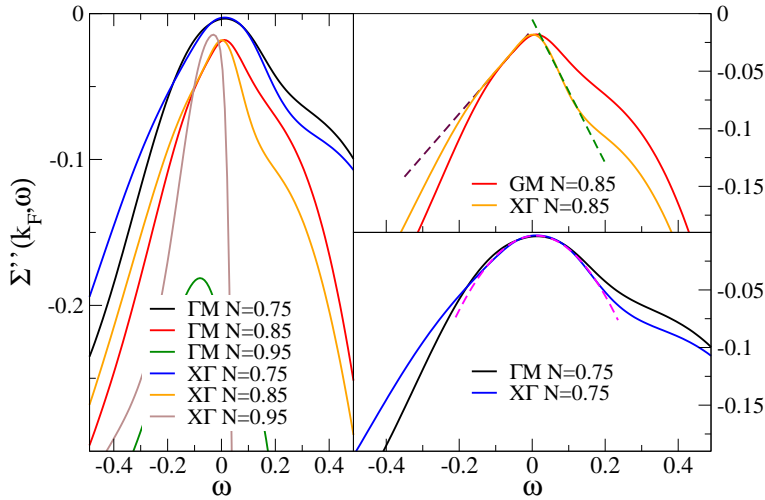


Figure 3.3: (Color online) Frequency dependence of the imaginary part of the self energy at the Fermi momenta, $\Sigma''(\mathbf{k}_F, \omega)$, along ΓM and $X\Gamma$ for $U = 6t$, $4t = 1$, $t' = 0$, $N_c = 16$ and $\beta = 58$. Right panels show a zoom of the low frequency region. Dashed lines fit the data linearly for $n = 0.85$ and quadratically for $n = 0.75$.

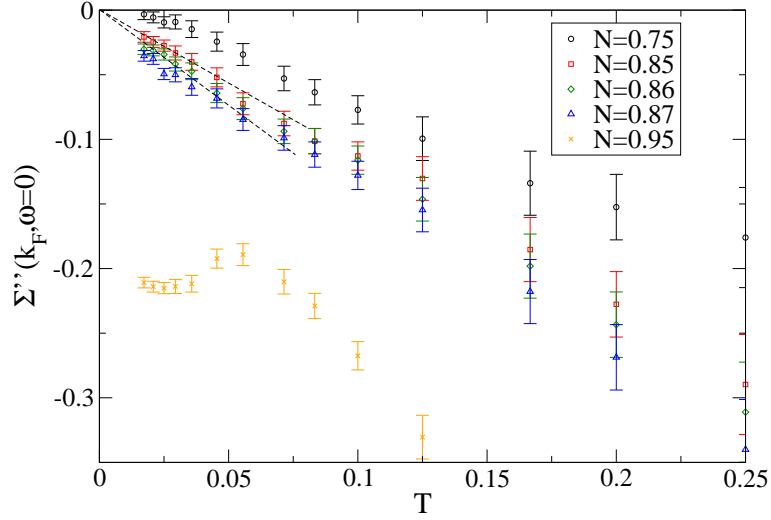


Figure 3.4: (Color online) Temperature dependence of the imaginary part of the self energy $\Sigma''(\mathbf{k}_F, \omega = 0)$ at the Fermi energy and momenta, $U = 6t$, $4t = 1$, $t' = 0$ and $N_c = 16$. The linear dashed lines fit the self energies for $n = 0.85$ and 0.86 below $T = 0.031$.

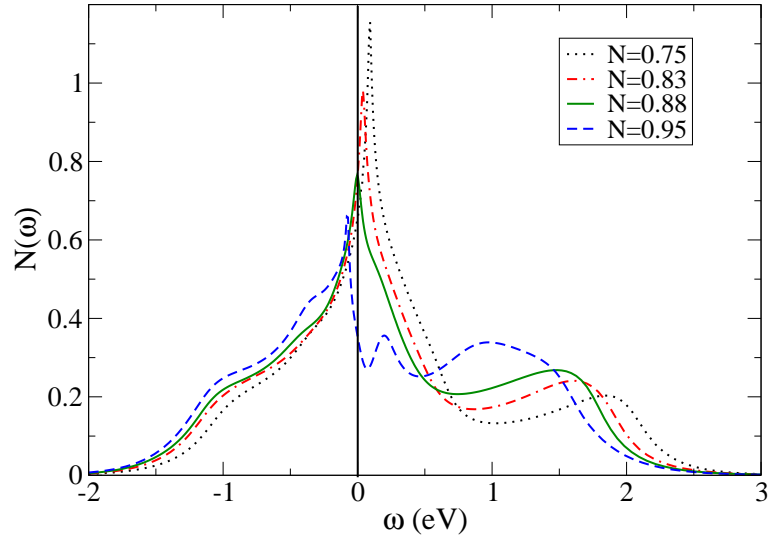


Figure 3.5: (Color online) The single-particle density of states for $t' = 0$, $U = 6t$, $4t = 1$, $N_c = 16$ and $\beta = 58$. The density of states shows low-energy particle-hole symmetry at the filling of $n = 0.88$.

energy is proportional to the negative temperature for small frequency and to the negative ω when the temperature is low. The marginal Fermi liquid self energy in Fig. 3.3 (upper right panel) shows a linear behavior, but interestingly with *different* slopes for positive and negative ω . This is not consistent with Eq. 3.7, but this may be due to the presence of some short range order. I.e., Markiewicz et al.[127] calculated the self-energy due to the random-phase approximation (RPA) magnetic polarizability for a single band model with dispersion obtained by a fitting to the tight binding local-density approximation. They found that the self-energy has linear forms but with different slopes on positive and negative ω when the van Hove singularity is at the Fermi level and quadratic otherwise.

Fig. 3.4 shows the temperature dependence of the self energy when $\omega = 0$ and $t' = 0$. Again we find a result consistent with Eq. 3.7, $\Sigma''(\mathbf{k}_F, \omega \rightarrow 0) \propto -T$, around the marginal Fermi liquid filling for $n = 0.85$ and 0.86 . The dashed lines are linear fits. The error bars are estimated by changing the random seeds in the Monte Carlo calculation. However, they do not reflect the systematic error that comes from the bias towards the default model, which in this case is the spectra from the next higher temperature. This error is largest at low T where the data is weak due to the minus sign problem.

The self energy and dynamic charge polarizability near the critical filling $n_c = 0.85$ are generally consistent with Varma's marginal Fermi liquid ansatz, as are the results found previously for the kinetic and potential energies which vary with temperature like $T^2 \ln(T)$ [128] and the vanishing wave function renormalization factor[61]. To understand the relationship of these results to the van Hove singularity, we will explore the density of states and the quasiparticle dispersion.

The density of states for several fillings is shown in Fig. 3.5. Since we have highly enhanced the quality of the self energy by *direct* analytic continuation of $\Sigma(\mathbf{K}, i\omega_n)$, the density of states in Figure 3.5 shows sharper features as compared to the results of Vidhyadhiraja et al[61]. As the doping decreases from the Fermi liquid to the pseudo-gap region, the peak of the density of states moves from positive to negative energy while its intensity is reduced. For $n = 0.95$, a pseudogap begins to open and a peak to form at positive frequencies. The half-filled case ($n = 1$, not shown) shows upper and lower Hubbard bands located at positive and negative frequencies, respectively. The density of states for filling 0.88 , close to the critical filling of 0.85 , shows low-frequency particle-hole symmetry.

Fig. 3.6 shows the dispersion obtained from the peaks of the spectral function $A(\mathbf{k}, \omega)$ for four fillings: $n = 0.85, 0.87, 0.88$ and 0.95 , along the anti-nodal direction and around the Fermi vector \mathbf{k}_F . In order to define \mathbf{k}_F we look for the maximum value of the zero frequency spectral function $A(\mathbf{k}, \omega = 0)$. In the Fermi liquid and marginal Fermi liquid regions, this definition is roughly equivalent to the Luttinger surface defined where $G'(\mathbf{k}, \omega = 0)$ changes sign. The two definitions yield different results for the pseudogap region, especially when $t' < 0$ which enhances the pseudogap. However, this difference is not large enough to qualitatively change our results or to change any of our conclusions. Therefore, for simplicity, we only show results using the first definition of \mathbf{k}_F . For a particular filling, the left panel shows the dispersion along the k_x direction ($k_y = 0$), while the right panel shows the dispersion along k_y ($k_x = k_{Fx}$). A common identifiable feature for all fillings is the presence of a flat region in the dispersion. This flat region is responsible for the van Hove singularity in the

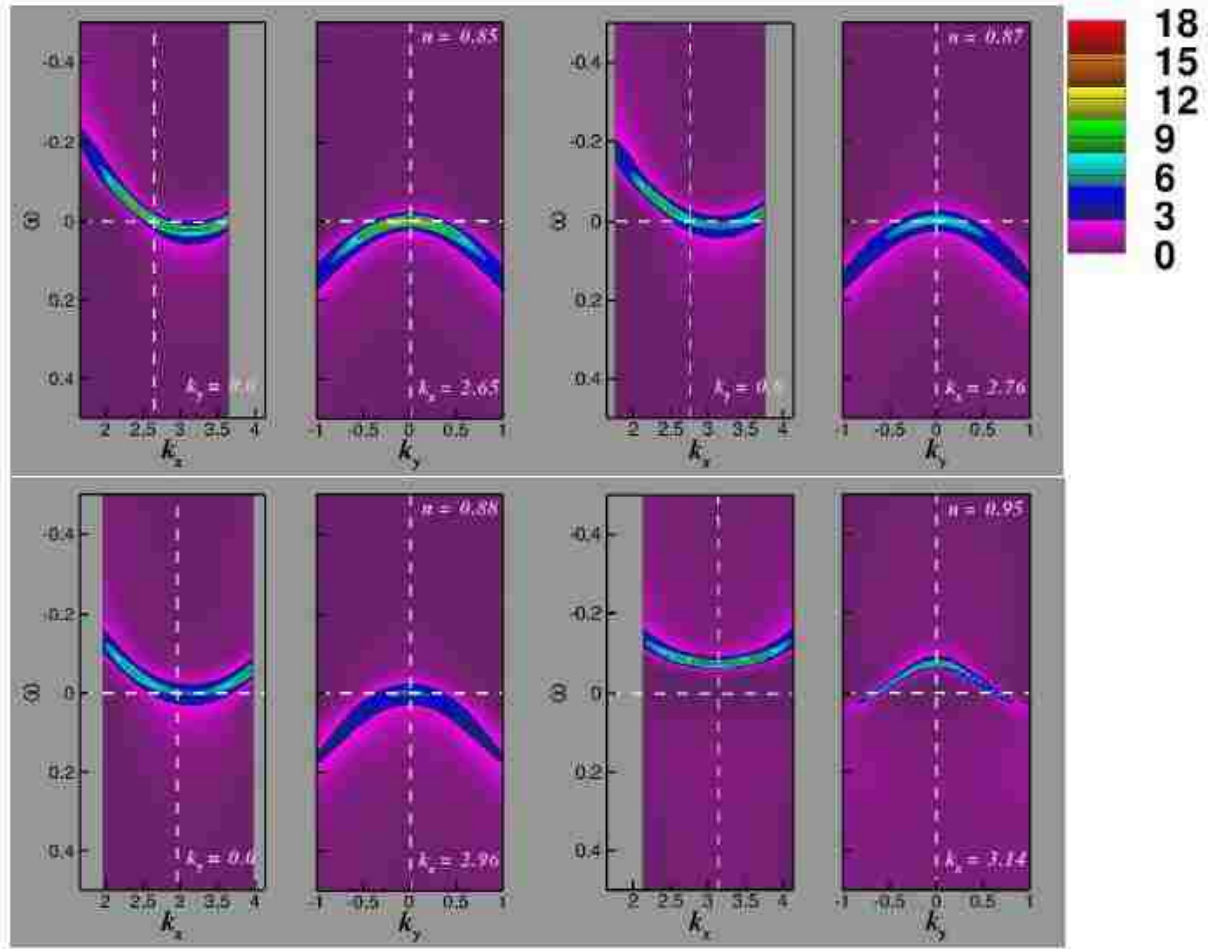


Figure 3.6: (Color online) Energy dispersion obtained from the peaks of the spectral function $A(\mathbf{k}, \omega)$ for various fillings around the Fermi vector \mathbf{k}_F along the anti-nodal direction for $t' = 0$, $U = 6t$, $4t = 1$, $N_c = 16$ and $\beta = 58$. By fixing $k_y = 0$ we explore the dispersion along the k_x direction, and for $k_x = k_{Fx}$ the dispersion along the k_y direction is plotted. Notice that the energy axes are inverted so that positive energies are plotted down. The dispersion along the k_y direction remains pinned near the Fermi level for a range of doping near the center of the superconducting dome (c.f. the inset of Fig. 3.1) while the dispersion along the k_x direction crosses the Fermi level continuously without being pinned.

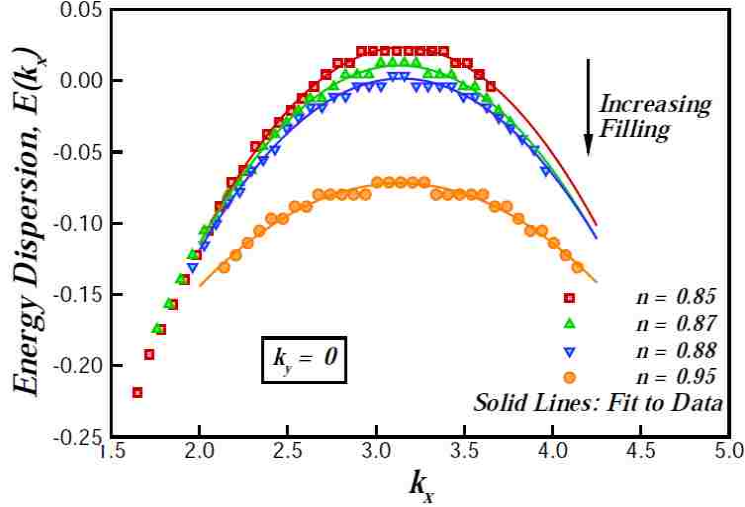


Figure 3.7: (Color online) Single particle dispersion around the Fermi energy taken along the anti-nodal direction ($k_y = 0$). The data is from Fig. 3.6. The solid lines are fits to a quadratic dispersion.

density of states. The van Hove singularity passes through the Fermi level at a filling of $n \approx 0.88$, which is near the quantum critical filling, $n \approx 0.85$, where the quasi-particle weight Z goes to zero[61]. At this filling, the topology of the Fermi surface also changes from hole-like (closed around the point $\mathbf{k} = (\pi, \pi)$) to electron-like (closed around $\mathbf{k} = (0, 0)$) with increasing filling (not shown) as seen in experiment[129]. The dispersion along the k_y direction remains pinned near the Fermi level for a range of doping near the center of the superconducting dome, while the dispersion along the k_x direction passes continuously through the Fermi level. This anisotropic motion of the flat dispersion is consistent with a van Hove peak which moves continuously through the Fermi level as shown in Fig. 3.5, and would correspond to a flat region at the Fermi level which is most isotropic at the crossing and shrinks to narrow pencil-like regions for fillings above and below the crossing.

The dispersion along the anti-nodal direction as a function of k_x for various fillings is displayed in Fig. 3.7. Interestingly, a quadratic form fits well to the data for all fillings. Next, we investigate if such a dispersion can capture the critical algebraic divergence of the pairing susceptibility.

3.3.2 Pairing Susceptibility

The density of states and the dispersion show clear evidence for a van Hove singularity which crosses the Fermi level near the critical filling. In order to see whether the van Hove singularity alone is sufficient to explain the enhanced bare pairing bubble, we calculate the pairing susceptibility in the d -wave channel for two simple models having a van Hove singularity at the Fermi level. We begin with the tight binding model given by Eq. (2.3) at half filling and $t' = 0$. The associated density of states has a logarithmic singularity at $\epsilon = 0$, $N(\epsilon) = \log|\epsilon|$. The temperature dependence of χ'_{0d} can be obtained by converting

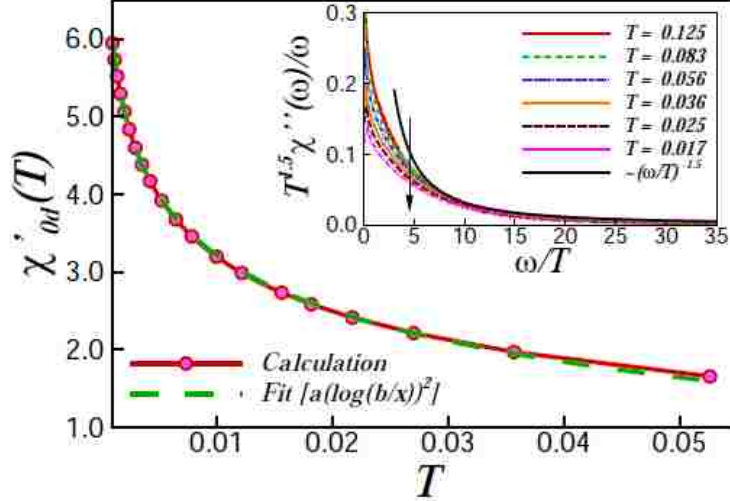


Figure 3.8: (Color online) Temperature dependence of the real part of the particle-particle d -wave susceptibility at $\omega = 0$ for the two-dimensional tight binding dispersion at half filling. Note that χ'_{0d} diverges logarithmically as $T \rightarrow 0$. Inset: Frequency dependence of the imaginary part of the particle-particle d -wave susceptibility. Note that the curves corresponding to various temperatures do not scale at large frequency. The arrow denotes the direction of decreasing temperature.

Eq. (3.5) to an integral over energy with a temperature T cutoff. It results in a $-(\log T)^2$ behavior. This is confirmed by explicit calculation of the sum in Eq. (3.5) as illustrated in Fig. 3.8. As shown in the inset, the imaginary part does not show scaling behavior as seen in Fig. 3.1.

We also consider the next higher order model allowed by the symmetry of the square lattice, a hypothetical model with a quartic dispersion

$$\epsilon_{\mathbf{k}} = -\frac{4}{\pi^4} ((|k_x| - \pi)^4 - k_y^4). \quad (3.11)$$

Such an extended form has been observed in experiments[68] and also confirmed by theoretical studies[80]. The low energy density of states for the quartic dispersion becomes $N(\epsilon) \sim 1/\sqrt{|\epsilon|}$ [89]. Following a similar logic as we used for the tight binding dispersion, for a quartic dispersion, we get

$$\chi'_{0d} \sim \frac{1}{\sqrt{T}} \quad (3.12)$$

Results for the explicit calculation (Eq. (3.5)) are shown in Fig. 3.9, and are consistent with the analytical arguments above. Though the temperature dependence of the real part of the bare susceptibility is found to be algebraic for this quartic dispersion, the inset reveals that the imaginary pairing susceptibility does not exhibit the scaling found by Yang et al[62]. Thus, the simple non-interacting picture of the van Hove singularity at the Fermi level does not completely describe the true temperature and frequency dependence of the susceptibility.

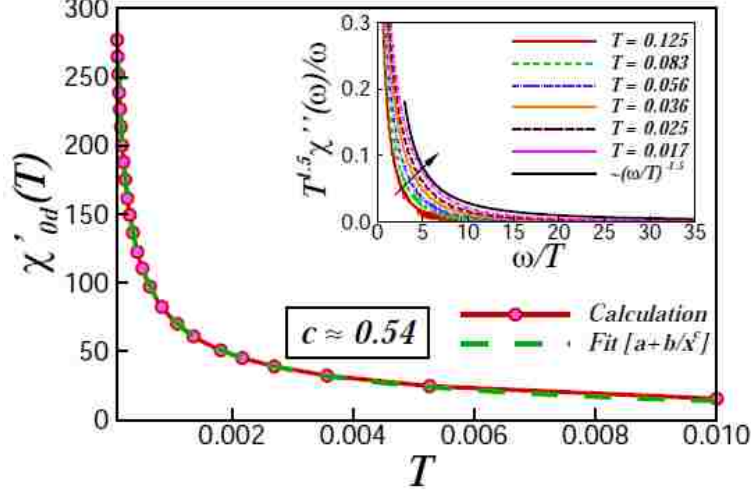


Figure 3.9: (Color online) Temperature dependence of the real part of the particle-particle d -wave susceptibility at $\omega = 0$ for the quartic dispersion of Eq. (3.11) at half filling. Note that χ'_{0d} diverges algebraically $\sim 1/\sqrt{T}$ as $T \rightarrow 0$. A fit to $a+b/x^c$ gives values of $a = -10.6$, $b = 1.98$ and $c = 0.54$. Inset: Frequency dependence of the imaginary part of the pairing d -wave susceptibility. Note that the curves corresponding to various temperatures does not scale well at large frequency. The arrow denotes the direction of decreasing temperature.

3.3.3 Effect of negative t'

The single-band Hamiltonian used to model the hole-doped cuprates generally includes a negative next-nearest-neighbor hopping t' . For $t' = -0.1t$, the temperature dependence of the self energy at the Fermi momenta and energy is shown in Fig. 3.10. We find that $\Sigma''(\mathbf{k}_F, \omega = 0)$ follows a linear behavior over a wider range of fillings, from $n = 0.83$ to 0.87.

Fig. 3.11 demonstrates that the inclusion of a negative t' also results in the pinning of the flat part of the k_y -dispersion to the Fermi level. However, now the pinning is observed for a larger range of fillings, roughly 0.80 to 0.86. Thus both measurements, the temperature dependence of the self energy and the pinning of the flat dispersion to the Fermi level, are consistent. If we take the viewpoint that the quantum critical point and the pinning of the dispersion along k_y to the Fermi level are concomitant aspects of quantum criticality, then a negative t' leads to a larger range of quantum critical fillings. We will also see the signature of this behavior in various transport properties discussed in Section 3.3.4.

Fig. 3.12 shows the density of states for $t'/t = -0.1$ and various fillings as a function of ω . For a given filling, the inset of Fig. 3.12 shows that the peak in the density of states is slightly shifted to smaller frequencies when compared with the peak in the density of states for $t' = 0$. It displays particle-hole symmetry roughly at $n = 0.84$, not $n = 0.88$ as for $t' = 0$. Moreover, if we use $\Delta\omega_p/\Delta n$, where ω_p is the location of peak in the density of states and n is the filling, to estimate the rate at which the peak crosses the Fermi level, we find that the peak of the density of states for $t' = 0$ crosses the Fermi level more quickly than the peak for negative t' . This can be seen in the inset of Fig. 3.12, where the filling dependence of

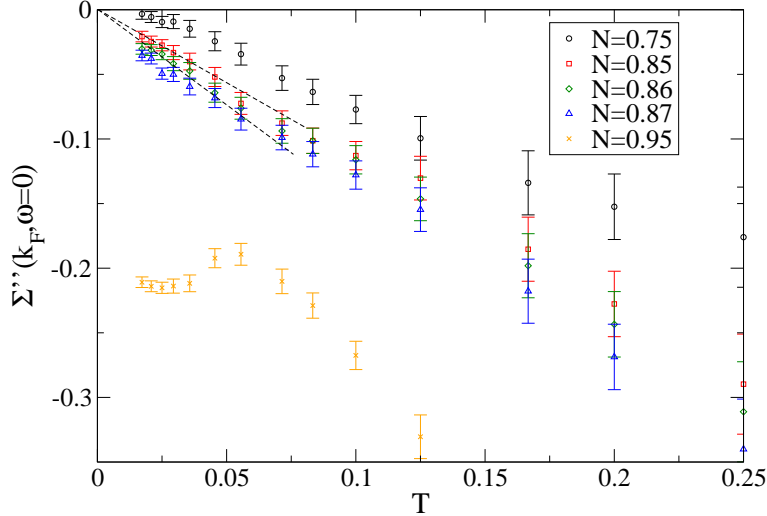


Figure 3.10: (Color online) Temperature dependence of the imaginary part of the self energy $\Sigma''(\mathbf{k}_F, \omega = 0)$ at the Fermi energy and momenta, $U = 6t$, $N_c = 16$, $4t = 1$, and $t'/t = -0.1$. The self energy for filling between $n = 0.83$ and 0.87 shows a linear- T behavior.

the peak location has a steeper slope for $t' = 0$ than that for $t'/t = -0.1$ at the Fermi level. This confirms that negative t' leads to a *wider* range of fillings with a van Hove peak near the Fermi level. The fact that this range of fillings coincides with the region where marginal Fermi liquid behavior is seen in the self energy suggests that the van Hove singularity and quantum criticality are related.

Another interesting point to be noted here is that, when compared to the $t' = 0$ result, the quasi-particle peaks become more incoherent for negative t' . This can be seen in the Matsubara quasiparticle weight along the antinodal momentum direction, Z_{AN} [61] displayed in Fig. 3.13 as a function of temperature for different fillings. The quasiparticle fraction is consistently smaller for $t'/t = -0.1$ than for $t' = 0$ for all fillings. This can also be seen through the increase of the blue color in the dispersion curves in Fig. 3.11 when compared with Fig. 3.6.

3.3.4 Transport Properties

Matrix element effects[130, 131], and the low precision of inverse photoemission can complicate the direct measurement of the flat dispersion resulting in the van Hove singularity, making indirect probes like the Fermi surface topology[129] and transport measurements more important. The van Hove singularity and the quantum critical point will also impact the transport properties of the system. Using the Kubo formula under the relaxation time approximation in Eqs. (3.8) and (3.9), we obtain the resistivity, thermal conductivity, and thermopower in the Fermi liquid, marginal Fermi liquid, and pseudo-gap regions.

Fig. 3.14 shows the resistivity as a function of temperature for $t' = 0$, left panel, and $t'/t = -0.1$, right panel. Linear resistivity reveals evidence of the marginal Fermi liquid because the electronic cross section is proportional to $-\Sigma''(k_F, \omega = 0)$ at low T , and, as

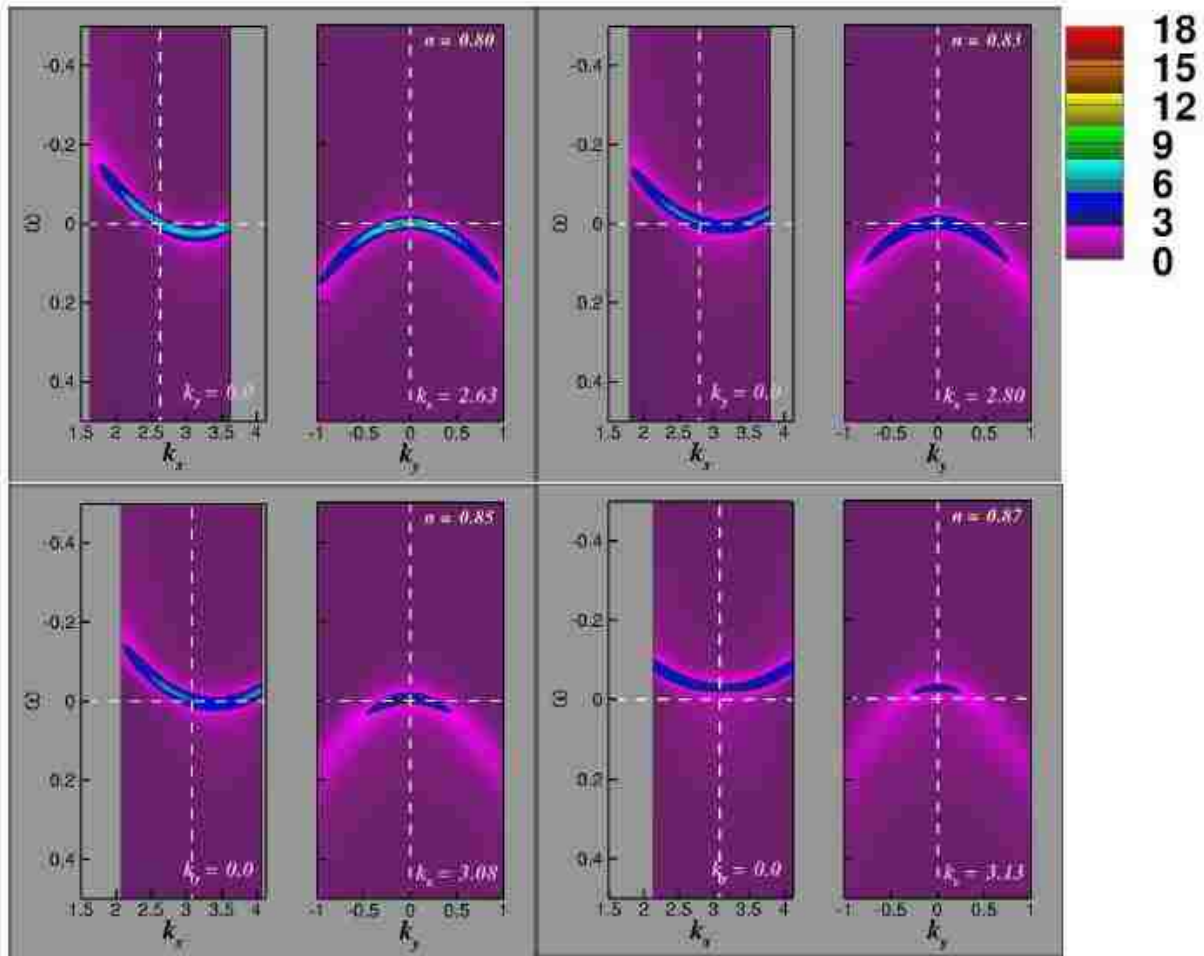


Figure 3.11: (Color online) Energy dispersion obtained from the peaks of the spectral function $A(\mathbf{k}, \omega)$ for various fillings around the Fermi vector \mathbf{k}_F along the anti-nodal direction for $t'/t = -0.1$, $U = 6t$, $4t = 1$, $N_c = 16$ and $\beta = 48$. The dispersion along the k_y direction remains pinned near the Fermi level for a broader range of dopings than found when $t' = 0$. Again, the dispersion along the k_x direction moves continuously across the Fermi level.

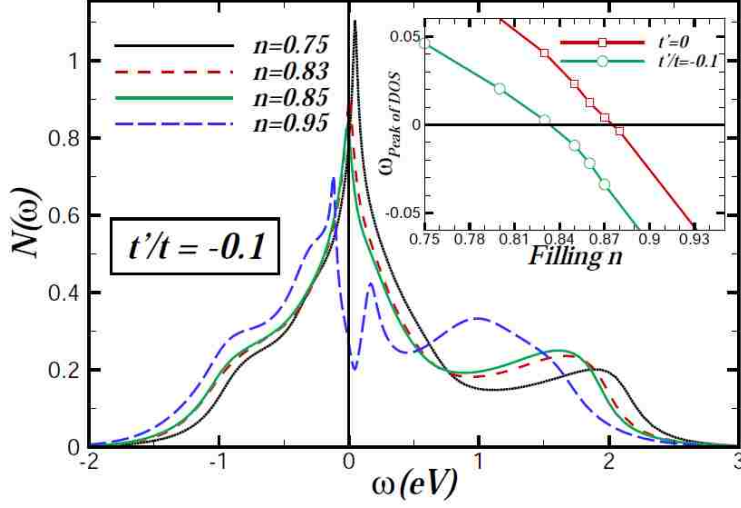


Figure 3.12: (Color online) Single-particle density of states for $t'/t = -0.1$ when $U = 6t$, $N_c = 16$, $4t = 1$, and $\beta = 48$. Inset: Comparison of the filling dependence of the position of the peak of the density of states (ω_p) for $t' = 0$ and $t'/t = -0.1$. As the filling changes, ω_p for $t' = 0$ crosses the Fermi level more quickly than for $t'/t = -0.1$.

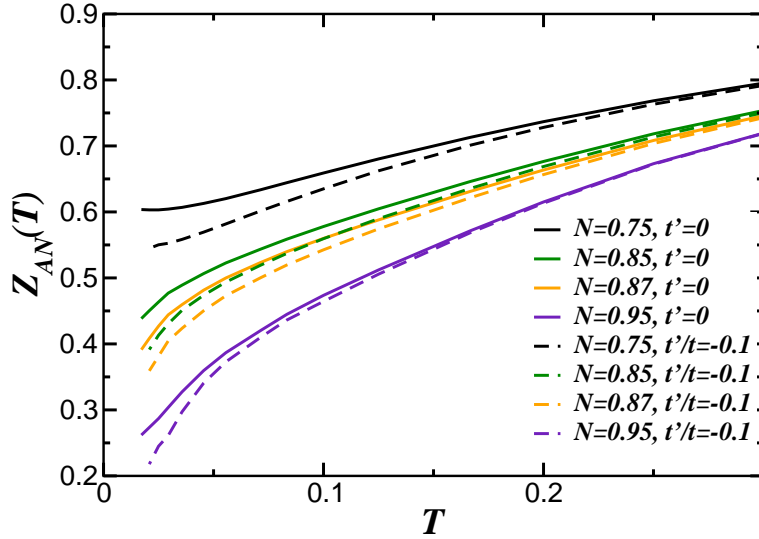


Figure 3.13: (Color online) Temperature dependence of the Matsubara fraction along the anti-nodal direction, Z_{AN} , for various fillings for $t' = 0$ and $t'/t = -0.1$. At the same filling and temperature, the Matsubara fraction decreases when $t' < 0$.

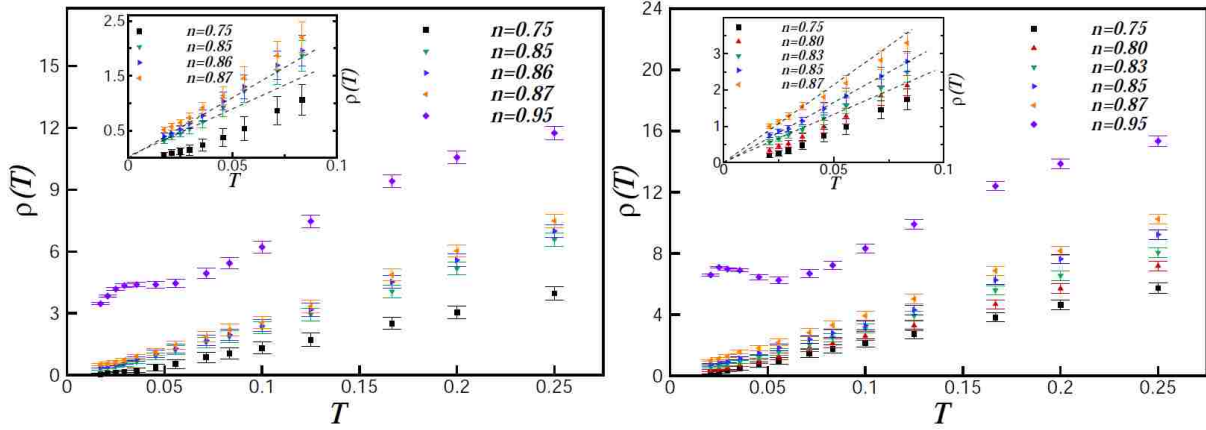


Figure 3.14: (Color online) Resistivity versus temperature for $t' = 0$ (left) and $t'/t = -0.1$ (right) with $U = 6t$, $N_c = 16$, and $4t = 1$. The dashed lines in the insets are linear fits. For $t' = 0$, the resistivity shows linear- T behavior for $n = 0.85$ and $n = 0.86$. For $t'/t = -0.1$, the resistivity shows linear- T behavior from $n = 0.83$ to $n = 0.87$.

seen in Fig. 3.4 and 3.10, this self energy is linear in T . Again, for $t' = 0$ a narrow range of fillings, from $n = 0.85$ to 0.86 , displays a linear- T resistivity at low T . While for $t'/t = -0.1$ a larger range of filling, $n = 0.83$ to 0.87 , exhibits a linear temperature dependence. The linear resistivity in the marginal Fermi liquid region is consistent with experiments[106, 107, 108, 109]. For $n = 0.75$, both $t' = 0$ and $t'/t = -0.1$ show Fermi liquid character, with a resistivity which goes to zero quadratically when T approaches zero. The fact that doping region with marginal Fermi liquid character increases with negative t' has consequences for the phase diagram near the quantum critical point, which we will discuss in Section 3.4.

According to the Wiedemann-Franz Law, $\kappa/(\sigma T) = \pi^2/3$ ($k_B = e = 1$), the thermal conductivity of a Fermi liquid is inversely proportional to T [117]. Fig. 3.15 shows that $\kappa \propto 1/T$ for $n = 0.75$ when $t'/t = 0$ and -0.1 , but weakly depends on T for the marginal Fermi liquid and the pseudo-gap regions. The inset shows that, for $n = 0.75$, the Wiedemann-Franz ratio $\kappa/(\sigma T)$ approaches a constant which is less than $\pi^2/3$ when $T \leq 0.08$. Dahm et al.[132] investigated the two-dimensional Hubbard model for $n \simeq 0.9$ and also found a smaller Wiedemann-Franz ratio. However, we find that the Wiedemann-Franz ratio is larger than $\pi^2/3$ for the marginal Fermi liquid ($n = 0.85$) and pseudo-gap ($n = 0.95$) regions. We also see that the thermal conductivity becomes very small as $T \rightarrow 0$ for $n = 0.95$ and saturates to a constant for $n = 0.85$. So, when studying κ , the marginal Fermi liquid seems to separate the Fermi liquid from the pseudo-gap region. The dashed curves in Fig. 3.15 for $t'/t = -0.1$ data are always below the solid curves for $t' = 0$ when plotting κ . However, the $t'/t = -0.1$ data is above the $t' = 0$ results when we focus on the ratio $\kappa/\sigma T$. This implies that negative t' reduces the electrical conductivity more than the thermal conductivity.

Chakraborty et al.[104] argue that the thermopower changes sign near the quantum critical point, and that this is related with the development of a state with particle-hole

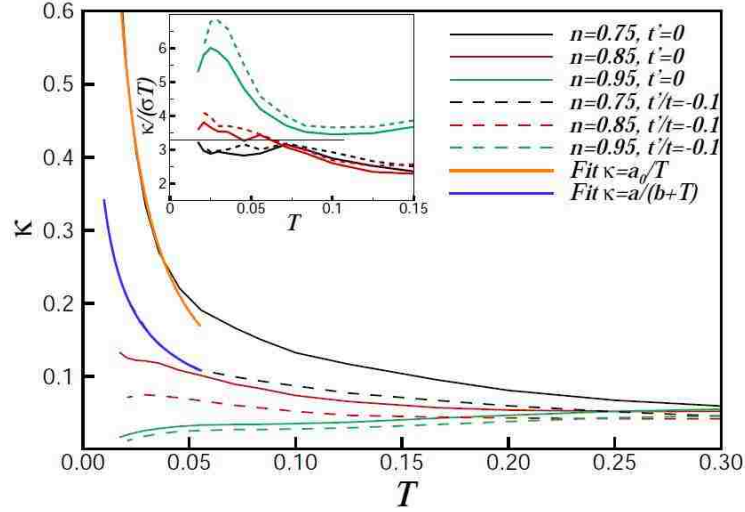


Figure 3.15: (Color online) Thermal conductivity versus temperature for $U = 6t$, $N_c = 16$, and $4t = 1$. Inset: Wiedemann Franz ratio for the same physical parameters. The horizontal solid line labels the constant $\pi^2/3$.

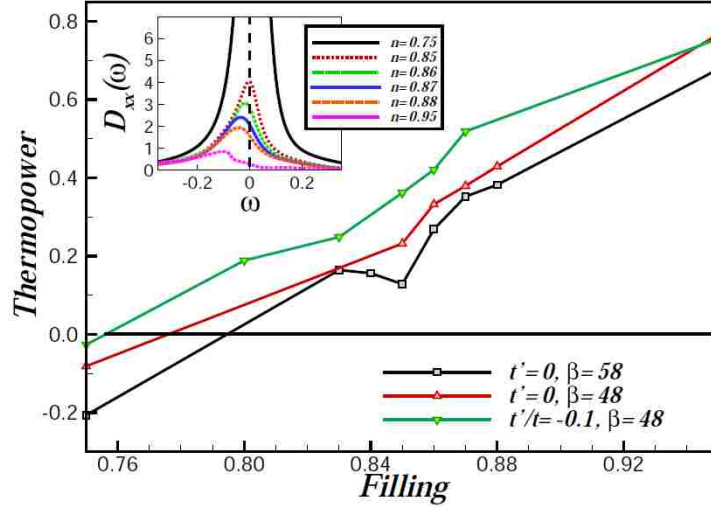


Figure 3.16: (Color online) Thermopower as a function of filling for $U = 6t$, $N_c = 16$, $4t = 1$. Lines are guides to the eyes. Inset: Frequency dependence of $\mathcal{D}_{xx}(\omega)$ (c.f. Eq. (3.9) for different fillings when $t' = 0$, $\beta = 58$. The slope of $\mathcal{D}_{xx}(\omega)$ at $\omega = 0$ is proportional to the thermopower according to Eq. (3.10).

symmetry. Fig. 3.16 shows the thermopower S as a function of filling. For $t' = 0$ and $\beta = 58$, the filling at which S changes sign is roughly 0.80. We expect that the zero-crossing of the thermopower will approach the critical filling of 0.85 for decreasing T . However, this is different from the filling, $n = 0.88$, at which the density of states displays particle-hole symmetry.

We find that due to the k -dependence of the relaxation time and the electron group velocity, the filling at which the thermopower crosses zero does not occur at the filling where the density of states shows a particle-hole symmetry at low energies. In Fermi liquid theory[125], if we assume constant relaxation time and group velocity, the thermopower is proportional to the derivative of the logarithm of the density of states at the Fermi level. This would suggest a thermopower which changes sign as the van Hove singularity crosses the Fermi level. However, in this approach $A(\mathbf{k}, \omega)^2$ in Eq. (3.9) is approximated by $\delta(\omega - \epsilon_{\mathbf{k}})\tau$, where $\tau = \tau_{\mathbf{k}}$ is a \mathbf{k} -independent relaxation time. In addition, the electron group velocity we use in our calculation also has a \mathbf{k} -dependence:

$$v^x(\mathbf{k}) = \frac{\partial \epsilon_{\mathbf{k}}^0}{\partial \mathbf{k}_x} = 2t \sin k_x + 4t' \sin k_x \cos k_y. \quad (3.13)$$

If we compare the quantity $\mathcal{D}_{xx}(\omega)$ (the inset of Fig. 3.16) and the density of states (Fig. 3.5) for different fillings and the same $t' = 0$, we find that the effect of $v^x(\mathbf{k})^2$ is to pull the peak of the density of states to the left, because the $\sin k_x$ term suppresses the contribution of the van Hove singularity at $X(\pi, 0)$ and enhances the contribution from the states below the Fermi level. As a result, the thermopower changes sign continuously and at a filling where the quantity $\mathcal{D}(\omega)$ has a zero slope at the Fermi level, around $n = 0.85$. As noted by Chakraborty et al.[104], this filling is different from the one where the density of states displays particle-hole symmetry, $n = 0.88$ for $t' = 0$. The impact of the van Hove singularity on the thermopower and other transport coefficients is diminished by the fact that the van Hove singularity comes predominantly from a region in \mathbf{k} space where the group velocity goes through zero.

3.4 Discussion

The results presented here have implications for both the quantum critical phase diagram and the proximity of the superconducting dome to the quantum critical point.

The close proximity of the quantum critical filling and the filling where the van Hove singularity crosses the Fermi level suggests that the two are related or even concomitant. Near the quantum critical point, we find that the flat part of the dispersion orthogonal to the antinodal direction is pinned to the Fermi level, but not the dispersion along that direction (Fig. 3.6). We also find that the low energy density of states exhibits particle-hole symmetry (Fig. 3.5). The linear- T resistivity and self energy, characteristic of a marginal Fermi liquid, are observed for the same fillings where this pinning is observed. Within the Dynamical Mean Field Approximation (DMFA)[78], it is known that if the van Hove singularity is pinned to the Fermi level for the non-interacting case, it remains pinned even for the interacting case due to the momentum independent nature of the self-energy. In addition, a van Hove singularity initially away from the Fermi level will tend to move towards the Fermi level due to the

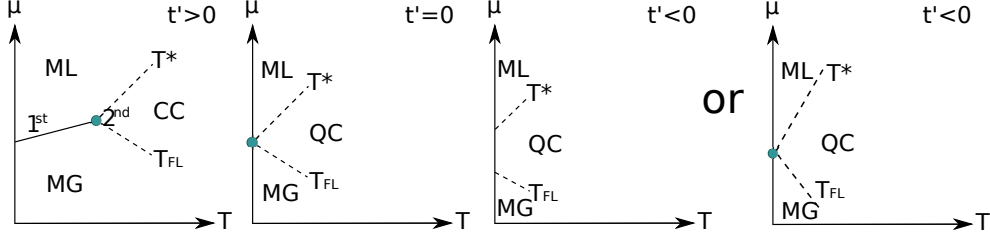


Figure 3.17: Schematic chemical potential-temperature ($\mu-T$) phase diagram for three values of t' : (from left to right) $t' > 0$, $t' = 0$, $t' < 0$ scenario presented in this chapter and a $t' < 0$ scenario based on a Lifshitz transition. CC (QC) indicates the classical (quantum) critical region. ML (MG) indicates the Mott liquid (gas) region. T^* is the crossover temperature between the Mott liquid and the critical region, T_{FL} separates the Mott gas from the critical region. Note here, we have ignored other phases to focus attention on the quantum critical region.

narrowing of the coherent component of the band resulting from electronic correlations. In the simplest Fermi liquid picture, the coherent part of the single-particle Green function $G(\mathbf{k}, \omega) = Z(\mathbf{k})/(\omega + i0^+ - Z(\mathbf{k})\epsilon(\mathbf{k}))$. So, if $Z(\mathbf{k})$, becomes small for some values of \mathbf{k} , then we would expect to see a flattening of the observed quasiparticle dispersion, $Z(\mathbf{k})\epsilon(\mathbf{k})$, accompanied by a shift of the peak towards the Fermi level with a vanishing weight. The new result of our work is that the non-local correlations included in the DCA, but absent in the DMFA, are able to move the van Hove singularity, with finite weight, to and even across the Fermi level. This cannot be due solely to the narrowing of the coherent part of the band, since the van Hove singularity crosses the Fermi level where quasiparticle fraction Z is already zero.

Neither a non-interacting picture of the van Hove singularity can completely describe the superconducting transition in the vicinity of the critical filling. In a BCS superconductor, the transition is driven by a logarithmic divergence of the bare pairing bubble as the temperature falls. In a recent work[62], the bare d -wave pairing susceptibility χ'_{0d} of the 2D Hubbard model was found to diverge algebraically as $\frac{1}{\sqrt{T}}$ at the quantum critical filling, instead of logarithmically, giving rise to a higher T_c . In the simulation, we traced the origin of this algebraic behavior to a component of the dynamic bare bubble which scaled as $\chi''_{0d}(\omega)/\omega = T^{-3/2}H(\omega/T)$ (see Fig. 3.1). A van Hove singularity is known to enhance the divergence of the bare pairing bubble. Since the bare d -wave pairing susceptibility is dressed only by the self energy, with no vertex corrections, a van Hove singularity seems to be the most likely explanation of its enhanced divergence. However, we found that a simple non-interacting picture with a van Hove singularity at the Fermi level does not completely explain the observed phenomena. The standard quadratic dispersion gives a logarithmic divergence of χ'_{0d} for the half filled model. A hypothetical quartic dispersion yields the observed algebraic divergence for χ'_{0d} , but does not give the correct scaling for the imaginary part of the bare susceptibility found in Yang et al.[62]. The latter is a consequence of the proximity to a quantum critical point, but not necessarily part of the van Hove scenario.

Our results also shed additional light on the quantum critical phase diagram. We found

previously[133, 134] that when $t' > 0$, there is a first order phase separation transition with a first-order line of co-existence in the $\mu - T$ phase diagram as shown in Fig. 3.17. In analogy with liquid-gas mixtures, we identify the two phases as a Mott liquid, which is insulating and incompressible with well formed local moments and short ranged order, and a Mott gas, which is a weakly compressible metallic Fermi liquid. The two phases have the same symmetry, so the first order line of co-existence terminates at a second order point where the charge susceptibility diverges. In analogy to other liquid-gas mixtures, there is a fan-shaped region dominated by fluctuations for temperatures above the critical point with neither liquid nor gas character. When $t' \rightarrow 0$, the critical point goes continuously to zero temperature and thus becomes a quantum critical point[134]. Above the quantum critical point, the marginal Fermi liquid region is found to exist in the V-shape quantum critical region. Inside this region, the only scale is the temperature (like Eq. (3.6) and (3.7)). T^* is the temperature separating the marginal Fermi liquid from the pseudo-gap region. T^* does not separate the quantum critical region from a region of hidden order. Rather in our scenario, it is only the boundary of the quantum critical region. As we cross from the quantum critical region to the Mott liquid, the character of the Mott liquid becomes apparent including a pseudo-gap.

Here we consider the effect of a negative next-nearest-neighbor hopping t' on the single particle dispersion. We find that for $t'/t = -0.1$, the flat part of the dispersion orthogonal to the antinode remains in close proximity to the Fermi level for a larger range of fillings ($0.83 \leq n \leq 0.87$) when compared with the $t' = 0$ result. We find that the resistivity displays a linear- T dependence, and the self energy displays MFL characteristics in the same range of doping. We also note that the single-particle spectra is less coherent in the center of this doping region than it is at the quantum critical filling when $t' = 0$. These observations are consistent with an increase in the doping region of marginal Fermi liquid character when $t'/t < 0$.

There are several different scenarios which may explain this behavior. Since the doping region where the van Hove singularity is near the Fermi level increases with decreasing t'/t , perhaps the simplest understanding of this behavior is that the van Hove singularity *pinning* gives rise to the marginal Fermi liquid behavior[74, 75, 76]. Another possibility is that both T and negative t' are relevant variables, or variables that, when finite, move the system away from a critical point. In addition, they are roughly similar in their effect, in that when $t' = T = 0$ the doping region of marginal Fermi liquid character shrinks to a point, but the region increases with either increasing T or decreasing t' . Thus when $t' < 0$, the quantum critical point may be viewed as moving to negative temperatures so that the quantum critical region broadens to allow the linear- T resistivity and the pinning of the flat k_y dispersion to the Fermi level to exist for a wider range of fillings (compare e.g. the third panel of Fig. 3.17 and inset of Fig. 3.1). However, this interpretation is not consistent with scaling theory where we expect a finite low temperature scale like T_F or T^* to emerge for any set of parameters that take us away from the quantum critical point. Another possibility is that the change in Fermi surface topology associated with the van Hove singularity crossing the Fermi level can introduce *Lifshitz* singularities in the free energy[135, 136, 137, 138, 139, 140, 141]. This scenario will mean a line of zero temperature critical points in the $t' - \mu$ plane beyond the quantum critical point as the control parameter t' is decreased from zero to negative values

in the $t' - \mu$ plane. For positive t' the Lifshitz transition may yield a line of first order critical points in $t' - \mu$ plane which terminates at the quantum critical point for $t' = 0$. To understand our results, the line of Lifshitz transitions for negative values of t'/t must yield an associated V-shaped region of quantum criticality which becomes flatter as t' decreases as shown on the right in Fig. 3.17. Finally, another mechanism enhanced by the van Hove singularity is the *Pomeranchuk instability*[142, 143] of the Fermi surface where the Fermi surface is distorted to break the C_4 symmetry of the square lattice. The possibility of Lifshitz and Pomeranchuk transitions are being studied currently and will be published elsewhere.

There is some experimental evidence[129] in the cuprates that there is a change in Fermi surface topology and an associated Fermi level crossing of the van Hove singularity at a doping that is larger than the doping at which T_c is maximum, while still being within the dome. On the other hand, we find that the van Hove singularity crosses the Fermi level at a slightly smaller doping than the optimal doping. This disagreement can be due to the other effects present in the real systems e.g. phonons that are not incorporated in this model calculation, or the strong doping dependence of the strength of the pairing interaction[62] seen in the simulations.

The transport provides some additional evidence for the van Hove singularity. In our calculations, the low energy particle-hole symmetry and the change in sign of the thermopower with doping near the critical value are both due to the crossing of the van Hove singularity. However, the doping associated with the van Hove crossing differs from that where the thermopower is zero due to the anisotropy of the group velocity on the Fermi surface.

3.5 Conclusion

We explore the role of the van Hove singularity in the quantum criticality observed at finite doping in the Hubbard model[61]. Near the quantum critical filling, we find a van Hove singularity due to a flattening of the dispersion near the Fermi level. The motion of the flat part of the dispersion along the antinodal direction is anisotropic. The part along the antinode moves continuously through the Fermi level. The part orthogonal to this direction is pinned near the Fermi level at a filling where the self energy, transport, and energies[128] also display marginal Fermi liquid behavior, and the quasiparticle fraction vanishes[61]. Many authors have proposed that the van Hove singularity near the Fermi level will enhance superconductivity by enhancing the divergence of the bare pairing bubble. Indeed we found previously that the superconducting dome surrounds the critical doping where the real part of the pairing bubble diverges algebraically, replacing the Fermi liquid log divergence[62]. However, a simple non-interacting picture with the van Hove singularity at the Fermi level doesn't explain the quantum critical scaling of the bare dynamic pairing susceptibility. We also found previously that a positive t' is the control parameter for a first order phase separation transition which is terminated by a second order critical point. As $t' \rightarrow 0$ this second order terminus is driven to zero temperature yielding the quantum critical point[134]. Here we explore the effect of a negative t' , and find that it is a relevant variable which increases the extent in doping (and chemical potential) of the quantum critical region characterized by marginal Fermi liquid behavior.

Chapter 4

Lifshitz Transition in the two-dimension Hubbard Model

Using large-scale dynamical cluster quantum Monte Carlo simulations, we study the Lifshitz transition of the two dimensional Hubbard model with next-nearest-neighbor hopping (t'), chemical potential and temperature as control parameters. At $t' \leq 0$, we identify a line of Lifshitz transition points associated with a change of the Fermi surface topology at zero temperature. In the overdoped region, the Fermi surface is complete and electron-like; across the Lifshitz transition, the Fermi surface becomes hole-like and develops a pseudogap. At (or very close to) the Lifshitz transition points, a van Hove singularity in the density of states crosses the Fermi level. The van Hove singularity occurs at finite doping due to correlation effects, and becomes more singular when t' becomes more negative. The resulting temperature dependence on the bare d -wave pairing susceptibility close to the Lifshitz points is significantly different from that found in the traditional van Hove scenarios. Such unambiguous numerical observation of the Lifshitz transition at $t' \leq 0$ extends our understanding of the quantum critical region in the phase diagram, and shines lights on future investigations of the nature of the quantum critical point in the two dimensional Hubbard model.

This work is the following work of the last chapter[23]. I performed analytic continuation on self energies intensively using the Maximum Entropy Method (MEM) to obtained the zero-frequency spectra $A(\mathbf{k}, \omega = 0)$ around the quantum critical point and identify the Lifshitz physics. This chapter has been published in the journal of Phys. Rev. B, **86**, 165136 (2012)[24].

4.1 Introduction

The physical properties of high- T_c cuprate superconductors are extremely sensitive to doping. Experiments, such as the angle-resolved photoemission spectroscopy[144] (ARPES) and quantum oscillation measurements[145], have clearly demonstrated a Fermi surface reconstruction as the doping concentration is varied. In the overdoped region, ARPES and quantum oscillation studies revealed a large Fermi surface that can be well captured by band theory. On the other hand, once the doping is reduced, the shape and size of Fermi surface change and photoemission data indicate that the Fermi surface breaks up into "Fermi arcs"[146]. More recent studies further indicate that the "Fermi arcs" are actually part of closed hole pockets[147, 148]. The formation of small Fermi pockets, as the doping is reduced from overdoped to underdoped region, has also been substantiated by quantum oscillation measurements[149, 150].

From a theoretical point of view, the change of the Fermi surface topology from a large surface to small "arcs" or "pockets" resembles a Lifshitz transition. Although proposed by Lifshitz in noninteracting Fermion systems decades ago[151], the Lifshitz transition has only recently begun to be considered as a quantum phase transition in strongly correlated electron

systems[137, 138, 139, 140, 152, 153, 154]. It has been used to explain experimental data in high- T_c cuprate superconductors[155, 141] or heavy fermion systems[156].

Using large-scale dynamical cluster quantum Monte Carlo simulations[47], a series of recent numerical works[157, 134, 62, 158, 23, 61] mapped out the phase diagram of the two dimensional Hubbard model near the quantum critical filling. Particularly, the superconducting dome in the proximity to the quantum critical doping has been identified[62]. At positive t' , there is a first-order phase separation transition occurring at finite temperature. The two phases being separated are an incompressible Mott liquid and a compressible Mott gas; these two phases are adiabatically connected to the pseudogap and the Fermi liquid states at $t' = 0$. The first-order line of coexistence terminates at a second order point where the charge susceptibility diverges[134, 158]. As $t' \rightarrow 0$, this critical point extrapolates continuously to zero temperature and thus becomes the quantum critical point (QCP) underneath the superconducting dome. Above the QCP, a V-shaped quantum critical region, characterized as a marginal Fermi liquid[159, 160] with linear resistivity, separates the pseudogap and the Fermi liquid phases. Furthermore, when the next-nearest-neighbor hopping becomes negative, $t' < 0$, there is indication of the Fermi surface topology changes at zero temperature, and the filling at which such changes occurs is an extension of the QCP at $t' = 0$ to negative t' [23].

Other numerical works also found similar feature of the Fermi surface reconstruction at $t' \leq 0$ by varying the hole doping concentration from overdoped towards half-filling. These include results from both dynamical cluster approximation[161, 162, 163, 164] and the cellular dynamical mean-field theory[165, 166, 167, 168, 169, 170], although the finite temperature critical point in the hole-doped side of the phase diagram found in Ref [[167]] is inconsistent with other works and might suffer from the finite size effects of a small four-site cluster.

Following such evidence, and in light of viewing the Fermi surface reconstruction as a Lifshitz transition[137, 138, 139, 155, 141, 153], we performed systematic numerical studies on the quantum critical phase diagram of the two dimensional Hubbard model at various t' , with special attention to the region of $t' < 0$, which is relevant for the hole-doped cuprates. We find at $t'/t \leq 0$, as the doping concentration varies from the overdoped to the underdoped regime, the Fermi surface changes its topology from electron-like with complete Fermi surface to hole-like with pseudogap at the anti-nodal direction. Such a topological transition in the Fermi surface is a Lifshitz transition. It is furthermore concomitant with a van Hove singularity in the density of states crossing the Fermi level at a doping which occurs very close to (if not at) the quantum critical point.

The van Hove singularity crossing and the concomitant quantum critical point occur at finite doping due to correlation effects even when $t' = 0$. Interestingly, we find the quantum critical phenomena prevail for negative t' , and the van Hove singularity defines a line of quantum critical points which extends from the QCP at $t' = 0$ to higher doping for $t' < 0$. The temperature dependence of correlation effects close to the van Hove singularities, and its influence on quantities like the quasiparticle fraction and the pairing polarization are very different from those found in the traditional van Hove scenarios[171, 66]. The QCP and the van Hove singularity have great impact on the conditions for pairing. At $t' < 0$, we find an enhanced temperature dependence of the bare d -wave pairing susceptibility above the QCP

that cannot be captured by the conventional BCS logarithmic divergence or the log-squared divergence found at a static van Hove singularity[171].

This chapter is organized as follows. Section 4.2 outlines the model and the methods used in this study: the dynamic cluster approximation (DCA) with weak-coupling continuous-time quantum Monte Carlo (CTQMC) as its cluster solver. Section 4.3 and 4.4 contain our numerical results and discussion, beginning with the spectral function and dispersion at various doping concentrations and values of t'/t , and followed by a detailed account of other single-particle properties such as density of states and quasiparticle fraction, across the Lifshitz transition. We then provide results on the unique temperature dependence of the bare d -wave pairing susceptibility. We use a schematic quantum critical phase diagram of the model which summarizes our numerical results. We end with conclusions and an overview of open questions in Section 4.5.

4.2 Formalism

In this work, we look for direct evidence of a Lifshitz transition in the spectral function of the two-dimensional Hubbard model defined in the eq. (2.23) with bare dispersion given by eq. (2.3).

We employ the DCA[119, 45] with weak-coupling CTQMC[49] as a cluster solver. The DCA is a cluster mean-field theory that maps the original lattice onto a periodic cluster of size $N_c = L_c^D$ (D is the dimensionality) embedded in a self-consistently determined host. It treats the spatial short-ranged correlations (up to L_c inside a cluster) explicitly while approximating the long-ranged correlations with a mean-field. In this work we choose a square cluster with $N_c = 16$. The six independent momentum patches are centered at $\Gamma = (0, 0)$, $M = (\pi, \pi)$, $X = (\pi, 0)$, $(\pi/2, \pi/2)$, $(\pi, \pi/2)$, and $(\pi/2, 0)$. We set the energy scale to $4t = 1$, choose the interaction strength at $U = 6t$ and study inverse temperatures up to $\beta = 58/4t$. The temporal correlations, essential for quantum criticality, are treated explicitly by the weak-coupling CTQMC solver for all cluster sizes. The solver expands the Coulomb interaction diagrammatically and samples in time continuously. Different from the Hirsch-Fye algorithm[121, 122] it therefore has no Trotter error.

As explained in the section 2.4, here we summarize the method of analytic continuing self energies using maximum entropy method. We obtain high-quality estimates of the cluster self-energy $\Sigma(\mathbf{K}, \omega)$ by employing the maximum entropy analytical continuation[57] (MEM) directly to the Matsubara-frequency self energies calculated from the DCA-CTQMC[118, 23, 59]. To perform MEM on the self-energy the non-Hartree part of $\Sigma(\mathbf{K}, i\omega_n)$ must be normalized by $U^2\chi_{\sigma,\sigma}$, where $\chi_{\sigma,\sigma} = \langle n_\sigma n_\sigma \rangle - \langle n_\sigma \rangle^2 = n_\sigma(1 - n_\sigma)$ is the local polarization of a single spin species σ . The normalized spectrum of the self-energy acts as a probability distribution:

$$\frac{\Sigma(\mathbf{K}, i\omega_n) - \Sigma_H}{U^2\chi_{\sigma,\sigma}} = \int d\omega \frac{\sigma(\mathbf{K}, \omega)}{i\omega_n - \omega}, \quad (4.1)$$

where $\sigma(\mathbf{K}, \omega) = -\frac{1}{\pi}\Sigma''(\mathbf{K}, \omega)/U^2\chi_{\sigma,\sigma}$, $\int d\omega\sigma(\mathbf{K}, \omega) = 1$, using $\chi_{\sigma,\sigma}$ obtained from the Monte Carlo process.

To obtain the lattice self energy, $\Sigma(\mathbf{k}, \omega)$, we interpolate the cluster self energy, $\Sigma(\mathbf{K}, \omega)$. From the lattice self energy we can get the lattice single-particle spectral function, $A(\mathbf{k}, \omega)$. An alternative way has been suggested by Stanescu et al.[172, 166, 169, 170], where the cluster cumulant, $M(\mathbf{K}, \omega) = 1/(\omega + \mu - \Sigma(\mathbf{K}, \omega))$, has been used for the interpolation to lattice quantities. Although the spectral functions produced by the two interpolation schemes have differences in the underdoped region, we found the two methods give the same quantum critical filling n_c [173].

4.3 Results

Figure 4.1 shows the \mathbf{k} -resolved spectral function evaluated at the Fermi level, $A(\mathbf{k}, \omega = 0)$, for $t'/t = 0$ and $t'/t = -0.1$. At $t' = 0$ we observe a change of the Fermi surface topology from electron-like to hole-like as the filling increases from $n = 0.75$ towards half-filling. This change of the topology of the Fermi surface or Lifshitz transition occurs at the same filling where the van Hove singularity crosses the Fermi level[66, 174]. The corresponding filling is the critical filling, n_c , of the Lifshitz transition. In the case $t' = 0$ we obtain $n_c \approx 0.88$. At $t'/t = -0.1$ the Fermi surface changes from electron-like to hole-like and then disappears as n varies from 0.8 towards half filling. Following the same criterion, the Lifshitz transition occurs at $n_c \approx 0.835$. Finally, for $t'/t = -0.2$, we find $n_c \approx 0.77$ (not shown). For all $t'/t \leq 0$ we studied, the system enters the pseudogap phase once the filling is larger than the corresponding n_c . In the case of $n = 0.92$ (left panel of Fig. 4.1) and $n = 0.87$ (right panel of Fig. 4.1) the collapses of the single-particle spectral weight along the antinodal direction can be clearly seen.

Figure 4.2 shows density of states for $t'/t = 0$ (left panel) and $t'/t = -0.1$ (right panel) with the same set of fillings of those in Fig. 4.1. For $t' = 0$, the van Hove singularity shifts from positive to negative frequency as the filling increases from 0.75 towards 1.0. The van Hove singularity is located at the Fermi level for the quantum critical filling $n_c \approx 0.88$. These results are consistent with our previous observations[134, 23]. After passing through the critical filling, a pseudogap in the density of states is formed, as it is displayed by the valley at $\omega \approx 0.05$ for $n = 0.92$, $t'/t = 0$. This parameter regime can thus be identified as the pseudogap region in the phase diagram. For $t'/t = -0.1$, the results in the right panel of Fig. 4.2 show a quantum critical filling $n_c \approx 0.835$. Note, the van Hove singularity in single-particle density of states has also been observed in the "momentum-selective" metal-insulator transition scenario[161, 162, 163, 164], however, the quantum critical phenomena associated with the van Hove singularity and the Lifshitz transition have not been discussed there.

The van Hove singularity originates from the flat dispersion along the antinodal direction with energy close to the Fermi level[84, 66, 174], as shown in Figure 4.3. At the critical doping for $t'/t = 0.0$, -0.1 , and -0.2 , there is always a saddle point region around momentum $X = (\pi, 0)$ where the dispersion is flat. In addition, we find that the flat region become wider and more pronounced as t' becomes more negative. Such flat dispersion at the chemical potential contributes low energy states and results in the van Hove singularity at the Fermi energy. Hence, our observation of the Lifshitz transition at the quantum critical doping for

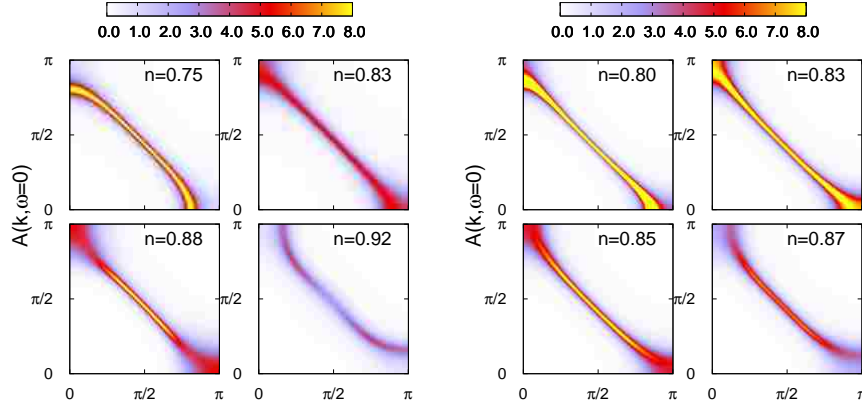


Figure 4.1: (Color online) Zero frequency spectra $A(\mathbf{k}, \omega = 0)$ for $t'/t = 0$ (left) and $t'/t = -0.1$ (right) as a function of filling n . As n increases towards half-filling, the system undergoes a Lifshitz transition where the Fermi surface changes topology from electron-like to hole-like. (Left panel) The Lifshitz transition occurs at $n_c \approx 0.88$, where the van Hove singularity crosses the Fermi level (as shown in Figure 4.2). (Right panel) The Lifshitz transition occurs at $n_c \approx 0.835$. Note that when $t'/t = -0.1$, the Lifshitz transition happens at a smaller filling than for the $t' = 0$ case. In either case, as $n \rightarrow 1$, the system enters the pseudogap phase with vanishing quasiparticle weight.

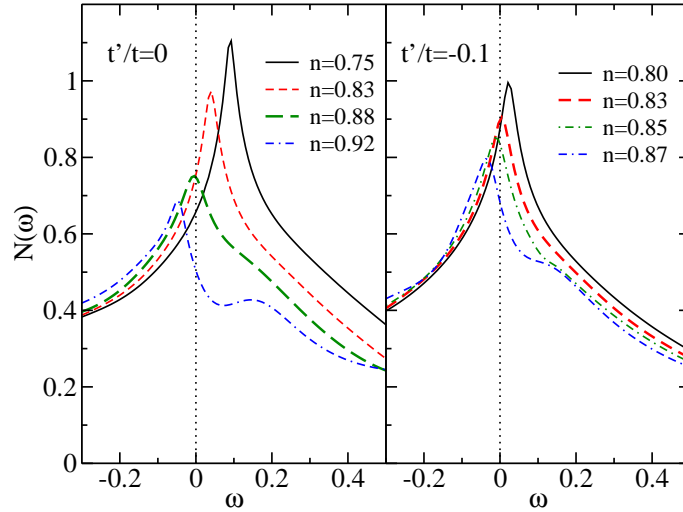


Figure 4.2: (Color online) The single-particle density of states for the parameters shown in Figure 4.1. (Left panel) $t'/t = 0$ with $n = 0.75, 0.83, 0.88$ and 0.92 . (Right panel) $t'/t = -0.1$ with $n = 0.80, 0.83, 0.85$ and 0.87 . The position of the van Hove singularity (peak in the density of states) shifts from positive frequency to negative frequency as the filling moves towards half-filling. The quantum critical point is at $n_c \approx 0.88$ for $t'/t = 0$, and $n_c \approx 0.835$ for $t'/t = -0.1$.

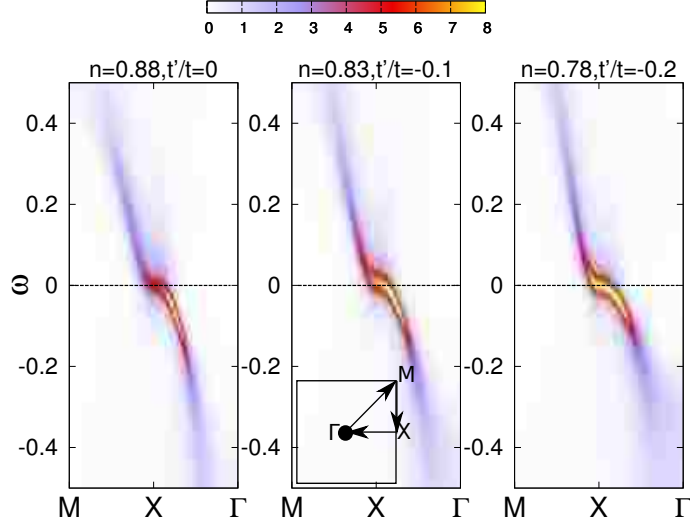


Figure 4.3: (Color online) Intensity plots of the spectral function $A(\mathbf{k}, \omega)$ along the segment $M \rightarrow X \rightarrow \Gamma$ inside the Brillouin zone. For different t'/t near the quantum critical fillings: $t'/t = 0$ with $n = 0.88$ (left), $t'/t = -0.1$ with $n = 0.83$ (middle), and $t'/t = -0.2$ with $n = 0.78$ (right), a saddle point region (flat dispersion) around X crosses the Fermi level at the critical filling n_c . The region becomes wider as t' goes to negative values.

$t'/t \leq 0$ is closely tied (if not in one-to-one correspondence) to the crossing of the Fermi level by the van Hove singularity.

The next-nearest-neighbor hopping t' can be viewed as the control parameter of the Lifshitz transition. To emphasize this point, we also calculate the zero frequency spectra for the non-interacting system as a function of t'/t , and compare them with our DCA results for the interacting system. In Figure 4.4, the left panel demonstrates the effect of t' on the Fermi surface topology of the non-interacting half-filled system. We find the Fermi surface changes from electron-like to hole-like when t' goes from positive to negative values. The right panel of Fig. 4.4 collects our results for the spectra of the interacting system, with $n = 0.85$ fixed and t'/t varies from 0.3 to -0.2 . Similar to the noninteracting system, the Fermi surface topology also changes from electron-like to hole-like as t'/t goes from positive to negative, which confirms that t' is indeed the relevant control parameter of the Lifshitz transition in the interacting system. However, the interacting system follows a more complicated phenomenology than the non-interacting system, due to the effect of electron-electron interaction. For example, in the lower two panels of the right hand side of Fig. 4.4, where t' is negative, not only is the Fermi surface topology changed to hole-like, but the spectral weight along the antinodal direction $(\pi, 0)$ also vanishes, signaling that the system enters the pseudogap phase. The strong interaction results in a redistribution of the spectral weight, leading to features different from the ones of the non-interacting system.

Instead of obtaining the spectral information from the analytical continued data, one can also directly read off the quasiparticle weight $Z(\mathbf{k})$ from the Matsubara frequency results. Since the quasiparticle weight will be finite across a Fermi surface, but it vanishes if the

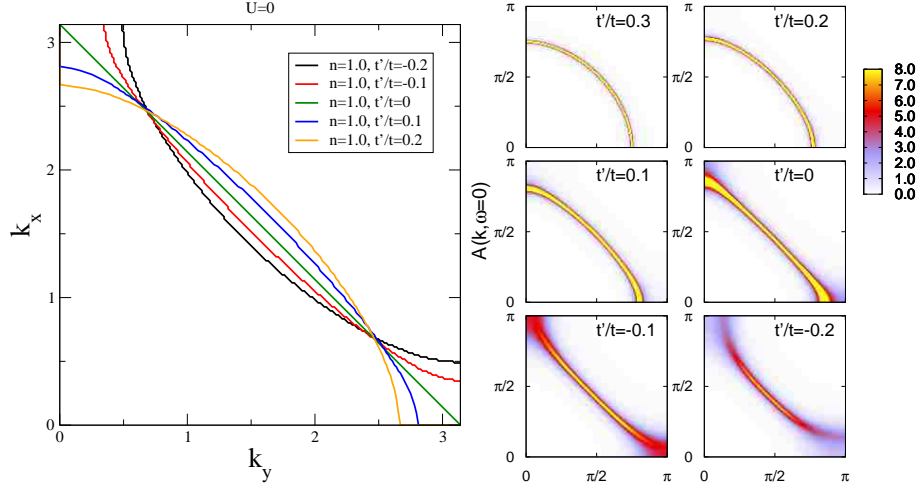


Figure 4.4: (Color online) t'/t as the control parameter of the Lifshitz transition. (Left panel) $A(\mathbf{k}, \omega = 0)$ for the non-interacting system at half-filling. As t'/t goes from positive to negative, the Fermi surface changes from electron-like to hole-like. (Right panel) $A(\mathbf{k}, \omega = 0)$ for the interacting system, $U/t = 6$, with filling $n = 0.85$ fixed. At positive t' , the system is inside the metallic Mott gas phase, and has complete Fermi surface; at negative t' , the system is inside the pseudogap phase, and the Fermi surface becomes hole-like. Since the Coulomb interaction reshuffles the spectral weight, at $t'/t = -0.1, -0.2$, the pseudogap at the antinodal direction can be clearly seen.

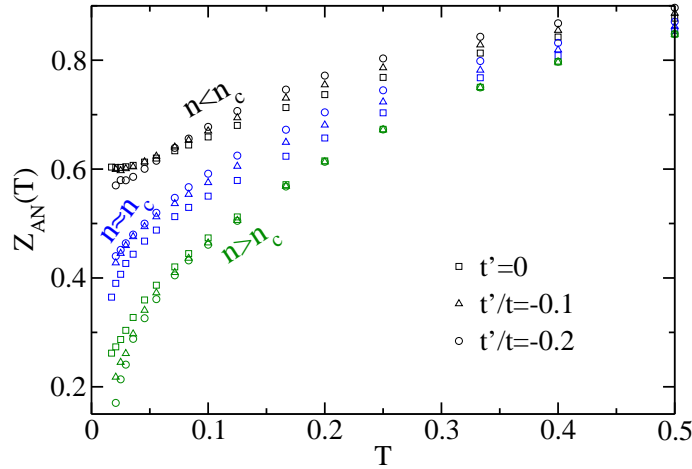


Figure 4.5: (Color online) Matsubara quasiparticle weight $Z_{AN}(T)$ versus temperature T evaluated with \mathbf{k} on the Fermi surface along the antinodal direction, for various fillings and t' . For $n < n_c$, $Z_{AN}(T)$ displays Fermi liquid behavior, with $Z_{AN}(T)$ extrapolating linearly to a finite value at low T ; for $n \approx n_c$, $Z_{AN}(T)$ displays the marginal Fermi liquid behavior, with negative curvature in $Z_{AN}(T)$ at low T ; and once inside the pseudogap region, $n > n_c$, $Z_{AN}(T)$ goes to zero as a function of T faster than for the marginal Fermi liquid fillings.

spectrum is incoherent, $Z(\mathbf{k})$ can be used to distinguish a Fermi liquid and a pseudogap state. The quasiparticle weight is calculated from the Matsubara frequency self-energy as $Z_0(k_F) = \left(1 - \frac{\Sigma''(\mathbf{k}, i\omega_0)}{\omega_0}\right)^{-1} \Big|_{\mathbf{k}=\mathbf{k}_F}$, where $\omega_0 = \pi T$ is the lowest fermionic Matsubara frequency. In the limit $T \rightarrow 0$, $Z_0(\mathbf{k})$ converges to the quasiparticle weight, $Z(\mathbf{k})$. Figure 4.5 shows $Z_{AN}(T) = Z_0(\omega_0 = \pi T, \mathbf{k}_F)$, the Matsubara quasiparticle weight on the Fermi surface along the antinodal direction for various t'/t . Z_{AN} exhibits different behavior for $n < n_c$ where the quasiparticle weight approaches a finite value and for $n \geq n_c$ where the quasiparticle weight vanishes in the limit $T \rightarrow 0$. The temperature dependence of $Z_{AN}(T)$ furthermore provides information about the relevant energy scales. One sees a clear difference in the temperature dependence of $Z_{AN}(T)$ when the system enters Fermi liquid, marginal Fermi liquid and pseudogap phases. Inside the Fermi liquid phase, $n < n_c$, where we choose $n = 0.75$ for $t'/t = 0$, $n = 0.70$ for $t'/t = -0.1$ and $n = 0.65$ for $t'/t = -0.2$, $Z_{AF}(T)$ extrapolates to a finite value roughly linearly at low T . Close to the Lifshitz transition points, $n \approx n_c$, where we choose $n = 0.88$ for $t'/t = 0$, $n = 0.83$ for $t'/t = -0.1$ and $n = 0.78$ for $t'/t = -0.2$, $Z_{AN}(T)$ shows a behavior consistent with the marginal Fermi liquid picture, i.e., a negative curvature in $Z_{AF}(T)$ at low T [61]. Finally, when the system is inside the pseudogap phase, $n > n_c$, we choose the same filling $n = 0.95$ for $t' = 0, -0.1$ and -0.2 , $Z_{AF}(T)$ goes to zero even faster than it does in the marginal Fermi liquid region. The detailed information about the crossover temperatures T^* and T_X , where the former signifies the crossover between pseudogap and the marginal Fermi liquid and the latter is the crossover temperature between the marginal Fermi liquid and the Fermi liquid, and the quantitative distinction between the marginal Fermi liquid and the pseudogap in terms of temperature and frequency dependence of the self energy and resistivity, have been discussed in detail in our previous publications[61, 158, 23].

The bare d -wave pairing susceptibility is calculated as $\chi_{0d}(\omega) = \sum_k \chi_0(\omega, q = 0) g_d(k)^2 / \sum_k g_d(k)^2$, where $g_d(k) = \cos(k_x) - \cos(k_y)$ is the d -wave form factor. It exhibits significant different features near the QCPs compared with those predicted by static van Hove scenarios[171, 66]. As shown in Fig. 4.6, close to the quantum critical fillings, the real part of the bare pairing susceptibility $\chi'_{0d}(\omega = 0, T)$ diverges quickly with decreasing temperature, following a power-law behavior close to $1/\sqrt{T}$, which is different from the BCS type of logarithmic divergence $\chi'_0(T) \propto N(0) \ln(\omega_D/T)$ with $N(0)$ the single-particle density of states at the Fermi surface and ω_D the phonon cutoff frequency. Such behavior is consistent with our previous results at $t' = 0$ close to the quantum critical filling[62, 23]. More interestingly, such temperature dependence persists for $t' < 0$. As shown in Fig. 4.6, the prefactor, a , in the power-law term becomes larger as t' becomes more negative. It signifies that the divergence becomes stronger at $t' < 0$ and, if the pairing strength does not change, there will be a higher superconducting transition temperature T_c compared with the one for $t' = 0$. Moreover, when we scale the imaginary part of the bare pairing susceptibility as $T^{1.5} \chi''_{0d}(\omega)/\omega$ versus ω/T [175], as shown in Fig. 4.7, we find the curves from different temperatures fall on the same universal scaling function such that $T^{1.5} \chi''_{0d}(\omega)/\omega = H(\omega/T) \approx (\omega/T)^{-1.5}$ for $\omega/T \geq 9 \approx 4t/J$, where $J \approx 0.11$ [176, 61] is the antiferromagnetic exchange energy near half filling. From the Kramers-Krönig relation, the real and imaginary parts of the susceptibility are related via $\chi'_{0d}(T) = \frac{1}{\pi} \int d\omega \chi''_{0d}(\omega)/\omega$, so collapse of the $\chi''_{0d}(\omega)/\omega$ will contribute a

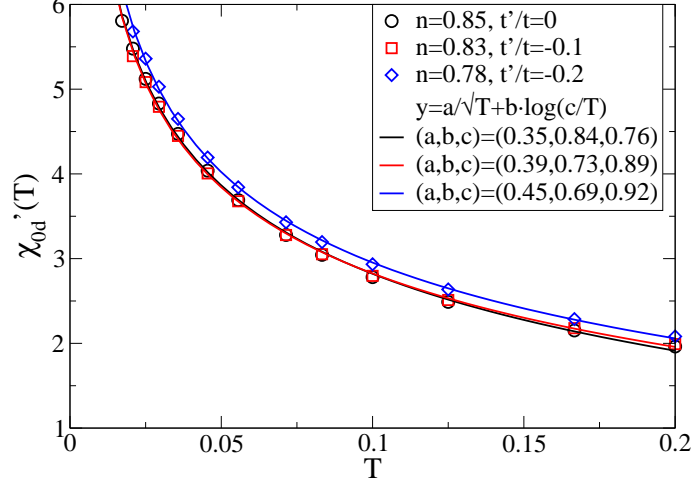


Figure 4.6: (Color online) The real part of the bare d -wave pairing susceptibility, $\chi'_{0d}(\omega = 0, T)$, at zero frequency, close to the quantum critical fillings for $t'/t = 0$, $t'/t = -0.1$, and $t'/t = -0.2$. The solid lines are fits to $\chi'_{0d}(\omega = 0, T) = a/\sqrt{T} + b \log(c/T)$. Close to the quantum critical fillings ($n = 0.85$ for $t'/t = 0$, $n = 0.83$ for $t'/t = -0.1$, and $n = 0.78$ for $t'/t = -0.2$), $\chi'_{0d}(\omega = 0, T)$ shows a power-law divergence with decreasing temperature. The prefactor a associated with the square-root term increases as t' become negative. This signifies a stronger divergence in the pairing susceptibility.

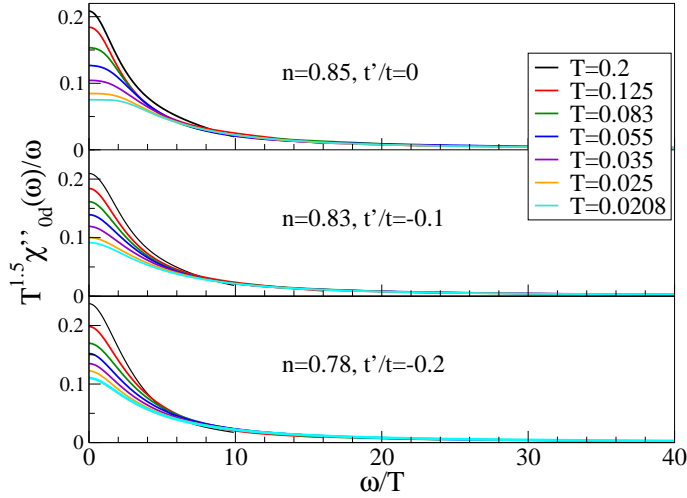


Figure 4.7: (Color online) Plots of $T^{1.5} \chi''_{0d}(\omega)/\omega$ versus ω/T close to the quantum critical doping ($n = 0.85$ for $t'/t = 0$, $n = 0.83$ for $t'/t = -0.1$, and $n = 0.78$ for $t'/t = -0.2$). As the temperature decreases, the curves coincide for $\omega/T > 9 \approx (4t/J)$ defining a scaling function $H(\omega/T)$, which corresponds to a contribution to $\chi'_{0d}(T) = \frac{1}{\pi} \int d\omega \chi''_{0d}(\omega)/\omega \propto \frac{1}{\sqrt{T}}$ as shown in Fig. 4.6. In the scaling regime, $H(\omega/T) \approx (\omega/T)^{-1.5}$.

term $\propto \frac{1}{\sqrt{T}}$ in the real part of $\chi'_{0d}(T)$.

4.4 Discussion

One of the important issues in the field of cuprate physics is the identification of the quantum critical point accepted by and large as relevant for the superconductivity and in particular for the strange “non-Fermi liquid” behavior observed in the vicinity of the maximum of the superconducting dome. Based on our numerical results presented here together with those published previously[134, 61, 62, 158, 23], a complete evolution of Fermi surface ($A(\mathbf{k}, \omega = 0)$) as a function of chemical potential and t'/t is given in Fig. 4.8. The Lifshitz points are highlighted in the red boxes. We also suggest the schematic phase diagram for the two dimensional Hubbard model shown in Figure 4.9 (note that for clarity we purposely neglect the antiferromagnetic region in this schematic plot). In this schematic phase diagram we also add a d -wave superconducting dome as a function of t'/t . The transition temperature T_c is obtained by extrapolating the lattice d -wave susceptibility from the DCA-INT-CTQMC calculation with $N_c = 16$ and $U = 6t$. The control parameters are the next-nearest-neighbor hopping t'/t , chemical potential μ , and temperature T . For each t' , we shift the chemical μ with respect to its value at half filling $\mu_{\text{HF}}(t'/t)$. For $t' > 0$, there is a first order phase separation transition between an insulating and incompressible Mott liquid (ML region in the lower inset of Fig. 4.9) and a weakly compressible metallic Mott gas (MG region in the lower inset of Fig. 4.9). As a function of temperature, this region of first order transitions terminates in a line of second order classical critical points (red dots and blue line for $t' > 0$). By varying t' this line of second order transitions is suppressed to $T = 0$. The corresponding $t' = 0$ doping defines the quantum critical point in the phase diagram.

This QCP separates the pseudogap regime from the Fermi liquid. As usual, one observes a V-shaped quantum critical region above this QCP, which shows the signatures of a marginal Fermi liquid. Note that this QCP at $t' = 0$ also involves a Lifshitz transition, i.e. a change in Fermi surface topology from electron-like in the Fermi liquid phase to hole-like in the pseudogap phase. This property can be directly inferred from the changes in the low-frequency structures of the spectral function (see Fig. 4.1). At the critical doping the van Hove singularity in the single particle density of states is located at the Fermi energy (see Fig. 4.2). Note that there are actually two effects involved. Firstly, the change in the overall shape of the Fermi surface, and secondly a distinctive suppression of spectral weight along the antinodal directions in the pseudogap phase. Based on the momentum resolution presently available, we are not able to make decisive statements about a possible formation of hole pockets. Higher momentum resolution would be necessary to unambiguously establish the nature of the Lifshitz transition. We are currently developing a multiscale dual Fermion dynamical cluster approach[177], which combines the DCA method used in this work with the recently introduced dual-Fermion formalism[178]. This approach can systematically incorporate the long-ranged correlations through the dual fermion lattice calculation, and will eventually provide us the necessary momentum resolution to address the question of the hole pockets and the type of Lifshitz transition associated with the QCP. However, the numerical data presented in this work are very indicative and indeed consistent with a collapse of the

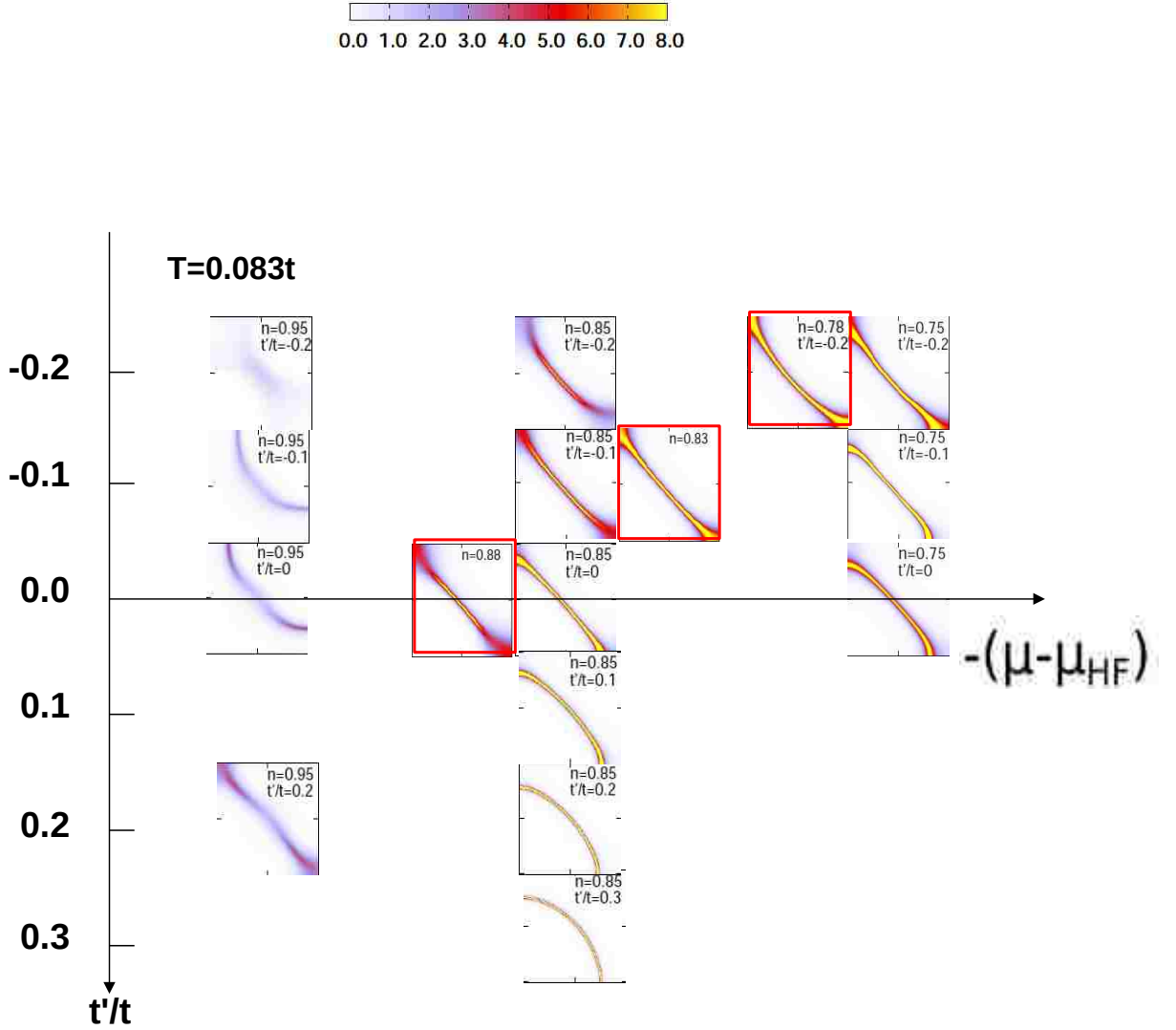


Figure 4.8: (Color online) Zero-frequency spectra $A(\mathbf{k}, \omega = 0)$ (equals to Fermi surface at large doping) as functions of next-nearest-neighbor hopping t'/t and the minus chemical potential with respect to its half-filled value at $T = 0.083t$ and $U = 6t$. When $t'/t \leq 0$, $-(\mu - \mu_{HF})$ is a monotonic function of the hole doping. The red boxes point out the parameters where $A(\mathbf{k}, \omega = 0)$ crosses the saddle point at $(\pi, 0)$ or $(0, \pi)$ and form a Lifshitz line associated with the topology of Fermi surface changing from electron-like (Fermi liquid) to hole-like (pseudogap).

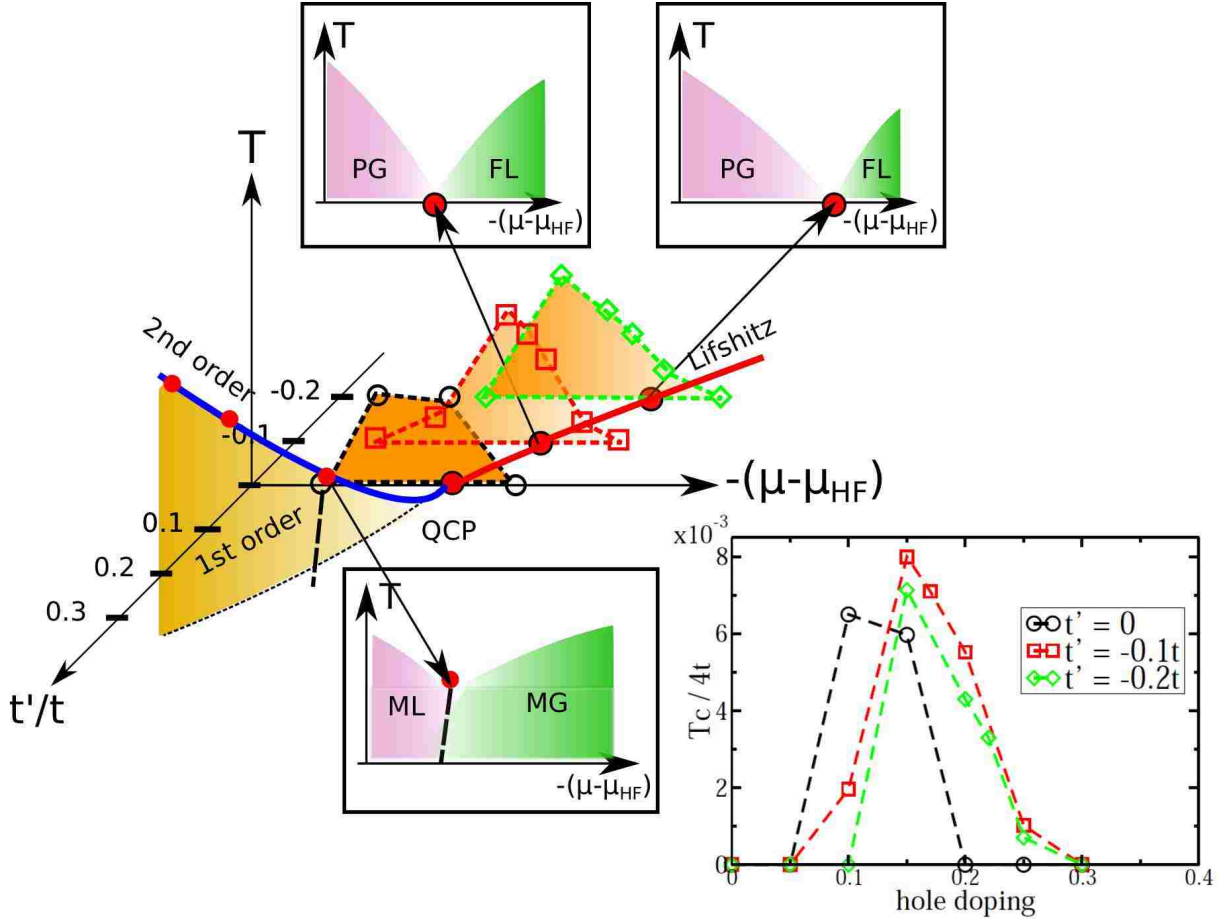


Figure 4.9: (Color online) Schematic phase diagram of the Hubbard model close to the quantum critical point (QCP) with temperature (T), chemical potential (μ), and next-nearest-neighbor hopping (t') as the control parameters. For clarity we neglect the anti-ferromagnetic phase. For each t' , we shift the chemical potential μ with respect to its half filling value $\mu_{HF}(t'/t)$. The three insets show the cut of the phase diagram at three different $t'/t = 0.1, -0.1$ and -0.2 . At positive t' , the Mott liquid and Mott gas phases are separated by a first order line; at negative t' , the pseudogap and the Fermi liquid phases are separated by a quantum critical region, and the region becomes wider as t' moves towards the negative direction. As the Lifshitz points move to larger hole doping at negative t' , the slope of the boundary between the pseudogap and the quantum critical region becomes less steep. The evolution of superconducting dome as a function t'/t is also plotted in the down-right inset.

Fermi surface from a large to a small one.

As t' becomes negative phase separation is suppressed, but the critical behavior associated with the Lifshitz transition remains, leading to a line of critical points at $T = 0$, as sketched in the schematic phase diagram in the region $t' < 0$. Since the effect of negative t' is to distort the Fermi surface towards hole-like (see Fig. 4.4), in the $t'/t < 0$ region of the phase diagram, one necessarily needs higher hole doping concentration to have the van Hove singularity locate at the Fermi level. This provides us a simple explanation for the fact that the Lifshitz points move to higher hole doping at $t' < 0$. Across the Lifshitz points, it is not only the change in shape of the Fermi surface, but more importantly the strong suppression of weight along the antinodal direction which leads to the interpretation of a Lifshitz transition at $T = 0$.

The quantum fluctuations here again lead to a region with quantum critical behavior. As it is commonly accepted, the low-energy model for the high- T_c cuprates is the two dimensional Hubbard model with at least $t > 0$ and $t' < 0$, we thus have strong numerical evidence that the QCP is indeed due to a transition of the Fermi surface topology, as already suggested by several other authors[166, 153]. We also find at negative t' that the quantum critical region becomes wider in the doping range (see the two upper insets of Fig. 4.9), the quantum critical points move to higher hole doping concentrations, and the boundary between the pseudogap region and quantum critical region becomes less steep as t' moves towards the negative direction.

There is, however, an important missing link. The explanation, for the interacting electron system, of why the van Hove singularity crosses the Fermi surface at the critical filling n_c , even for $t' = 0$, thus triggering the Lifshitz transition. In previous DCA studies of the 2D Hubbard model[179, 164], it was found that the non-local correlations present in the DCA, but missing in the single site dynamic mean field approximation (DMFA), tend to distort the Fermi surface of the hole doped system so that it is centered around the wavevector (π, π) rather than $(0, 0)$. As the system is doped away from half filling, these correlations become weaker, and the DCA Fermi surface returns to the DMFA Fermi surface centered around $(0, 0)$. Thus the topology of the Fermi surface changes from hole-like to electron-like at finite doping.

On the other hand, since the correlation effects at finite doping show strong temperature dependence, we expect the phenomena associated with the van Hove singularity also have a temperature dependence which is quite different from those predicted by models with a static van Hove singularity resulting from a saddle point in the bare dispersion[66]. This has important consequences for the superconducting transition T_c , which, at sufficiently high doping, is determined by the BCS-like condition $V_d \chi'_{0d}(\omega = 0) = 1$ where χ'_{0d} is the real part of the bare d-wave pairing susceptibility and V_d is the strength of the d-wave pairing interaction.

Following the results in Fig. 4.6 and 4.7, we find at $t' = 0$, $t'/t = -0.1$, and $t'/t = -0.2$, $\chi'_{0d}(\omega = 0)$ close to the van Hove singularity diverges quickly with decreasing temperature, roughly following the power-law behavior $\propto a/\sqrt{T}$, which is significantly different from the conventional BCS logarithmic divergence or the log-squared divergence found at a static van Hove singularity[171, 66]. Moreover, we find that the prefactor a increases with negative t' ,

which signifies a stronger divergence in the pairing bubble compared with the one at $t' = 0$. However, we also know the d -wave pairing vertex, V_d , decays monotonically with hole doping, since V_d originates predominantly from the spin channel[51, 62]. A negative t' will frustrate the antiferromagnetic background, and hence suppress the spin channel contribution to the d -wave pairing vertex. At the same time, according to our Lifshitz phase diagram (Fig. 4.9), one needs higher hole doping concentration to approach the QCP for negative t' . The higher quantum critical doping and the suppression of the spin channel contribution to the pairing vertex lead us to expect the d -wave pairing vertex, V_d , becomes even smaller for $t' < 0$ than it is for $t' = 0$. Hence, a more strongly divergent pairing bubble, χ'_{0d} , and a weaker pairing vertex, V_d , bring us to an interesting situation for $t' < 0$, where there is a competition between χ'_{0d} and V_d . Whether this competition will yield a higher T_c and larger superconducting dome in the doping range close to the Lifshitz points at negative t' will be the subject of future investigations.

Our phase diagram is also phenomenologically consistent with the recent proposal of unconventional quantum criticality at the border of a first order metal-insulator transition and a continuous transition triggered by quantum fluctuations[137, 138, 139]. This marginal quantum critical point belongs to an unprecedented universality class and has unique feature with combined characteristics of symmetry breaking and topological (Lifshitz) transitions[140]. Whether the Lifshitz points presented at $t'/t \leq 0$ in this work display unconventional quantum criticality is also a subject of further studies.

4.5 Conclusion

Using large-scale dynamical cluster quantum Monte Carlo simulations, we map out the Lifshitz phase diagram of the two dimensional Hubbard model in the vicinity of the quantum critical fillings. The control parameters of the phase diagram are temperature T , chemical potential, and the next-nearest-neighbor hopping t'/t . Consistent with our previous results[134, 23, 158], we find at positive t' a first order phase separation transition which is terminated by a second order critical point. As $t' \rightarrow 0$, the second order terminus is driven to zero temperature, and becomes the QCP separating the pseudogap and the Fermi liquid phases. Here, we extend the investigation into negative t' , and find out a line of van Hove singularities where the Fermi surface topology changes from electron-like in the Fermi liquid region to hole-like in the pseudogap region of the phase diagram. The points on this line of van Hove singularities hence are the quantum critical points where the Lifshitz transition occurs. Close to these QCPs, the bare d -wave pairing bubble diverges algebraically in temperature. Originating from these Lifshitz points, the V-shaped quantum critical region emerges with marginal Fermi liquid properties and vanishing quasiparticle weight[61, 23]. We also find the V-shaped quantum critical region becomes wider in doping range (and chemical potential) as t'/t becomes negative.

There remain a number of interesting open issues, including the possible formation of hole pockets in the pseudogap phase, the reason of the van Hove singularity crossing the Fermi surface at the quantum critical doping, the superconducting transition temperature T_c and the shape of the superconducting dome at negative t' , and the possible unconventional

quantum criticality associated with the Lifshitz transition points. All these questions require not only massively parallel large-scale simulations, but more importantly, new techniques that will greatly increase the momentum resolution. In fact, progress has already been made along these directions[177], and the remaining questions will be addressed in future work.

Chapter 5

Unconventional Superconductivity on the Triangular Lattice Hubbard Model

Using large-scale dynamical cluster quantum Monte Carlo simulations, we explore the unconventional superconductivity in the hole-doped Hubbard model on the triangular lattice. Due to the interplay of electronic correlations, geometric frustration, and Fermi surface topology, we find a doubly degenerate singlet pairing state at an interaction strength close to the bare bandwidth. Such an unconventional superconducting state is mediated by antiferromagnetic spin fluctuations along the Γ - K direction, where the Fermi surface is nested. An exact decomposition of the irreducible particle-particle vertex further confirms the dominant component of the effective pairing interaction comes from the spin channel. Our findings provide support for chiral $d+id$ superconductivity in water-intercalated sodium cobaltates $\text{Na}_x\text{CoO}_2 \cdot y\text{H}_2\text{O}$, as well as insight into the superconducting phases of the organic compounds κ -(ET) $_2$ X and Pd(dmit) $_2$.

My contribution to this work is to establish the INT-CTQMC codes with the tables containing the triangular Betts lattice built by Dr. Unjong Yu. I also establish the following analysis codes with the tables including the MEM code, the analysis codes of finding leading eigenvalues of the pairing matrix, the analysis codes of decomposing the irreducible vertex, and the analysis codes to calculate the transport properties using the Kubo's formula. This chapter has been published in the Phys. Rev. B **88**, 041103(R) (2013)[25].

5.1 Introduction

Since the discovery of the Cu-based high temperature superconductors, the search for new unconventional superconductors is among the central topics in condensed-matter physics[35]. The water-intercalated sodium cobaltates $\text{Na}_x\text{CoO}_2 \cdot y\text{H}_2\text{O}$ [17, 33, 34] and two families of organic charge-transfer salts κ -(ET) $_2$ X and Pd(dmit) $_2$ [26, 32, 27, 28, 29, 30] are of particular interest. The underlying structure of these layered materials is the geometrically frustrated triangular lattice. The competition between electronic correlations and geometric frustration yields novel phenomena. For example, the most frustrated members of the κ -(ET) $_2$ X and Pd(dmit) $_2$ families are believed to host quantum spin liquid states[15], and the recently discovered 5K superconducting phase in $\text{Na}_x\text{CoO}_2 \cdot y\text{H}_2\text{O}$ might be a chiral state which breaks parity and time reversal giving rise to interesting edge modes that can carry quantized particle and spin currents[180, 36, 181].

The layered triangular lattice compound $\text{Na}_x\text{CoO}_2 \cdot y\text{H}_2\text{O}$ has a superconducting dome for $x \sim 0.3$, $y \sim 1.3$ at $T_c \sim 5\text{K}$ [17, 33, 34]. Due to intercalation, its electronic structure is effectively two-dimensional. A very rich phase diagram has been mapped out for a range of Na concentrations[34]; however, the nature of the superconducting phase has remained poorly understood. Recent measurements on high quality single crystals[182] show that the spin contributions to the Knight shift decreases below T_c along the a and c axes, supporting

the notion that the Cooper pairs are formed in a spin-singlet state. The temperature and doping dependence of the Knight shift and the relaxation rate above T_c provide evidence of antiferromagnetic correlations[182, 183].

There are a number of theoretical proposals for the unconventional superconductivity in the cobaltates. The underlying triangular lattice belongs to the C_{6v} symmetry group and allows a doubly degenerate E_2 representation of the superconducting order parameter with $d_{x^2-y^2}$ and d_{xy} degenerate states[35, 36, 37], raising the exciting possibility of a time-reversal symmetry breaking chiral $d_{x^2-y^2} \pm id_{xy}$ superconductor. Earlier studies of the cobaltates draw analogy to the cuprates and employed either a phenomenological RVB theory[184], or a slave boson mean-field approach[185] to provide signatures of a spin-singlet $d + id$ pairing state. Recent studies of the sodium cobaltates using a Gutzwiller projection supplemented by symmetry arguments[180], as well as the multi-orbital functional renormalization group[181], reveal a rich phase diagram with an anisotropic $d + id$ phase and a possible topological quantum phase transition through a nodal superconducting state. However, one needs to bear in mind that prior approaches suffer either from their mean-field nature, or their incapability of capturing correlation effects in the strong coupling regime. Hence, there is an urgent need of unbiased studies, where the interplay of strong electronic correlations and geometric frustration can be treated in a non-perturbed fashion.

The simplest model that captures the essential physics of the cobaltates and organic compounds is the single-band Hubbard model on a triangular lattice. In this Letter, we explore the low-energy properties of this model by large-scale dynamical cluster quantum Monte Carlo simulations[47]. We focus on the different superconducting instabilities in the hole-doped side of the phase diagram. To the best of our knowledge, this is the first study of the hole-doped Hubbard model on the triangular lattice exploring the pairing symmetries on different cluster sizes. Clusters up to size $N_c = 12$ allow a greater momentum resolution and higher quality data on the spectral function, self energy, and different superconducting susceptibilities. Therefore, we obtain an unambiguous signature of an unconventional doubly-degenerate superconducting state in the strong to intermediate coupling region. By explicitly comparing the pairing susceptibility in the s -, $d_{x^2-y^2}$ -, d_{xy} -wave singlet channels and the f -wave triplet channel, we find that the $d_{x^2-y^2}$ and d_{xy} components are most divergent and extrapolate to the same T_c within our numerical accuracy. We identify that the pairing is mediated by strong spin fluctuations along the antiferromagnetically (AF) ordered wavevector on the Γ to K direction. The Fermi surface (FS) is nested along this AF wavevector, but the system only orders at half-filling in the Heisenberg limit. An exact decomposition of the irreducible particle-particle vertex furthermore reveals the dominant part in the effective pairing interaction comes from the spin channel.

5.2 Formalism

The Hamiltonian of the system is defined in the eq. (2.23) with the bare dispersion is given by the eq. (2.4). We investigate one and two-particle properties of the model using the dynamical cluster approximation (DCA)[119](section 2.2.3) with weak-coupling continuous time quantum Monte Carlo (CTQMC)[49](section 2.3) as the cluster solver. The DCA

maps the original lattice onto a periodic cluster of size N_c embedded in a self-consistently determined host. Spatial correlations inside a cluster are treated explicitly while those at longer length scales are described at the mean-field level. In this work we choose clusters of sizes $N_c = 4, 6, 8$ and 12 . We study inverse temperatures up to $\beta t = 16.5$. We obtain the cluster self-energy $\Sigma(\mathbf{K}, \omega)$ via the maximum entropy method[57] (MEM, section 2.4) applied directly to the Matsubara-frequency self energies calculated by the DCA-CTQMC[118, 24]. We then interpolate the $\Sigma(\mathbf{K}, \omega)$ to obtain the lattice self energy, $\Sigma(\mathbf{k}, \omega)$, and lattice spectral function, $A(\mathbf{k}, \omega)$.

To obtain various susceptibilities, $\chi(T)$, we extract the irreducible vertex function Γ via the Bethe-Salpeter equation (eq. (2.132)) from the two-particle Green function measured on the cluster, then employing $\chi(T) = \frac{\chi_0}{1 - \Gamma\chi_0}$, where χ_0 is the bare susceptibility constructed from the dressed one-particle lattice Green function. The superconducting pairing susceptibilities are obtained from the particle-particle channel, and the charge and spin susceptibilities are obtained from the particle-hole channel. We further separate the pairing susceptibilities explicitly into spin singlet and triplet channels, where in the singlet channel we project the $\chi(T)_{pairing}$ onto s -, $d_{x^2-y^2}$ -, and d_{xy} -wave, and in the triplet channel we project it onto the f -wave channel, with the corresponding form factors defined in the eq. (2.153) to (2.158)[35, 181] (section 2.3.3).

To explore the pairing mechanism we decompose the particle-particle pairing vertex Γ into the fully irreducible vertex Λ , the charge ($S = 0$) particle-hole contribution, Φ_c , and the spin ($S = 1$) particle-hole contribution, Φ_s , through the parquet equation, $\Gamma = \Lambda + \Phi_c + \Phi_s$ [51](section 2.3.4). We furthermore project the previous expression using different form factors such as $d_{x^2-y^2}$ and d_{xy} ,

$$V_{d_{x^2-y^2}/d_{xy}} = V_{d_{x^2-y^2}/d_{xy}}^\Lambda + V_{d_{x^2-y^2}/d_{xy}}^C + V_{d_{x^2-y^2}/d_{xy}}^S, \quad (5.1)$$

where each term is the projected component of the corresponding term in the parquet equation[62]. In this way, we are able to distinguish which component contributes the most to the effective pairing interaction.

5.3 Results

Fig. 5.1 displays the cluster spin susceptibility at different fillings, $n = 0.667, 0.8$, and 1 , and coupling $U = 8.5t$. The data are obtained from DCA-CTQMC simulations with cluster size $N_c = 12$, and we interpolate the cluster susceptibility into the entire Brillouin zone (BZ). At very high hole-doping, $n = 0.667$, the susceptibility is mostly flat. As the filling increases, $n = 0.8$, the spin susceptibility develops six bumps at the K points. When $n = 1$, the bumps become more pronounced. The vector connecting Γ to K is the antiferromagnetically ordered wave vector (\vec{Q}_{AF}) in the Heisenberg limit of the half-filled model. The cluster spin susceptibility demonstrates that the antiferromagnetic fluctuations become stronger as the filling moves towards $n = 1$. The pairing of electrons may be mediated by these fluctuations[186, 187].

Fig. 5.2 shows the Fermi surface (FS) at the same fillings used in the previous figure. Fig. 5.2(a) corresponds to the non-interacting limit. At $n = 0.667, 0.8$ and 1 the FS is

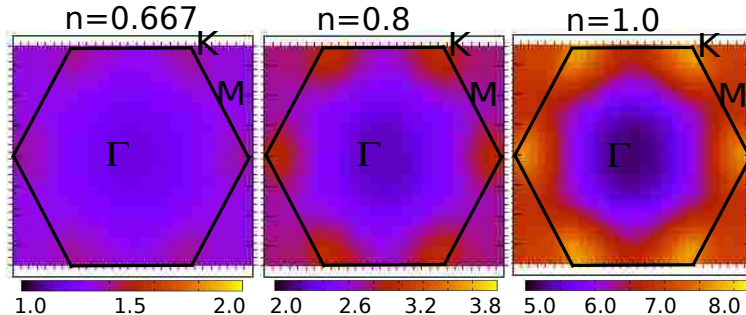


Figure 5.1: (Color online) Cluster spin susceptibility for $N_c = 12$, interaction strength $U = 8.5t$, temperature $T = 0.1t$ and different fillings, $n = 0.667, 0.8$, and 1 .

close to a perfect circle. The van Hove singularity in the non-interacting band structure is present at $n = 1.5$ with saddle points at M . One-loop RG calculations[188] show the FS in the hole-doped side is stable against weak Coulomb interactions. However, under strong interaction, the FS begins to deform and new phenomena such as superconductivity emerges. Fig. 5.2(b) displays the FS at $n = 0.667$, $U = 8.5t$, which is slightly deformed towards a hexagon. The red arrow corresponds to $\overrightarrow{Q_{AF}}$, while the pink arrow is this vector shifting its center to Γ and rotating it by 60° . For $n = 0.667$ the pink arrow is longer than the diameter of the FS so there is no nesting effect, and we do not observe superconductivity at this filling. In Fig.5.2(c), $n = 0.8$, the FS is more deformed, the $\overrightarrow{Q_{AF}}$ now connects significant sections of the FS, and as illustrated in Fig. 5.1, the AF fluctuations are stronger. The nesting effect and the strong AF fluctuations together give rise to diverging pairing susceptibilities at filling $n = 0.8$ and 0.9 , as discussed below. At half-filling, $n = 1$, the FS is further deformed towards a hexagon, but the spectral weight become less coherent due to the strong interaction. Interestingly, the nesting vector now is shorter than the diameter of the FS. Hence, even through the AF fluctuations are the strongest here, electrons on the FS are hard to pair by $\overrightarrow{Q_{AF}}$, the system is rather subject to a Mott transition, whose novel features are beyond the scope of this thesis.

Fig. 5.3 displays the inverse pairing susceptibility as a function of temperature, $1/\chi_{pairing}(T)$, at filling $n = 0.9$, $U = 8.5t$, and $N_c = 6$. Here we explicitly project the lattice pairing susceptibility in the s -, $d_{x^2-y^2}$ -, and d_{xy} -wave singlet channels and the f -wave triplet channel by using the appropriate form factors. Fig. 5.3 shows that the two singlet d -wave components are the most divergent ones. Within our numerical resolution their $1/\chi_{pairing}$ extrapolate to zero at the same superconducting transition temperature, T_c . This implies that the superconducting order parameter is doubly degenerate with components $d_{x^2-y^2}$ and d_{xy} . Based on symmetry arguments any linear combination of both d -wave components is possible below T_c . However, both Ginzburg-Landau and BCS-type mean-field approaches favor superconducting phases that break the time-reversal symmetry for singlet multicomponent superconductors[189, 190], such as the $d+id$ singlet pairing state predicted in graphene[36, 37] and the cobaltates[180, 181]. Therefore, our findings support the possibility of a chiral $d+id$ superconducting phase in the hole-doped triangular Hubbard model. The inset of Fig. 5.3

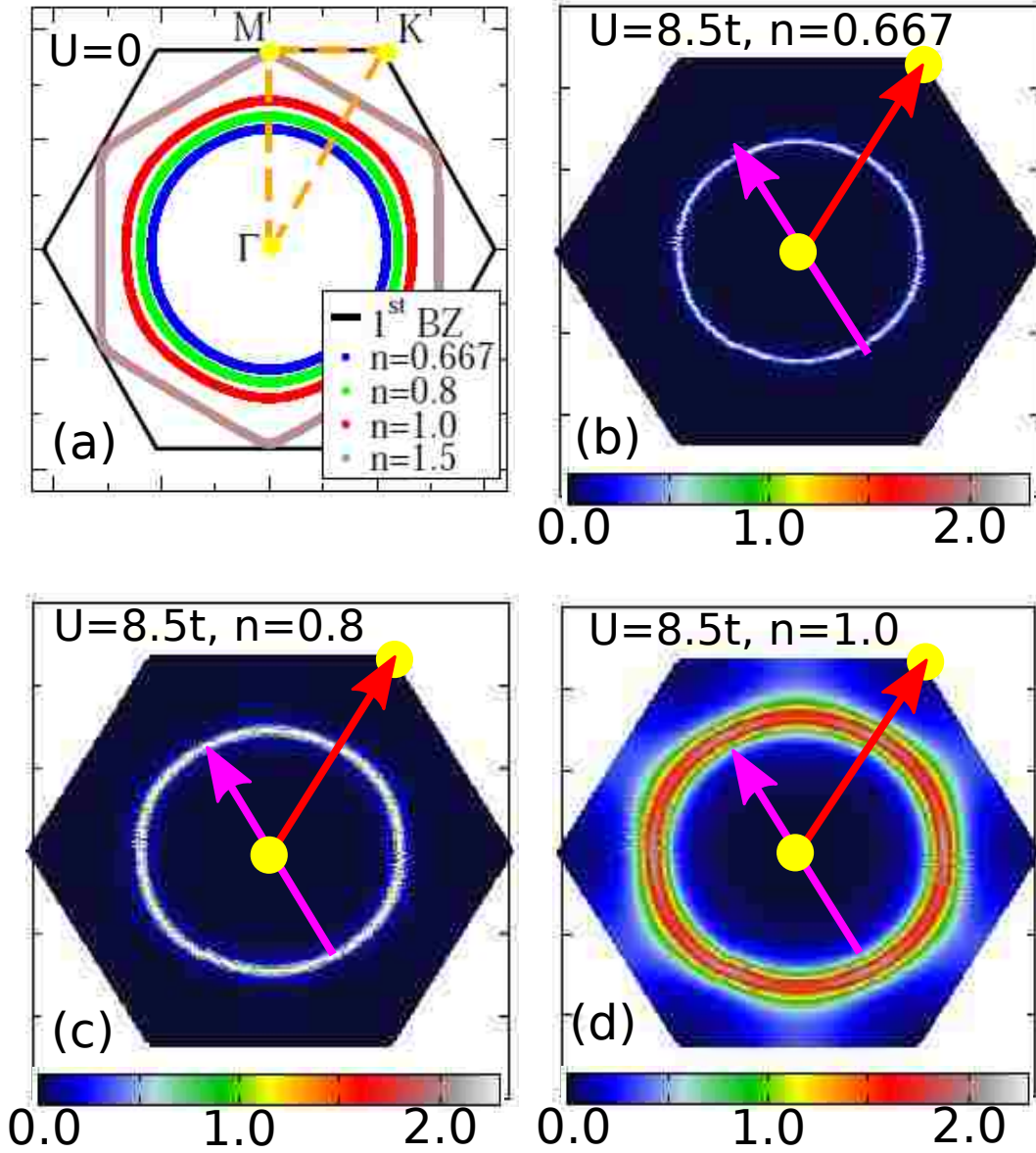


Figure 5.2: (Color online) (a) First Brillouin zone, the symmetric path $\Gamma - M - K - \Gamma$ and the non-interacting Fermi surface at different band fillings. (b), (c), (d) Spectral function $A(\mathbf{k}, \omega = 0)$ on the Fermi surface for $N_c = 12$ DCA-CTQMC simulations with $U = 8.5t$, $T = 0.1t$, and $n = 0.667$ in (b), $n = 0.8$ in (c), and $n = 1$ in (d). Red arrow is the AF ordered wave vector (\vec{Q}_{AF}) and the pink arrow is after shifting its center to Γ and rotating it by 60° .

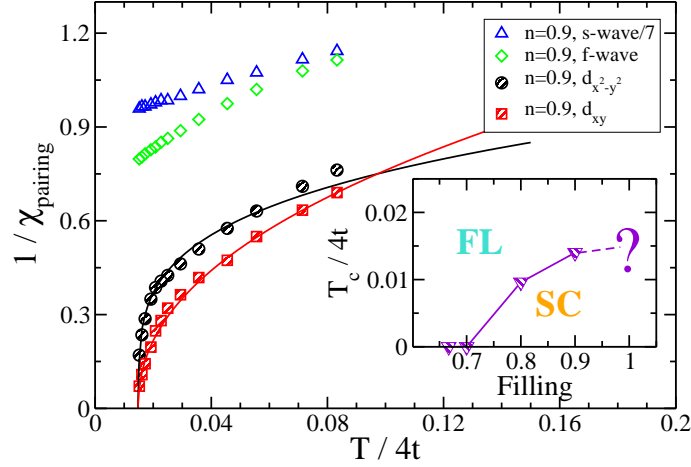


Figure 5.3: (Color online) Inverse pairing susceptibility, $1/\chi_{pairing}$, for $N_c = 6$, $U = 8.5t$ and $n = 0.9$. The singlet s -wave and triplet f -wave do not diverge, whereas the singlet pairing channels with $d_{x^2-y^2}$ - and d_{xy} -wave symmetry show a divergency at the same T_c . Note that we have multiplied by a factor of 7 the s -wave pairing susceptibility in order to use the same vertical scale. (Inset) The superconducting transition temperature T_c as a function of doping. FL and SC label the Fermi liquid and superconducting regions, respectively.

shows the phase diagram for different doping concentrations based on $N_c = 6$ DCA-CTQMC simulations. T_c becomes finite for doping larger than $n = 0.7$ due to the onset of FS nesting and strong AF correlations, and increases as n approaches 1, reflecting that the AF fluctuations become stronger towards half-filling. However, the nature of the ground state at half-filling is still unclear due to a worsened minus-sign problem in our simulations.

To shine light on the dominant contribution to the pairing interaction, we use the parquet equations to decompose the irreducible particle-particle vertex function, and project each term onto its $d_{x^2-y^2}$ and d_{xy} components. The results are presented in Fig. 5.4 for a DCA-CTQMC simulation with cluster size $N_c = 12$, $U = 8.5t$ and filling $n = 0.9$. The left, right panels correspond to the d_{xy} , $d_{x^2-y^2}$ projection of the parquet equations, respectively. In both cases, the dominant contribution to the effective pairing interactions $V_{d_{xy}}$ and $V_{d_{x^2-y^2}}$ is from the magnetic, spin $S = 1$, particle-hole channel, $V_{d_{xy}}^S$ and $V_{d_{x^2-y^2}}^S$. In fact, we also find that the pairing interaction, $V_{d_{xy}/d_{x^2-y^2}}(\mathbf{k} - \mathbf{k}')$ is peaked at momentum transfer $|\mathbf{k} - \mathbf{k}'| = |\overrightarrow{Q_{AF}}|$. The vertex decomposition confirms that this peak comes from the spin channel $V_{d_{xy}/d_{x^2-y^2}}^S(\overrightarrow{Q_{AF}})$ (not shown). Note that both $N_c = 6$ and 12 size clusters have the cluster points connected by $\overrightarrow{Q_{AF}}$. From the BCS gap equation[189]

$$\Delta_{\mathbf{k}} = -\frac{1}{N} \sum_{\mathbf{k}'} V^{SC}(\mathbf{k} - \mathbf{k}') \frac{\Delta_{\mathbf{k}'}}{2E(\mathbf{k}')} \tanh\left(\frac{E(\mathbf{k}')}{2T}\right), \quad (5.2)$$

where $E(\mathbf{k}) = \sqrt{\epsilon_{\mathbf{k}}^2 + \Delta_{\mathbf{k}}^2}$, we infer that if the superconducting pairing interaction $V^{SC}(\mathbf{k} - \mathbf{k}')$

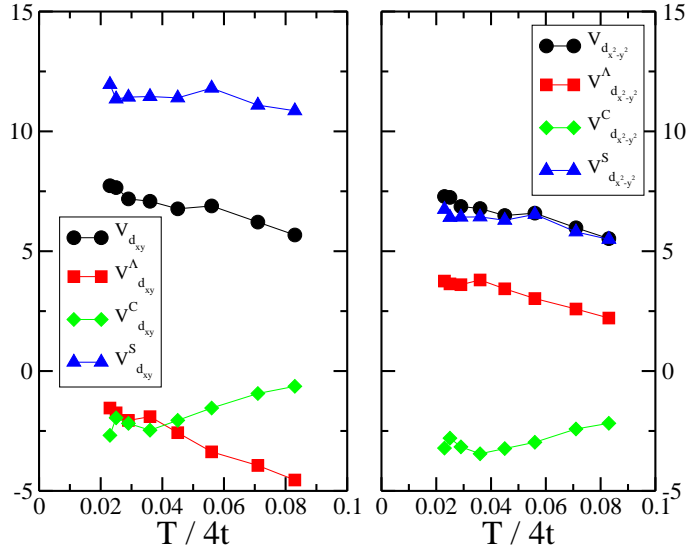


Figure 5.4: (Color online) Left: d_{xy} projected contributions to the pairing vertex $V_{d_{xy}}$, from the fully irreducible vertex $V_{d_{xy}}^\Lambda$, charge $V_{d_{xy}}^C$ and spin $V_{d_{xy}}^S$ cross channels versus T at $n = 0.9$, $U = 8.5t$. Right: the $d_{x^2-y^2}$ -wave projection of the same quantities. In both cases, the contribution to the pairing interaction from spin channel is clearly dominant.

is peaked at $\overrightarrow{Q_{AF}}$, the order parameters $\Delta_{\mathbf{k}}$ which correspond to $d_{x^2-y^2}$, d_{xy} and f -waves are equally favored in the $N_c = 6$ and 12 clusters. Our results suggest that d_{xy} and $d_{x^2-y^2}$ singlet pairing are favored over the f -wave triplet pairing, probably because f -wave has a more complex nodal structure than the two d -waves[35].

5.4 Conclusion

Using large-scale dynamical cluster quantum Monte Carlo simulations, we find a doubly degenerate singlet pairing state at interaction strength close to the bare bandwidth and filling larger than $n = 0.7$ in the hole-doped Hubbard model on the triangular lattice. Our findings support the presence of a chiral $d + id$ singlet superconducting phase in this model. The pairing mechanism comes from antiferromagnetic spin fluctuations at the magnetic order wavevector nesting the deformed FS. A decomposition of the vertex further confirms that the spin channel contributes the most to the effective pairing interaction.

Chapter 6

General Conclusion and Outlook

In this thesis, we try to understand the physics of unconventional superconductivity both on the square- and triangular-lattice Hubbard models using large-scale dynamical cluster quantum Monte Carlo simulations. For the square-lattice Hubbard model near the optimal hole doping, we find the formation of d -wave pairings is due to the C_4 symmetry of the Fermi surface and the antiferromagnetic instability with nesting wavevector $\mathbf{q} = (\pi, \pi)$. The high transition temperature may originate from a quantum critical point (QCP) beneath the superconducting dome at the ground state. For the triangular-lattice Hubbard model on the hole-doped side, the $d+id$ pairing comes from the C_{6v} symmetry of the nested Fermi surface and the instability of the antiferromagnetic susceptibility with $\mathbf{q} = (\frac{2\pi}{3}, \frac{2\pi}{\sqrt{3}})$. Whether there is a QCP on the phase diagram of the triangular-lattice Hubbard model at half filling close to the metal-insulator transition (MIT) requires future investigations.

In the square-lattice Hubbard model, we also identify a line of Lifshitz transition associated with the change of topology of the Fermi surface. The van Hove singularity crossing the Fermi level is the characteristic feature of the Lifshitz points. Similarly, the Fermi surface for the triangular-lattice Hubbard model will also change its topology at filling $n \approx 1.5$. The properties of such a Lifshitz transition also needs future studies.

For future topics, we find that there is a similarity between the n - T phase diagram for the square-lattice Hubbard model with U fixed and the U - T phase diagram for the triangular-lattice Hubbard model with n fixed at 1. For the square lattice, MIT occurs when the filling n moves toward the half filling under a fixed interaction U , while for the triangular lattice, MIT when the interaction U increases toward U_c for $n = 1$. The pseudo-gap physics before the MIT is discovered for the square case while the long sought “spin-liquid” physics on the triangular lattice is still a mystery. Due to the serious minus sign problem at large U , to study the triangular lattice at or above half filling in the strongly correlated regime, we will improve our numerical method using the strong-coupling quantum Monte Carlo solver to investigate the physics when $U \geq U_c$.

Bibliography

- [1] H. Kamerlingh Onnes. Further experiments with liquid helium. G. On the electrical resistance of pure metals, etc. VI. On the sudden change in the rate at which the resistance of mercury disappears. *Comm. Phys. Lab. Univ. Leiden*, page 124, 1911.
- [2] J. Bardeen, L. N. Cooper, and J. R. Schrieffer. Theory of Superconductivity. *Phys. Rev.*, **108**:1175–1204, Dec 1957.
- [3] Leon N. Cooper. Bound Electron Pairs in a Degenerate Fermi Gas. *Phys. Rev.*, **104**:1189–1190, Nov 1956.
- [4] J. R. Schrieffer, D. J. Scalapino, and J. W. Wilkins. Effective Tunneling Density of States in Superconductors. *Phys. Rev. Lett.*, **10**:336–339, Apr 1963.
- [5] P. Morel and P. W. Anderson. Calculation of the Superconducting State Parameters with Retarded Electron-Phonon Interaction. *Phys. Rev.*, **125**:1263–1271, Feb 1962.
- [6] W. L. McMillan. Transition Temperature of Strong-Coupled Superconductors. *Phys. Rev.*, **167**:331–344, Mar 1968.
- [7] M. R. Norman. Unconventional Superconductivity. *arXiv:1302.3176*, 2013.
- [8] D. D. Osheroff, R. C. Richardson, and D. M. Lee. Evidence for a New Phase of Solid He³. *Phys. Rev. Lett.*, **28**:885–888, Apr 1972.
- [9] G. R. Stewart. Heavy-fermion systems. *Rev. Mod. Phys.*, **56**:755–787, Oct 1984.
- [10] J. G. Bednorz and K. A. Müller. Possible high-T_c superconductivity in the Ba-La-Cu-O system. *Zeit. Physik, B*, **64**:189–193, 1986.
- [11] W. A. Little. Possibility of Synthesizing an Organic Superconductor. *Phys. Rev.*, **134**:A1416–A1424, Jun 1964.
- [12] F. Steglich, J. Aarts, C. D. Bredl, W. Lieke, D. Meschede, W. Franz, and H. Schäfer. Superconductivity in the Presence of Strong Pauli Paramagnetism: CeCu₂Si₂. *Phys. Rev. Lett.*, **43**:1892–1896, Dec 1979.
- [13] B. T. Matthias, T. H. Geballe, and V. B. Compton. Superconductivity.
- [14] L. Gao, Y. Y. Xue, F. Chen, Q. Xiong, R. L. Meng, D. Ramirez, C. W. Chu, J. H. Eggert, and H. K. Mao. Superconductivity up to 164K in HgBa₂Ca_{m-1}Cu_mO_{2m+2+δ} (m= 1, 2, and 3) under quasihydrostatic pressures. *Phys. Rev. B*, **50**:4260–4263, Aug 1994.

- [15] P.W. Anderson. Resonating valence bonds: A new kind of insulator? *Materials Research Bulletin*, **8**:153–160, Feb 1973.
- [16] Patrick A. Lee. An End to the Drought of Quantum Spin Liquids. *Science*, **321**:1306–1307, Sept 2008.
- [17] Eiji Takayama-Muromachi Fujio Izumi Ruben A. Dilanian Kazunori Takada, Hiroya Sakurai and Takayoshi Sasaki. Superconductivity in two-dimensional CoO₂ layers. *Nature*, **422**:53–55, Mar 2003.
- [18] C. M. Varma. Proposal for an experiment to test a theory of high-temperature superconductors. *Phys. Rev. B*, **61**:R3804–R3807, Feb 2000.
- [19] S. Sachdev. *Quantum Phase Transitions*. Cambridge University Press, 1999.
- [20] C. G. Olson, R. Liu, D. W. Lynch, R. S. List, A. J. Arko, B. W. Veal, Y. C. Chang, P. Z. Jiang, and A. P. Paulikas. High-resolution angle-resolved photoemission study of the Fermi surface and the normal-state electronic structure of Bi₂Sr₂CaCu₂O₈. *Phys. Rev. B*, **42**:381–386, Jul 1990.
- [21] J. C. Campuzano T. Takahashi M. Randeria M. R. Norman T. Mochikuparallel K. Kawakiparallel H. Ding, T. Yokoya and J. Giapintzakis. Spectroscopic evidence for a pseudogap in the normal state of underdoped high-Tc superconductors. *Nature*, **382**:51–54, Jul 1996.
- [22] D. S. Dessau D. S. Marshall C. H. Park P. Fournier A. G. Loeser, Z.-X. Shen and A. Kapitulnik. Excitation Gap in the Normal State of Underdoped Bi₂Sr₂CaCu₂O_{8+δ}. *Science*, **273**:325–329, Jul 1996.
- [23] K.-S. Chen, S. Pathak, S.-X. Yang, S.-Q. Su, D. Galanakis, K. Mielsons, M. Jarrell, and J. Moreno. Role of the van Hove singularity in the quantum criticality of the Hubbard model. *Phys. Rev. B*, **84**:245107, Dec 2011.
- [24] K.-S. Chen, Z. Y. Meng, T. Pruschke, J. Moreno, and M. Jarrell. Lifshitz transition in the two-dimensional Hubbard model. *Phys. Rev. B*, **86**:165136, Oct 2012.
- [25] Kuang Shing Chen, Zi Yang Meng, Unjong Yu, Shuxiang Yang, Mark Jarrell, and Juana Moreno. Unconventional superconductivity on the triangular lattice hubbard model. *Phys. Rev. B*, 88:041103, Jul 2013.
- [26] Y. Shimizu, K. Miyagawa, K. Kanoda, M. Maesato, and G. Saito. Spin Liquid State in an Organic Mott Insulator with a Triangular Lattice. *Phys. Rev. Lett.*, **91**:107001, Sep 2003.
- [27] Masaharu Oguni Yugo Oshima Hiroyuki Nojiri Yasuhiro Shimizu Kazuya Miyagawa Satoshi Yamashita, Yasuhiro Nakazawa and Kazushi Kanoda. Thermodynamic properties of a spin-1/2 spin-liquid state in a \hat{I}^0 -type organic salt. *Nature Physics*, **4**:459–462, Apr 2008.

- [28] Yuichi Kasahara Takahiko Sasaki Naoki Yoneyama Norio Kobayashi Satoshi Fujimoto Takasada Shibauchi Minoru Yamashita, Norihito Nakata and Yuji Matsuda. *Nature Physics*, **5**:44–47, Nov 2009.
- [29] T. Itou, A. Oyamada, S. Maegawa, M. Tamura, and R. Kato. *Phys. Rev. B*, **77**:104413, Mar 2008.
- [30] Yasuhiro Nakazawa Masafumi Tamura Satoshi Yamashita, Takashi Yamamoto and Reizo Kato. Gapless spin liquid of an organic triangular compound evidenced by thermodynamic measurements. *Nature Communications*, **2**:275, Apr 2011.
- [31] K. Kanoda and R. Kato. *Annu. Rev. Condens. Matter Phys.*, **2**:167, 2011.
- [32] Y. Kurosaki, Y. Shimizu, K. Miyagawa, K. Kanoda, and G. Saito. *Phys. Rev. Lett.*, **95**:177001, Oct 2005.
- [33] M. L. Foo R. E. Schaak, T. Klimczuk and R. J. Cava. Superconductivity phase diagram of $\text{Na}_x\text{CoO}_2 \cdot 1.3\text{H}_2\text{O}$. *Nature*, **424**:527–529, Jul 2003.
- [34] Maw Lin Foo, Yayu Wang, Satoshi Watauchi, H. W. Zandbergen, Tao He, R. J. Cava, and N. P. Ong. Charge Ordering, Commensurability, and Metallicity in the Phase Diagram of the Layered Na_xCoO_2 . *Phys. Rev. Lett.*, **92**:247001, Jun 2004.
- [35] Manfred Sgrist and Kazuo Ueda. Phenomenological theory of unconventional superconductivity. *Rev. Mod. Phys.*, **63**:239–311, Apr 1991.
- [36] L. S. Levitov Rahul Nandkishore and A. V. Chubukov. *Nature Physics*, **8**:158–163, Jan 2012.
- [37] Maximilian L. Kiesel, Christian Platt, Werner Hanke, Dmitry A. Abanin, and Ronny Thomale. Competing many-body instabilities and unconventional superconductivity in graphene. *Phys. Rev. B*, **86**:020507, Jul 2012.
- [38] J. Hubbard. Electron correlations in narrow energy bands. *Proceedings of the Royal Society A*, **276**(1365):238–257, 1963.
- [39] Antoine Georges, Gabriel Kotliar, Werner Krauth, and Marcelo J. Rozenberg. Dynamical mean-field theory of strongly correlated fermion systems and the limit of infinite dimensions. *Rev. Mod. Phys.*, **68**:13–125, Jan 1996.
- [40] Guy Makov Nathan Argaman. Density functional theory: An introduction. *American Journal of Physics*, **68**:69, January 2000.
- [41] M. Jarrell. Hubbard model in infinite dimensions: A quantum Monte Carlo study. *Phys. Rev. Lett.*, **69**:168–171, Jul 1992.
- [42] Antoine Georges and Gabriel Kotliar. Hubbard model in infinite dimensions. *Phys. Rev. B*, **45**:6479–6483, Mar 1992.

- [43] J. K. Freericks and Mark Jarrell. Magnetic Phase Diagram of the Hubbard Model. *Phys. Rev. Lett.*, **74**:186–189, Jan 1995.
- [44] Mark Jarrell, Hanbin Pang, D. L. Cox, and K. H. Luk. Two-Channel Kondo Lattice: An Incoherent Metal. *Phys. Rev. Lett.*, **77**:1612–1615, Aug 1996.
- [45] M. H. Hettler, M. Mukherjee, M. Jarrell, and H. R. Krishnamurthy. Dynamical cluster approximation: Nonlocal dynamics of correlated electron systems. *Phys. Rev. B*, **61**(19):12739–12756, May 2000.
- [46] Th. Pruschke Th. Maier, M. Jarrell and J. Keller. A non-crossing approximation for the study of intersite correlations. *European Physical Journal B*, **13**(1):613 – 624, 2000.
- [47] Thomas Maier, Mark Jarrell, Thomas Pruschke, and Matthias H. Hettler. Quantum cluster theories. *Rev. Mod. Phys.*, **77**:1027–1080, Oct 2005.
- [48] J S Flynn D D Betts, H Q Lin. Improved finite-lattice estimates of the properties of two quantum spin models on the infinite square lattice. *Canadian Journal of Physics*, **77**(5):353–369, 1999.
- [49] A. N. Rubtsov, V. V. Savkin, and A. I. Lichtenstein. Continuous-time quantum Monte Carlo method for fermions. *Phys. Rev. B*, **72**(3):035122, Jul 2005.
- [50] F. F. Assaad and T. C. Lang. Diagrammatic determinantal quantum Monte Carlo methods: Projective schemes and applications to the Hubbard-Holstein model. *Phys. Rev. B*, **76**:035116, Jul 2007.
- [51] T. A. Maier, M. S. Jarrell, and D. J. Scalapino. Structure of the Pairing Interaction in the Two-Dimensional Hubbard Model. *Phys. Rev. Lett.*, **96**:047005, Feb 2006.
- [52] H. B. Schüttler and D. J. Scalapino. Monte Carlo Studies of the Dynamics of Quantum Many-Body Systems. *Phys. Rev. Lett.*, **55**:1204–1207, Sep 1985.
- [53] H. B. Schüttler and D. J. Scalapino. Monte Carlo studies of the dynamical response of quantum many-body systems. *Phys. Rev. B*, **34**:4744–4756, Oct 1986.
- [54] S. R. White, D. J. Scalapino, R. L. Sugar, and N. E. Bickers. Monte Carlo calculation of dynamical properties of the two-dimensional Hubbard model. *Phys. Rev. Lett.*, **63**:1523–1526, Oct 1989.
- [55] Mark Jarrell and Ofer Biham. Dynamical approach to analytic continuation of quantum Monte Carlo data. *Phys. Rev. Lett.*, **63**:2504–2507, Nov 1989.
- [56] R. N. Silver, D. S. Sivia, and J. E. Gubernatis. Maximum-entropy method for analytic continuation of quantum Monte Carlo data. *Phys. Rev. B*, **41**:2380–2389, Feb 1990.
- [57] J.E. Gubernatis Mark Jarrell. Bayesian Inference and the Analytic Continuation of Imaginary-Time Quantum Monte Carlo Data. *Phys. Rep.*, **269**:133–195, May 1996.

- [58] Anders W. Sandvik. Stochastic method for analytic continuation of quantum Monte Carlo data. *Phys. Rev. B*, **57**:10287–10290, May 1998.
- [59] Sebastian Fuchs, Emanuel Gull, Matthias Troyer, Mark Jarrell, and Thomas Pruschke. Spectral properties of the three-dimensional Hubbard model. *Phys. Rev. B*, **83**:235113, Jun 2011.
- [60] R. K. Bryan. Maximum entropy analysis of oversampled data problems. *Eur. Biophys. J.*, **18**(3):165, 1990.
- [61] N. S. Vidhyadhiraja, A. Macridin, C. Sen, M. Jarrell, and Michael Ma. Quantum Critical Point at Finite Doping in the 2D Hubbard Model: A Dynamical Cluster Quantum Monte Carlo Study. *Phys. Rev. Lett.*, **102**(20):206407, May 2009.
- [62] S.-X. Yang, H. Fotso, S.-Q. Su, D. Galanakis, E. Khatami, J.-H. She, J. Moreno, J. Zaanen, and M. Jarrell. Proximity of the Superconducting Dome and the Quantum Critical Point in the Two-Dimensional Hubbard Model. *Phys. Rev. Lett.*, **106**:047004, 2011.
- [63] J. Labbè and J. Bok. Superconductivity in alkaline-earth-substituted La_2CuO_4 . *Europhys. Lett.*, **3**(22):1225–1230, 1987.
- [64] J. Friedel. On quasi one-dimensional or two-dimensional superconductors. *J. Phys. (Paris)*, **48**(10):1787–1797, 1987.
- [65] D. M. Newns, H. R. Krishnamurthy, P. C. Pattnaik, C. C. Tsuei, and C. L. Kane. Saddle-point pairing: An electronic mechanism for superconductivity. *Phys. Rev. Lett.*, **69**(8):1264–1267, Aug 1992.
- [66] R. S. Markiewicz. A survey of the van Hove scenario for high-Tc superconductivity with special emphasis on pseudogaps and striped phases. *J. Phys. Chem. Solids*, **58**:1179 – 1310, 1997.
- [67] D. S. Dessau, Z.-X. Shen, D. M. King, D. S. Marshall, L. W. Lombardo, P. H. Dickinson, A. G. Loeser, J. DiCarlo, C.-H Park, A. Kapitulnik, and W. E. Spicer. Key features in the measured band structure of $\text{Bi}_2\text{Sr}_2\text{CaCu}_2\text{O}_{8+\delta}$: Flat bands at E_F and Fermi surface nesting. *Phys. Rev. Lett.*, **71**(17):2781–2784, Oct 1993.
- [68] K. Gofron, J. C. Campuzano, A. A. Abrikosov, M. Lindroos, A. Bansil, H. Ding, D. Koelling, and B. Dabrowski. Observation of an "Extended" van Hove Singularity in $\text{YBa}_2\text{Cu}_4\text{O}_8$ by Ultrahigh Energy Resolution Angle-Resolved Photoemission. *Phys. Rev. Lett.*, **73**(24):3302–3305, Dec 1994.
- [69] A.A. Abrikosov, J.C. Campuzano, and K. Gofron. Experimentally observed extended saddle point singularity in the energy spectrum of $\text{YBa}_2\text{Cu}_3\text{O}_{6.9}$ and $\text{YBa}_2\text{Cu}_4\text{O}_8$ and some of the consequences. *Physica C: Superconductivity*, **214**(1-2):73 – 79, 1993.

- [70] J. C. Campuzano, K. Gofron, H. Ding, R. Liu, B. Dabrowski, and B. J. W. Veal. Photoemission from the high-Tc superconductors. *J. Low Temp. Phys.*, **95**:245–250, 1994.
- [71] D. M. King, Z. X. Shen, D. S. Dessau, D. S. Marshall, C. H. Park, W. E. Spicer, J. L. Peng, Z. Y. Li, and R. L. Greene. Observation of a Saddle-Point Singularity in $\text{Bi}_2(\text{Sr}_{0.97}\text{Pr}_{0.03})_2\text{CuO}_{6+\delta}$ and Its Implications for Normal and Superconducting State Properties. *Phys. Rev. Lett.*, **73**(24):3298–3301, Dec 1994.
- [72] A. Piriou, N. Jenkins, C. Berthod, I. Maggio-Aprile, and O. Fischer. First direct observation of the van Hove singularity in the tunnelling spectra of cuprates. *Nat. Commun.*, **2**:221, 2011.
- [73] J. L. McChesney, Aaron Bostwick, Taisuke Ohta, Thomas Seyller, Karsten Horn, J. González, and Eli Rotenberg. Extended van Hove Singularity and Superconducting Instability in Doped Graphene. *Phys. Rev. Lett.*, **104**(13):136803, Apr 2010.
- [74] P. C. Pattnaik, C. L. Kane, D. M. Newns, and C. C. Tsuei. Evidence for the van Hove scenario in high-temperature superconductivity from quasiparticle-lifetime broadening. *Phys. Rev. B*, **45**(10):5714–5717, Mar 1992.
- [75] D. M. Newns, C. C. Tsuei, R. P. Huebener, P. J. M. van Bentum, P. C. Pattnaik, and C. C. Chi. Quasiclassical Transport at a van Hove Singularity in Cuprate Superconductors. *Phys. Rev. Lett.*, **73**(12):1695–1698, Sep 1994.
- [76] C. C. Tsuei, D. M. Newns, C. C. Chi, and P. C. Pattnaik. Anomalous isotope effect and van Hove singularity in superconducting Cu oxides. *Phys. Rev. Lett.*, **65**(21):2724–2727, Nov 1990.
- [77] C. M. Varma, P. B. Littlewood, S. Schmitt-Rink, E. Abrahams, and A. E. Ruckenstein. Phenomenology of the normal state of Cu-O high-temperature superconductors. *Phys. Rev. Lett.*, **63**(18):1996–1999, Oct 1989.
- [78] P. Majumdar and H. R. Krishnamurthy. van Hove singularity effects in strongly correlated fermions. *cond-mat/9604057v1*, 1996.
- [79] F.F. Assaad and M. Imada. Unusually flat hole dispersion relation in the two-dimensional Hubbard model and restoration of coherence by addition of pair-hopping processes. *Eur. Phys. J. B*, **10**:595–598, 1999.
- [80] Masatoshi Imada, Atsushi Fujimori, and Yoshinori Tokura. Metal-insulator transitions. *Rev. Mod. Phys.*, **70**:1039–1263, 1998.
- [81] Elbio Dagotto, Alexander Nazarenko, and Massimo Boninsegni. Flat quasiparticle dispersion in the 2D t-J model. *Phys. Rev. Lett.*, **73**(5):728–731, Aug 1994.

- [82] D. M. Newns, P. C. Pattnaik, and C. C. Tsuei. Role of van Hove singularity in high-temperature superconductors: Mean field. *Phys. Rev. B*, **43**(4):3075–3084, Feb 1991.
- [83] S. Gopalan, O. Gunnarsson, and O. K. Andersen. Effects of saddle-point singularities on the electron lifetime. *Phys. Rev. B*, **46**:11798–11806, 1992.
- [84] R. J. Radtke and M. R. Norman. Relation of extended van Hove singularities to high-temperature superconductivity within strong-coupling theory. *Phys. Rev. B*, **50**(13):9554–9560, Oct 1994.
- [85] R. Hlubina and T. M. Rice. Resistivity as a function of temperature for models with hot spots on the Fermi surface. *Phys. Rev. B*, **51**(14):9253–9260, Apr 1995.
- [86] D. M. Newns, C. C. Tsuei, and P. C. Pattnaik. Van Hove scenario for d-wave superconductivity in cuprates. *Phys. Rev. B*, **52**(18):13611–13618, Nov 1995.
- [87] I. Dzyaloshinskii. Extended van-Hove Singularity and Related Non-Fermi Liquids. *J. Phys. I France*, **6**:119–135, 1996.
- [88] D. Djajaputra and J. Ruvalds. van Hove singularity effects in strongly correlated fermions. *cond-mat/9604057v1*, 1996.
- [89] R. G. Dias. Effects of van Hove singularities on the upper critical field. *J. Phys.: Condens. Matt.*, **12**(42):9053, 2000.
- [90] Christoph J. Halboth and Walter Metzner. Renormalization-group analysis of the two-dimensional Hubbard model. *Phys. Rev. B*, **61**(11):7364–7377, Mar 2000.
- [91] G. Kastelnakis. A Fermi liquid model for the overdoped and optimally doped cuprate superconductors: scattering rate, susceptibility, spin resonance peak and superconducting transition. *Physica C: Superconductivity*, **340**:119 – 132, 2000.
- [92] V. Y. Irkhin and A. A. Katanin. Violation of the Fermi-liquid picture in two-dimensional systems owing to van Hove singularities. *Phys. Rev. B*, **64**:205105–205111, 2001.
- [93] V. Y. Irkhin, A. A. Katanin, and M. I. Katsnelson. Robustness of the van Hove Scenario for High- T_c Superconductors. *Phys. Rev. Lett.*, **89**:076401, 2002.
- [94] K. G. Sandeman, G. G. Lonzarich, and A. J. Schofield. Ferromagnetic Superconductivity Driven by Changing Fermi Surface Topology. *Phys. Rev. Lett.*, **90**(16):167005, Apr 2003.
- [95] A. A. Katanin and A. P. Kampf. Quasiparticle Anisotropy and Pseudogap Formation from the Weak-Coupling Renormalization Group Point of View. *Phys. Rev. Lett.*, **93**:106406, 2004.

- [96] R. S. Markiewicz. Mode-coupling model of Mott gap collapse in the cuprates: Natural phase boundary for quantum critical points. *Phys. Rev. B*, **70**(17):174518, Nov 2004.
- [97] G. Kastelnakis. Quasiparticle scattering rate in overdoped superconducting cuprates. *Phys. Rev. B*, **71**:014520, 2005.
- [98] K. M. Shen, N. Kikugawa, C. Bergemann, L. Balicas, F. Baumberger, W. Meevasana, N. J. C. Ingle, Y. Maeno, Z.-X. Shen, and A. P. Mackenzie. Evolution of the Fermi Surface and Quasiparticle Renormalization through a van Hove Singularity in $\text{Sr}_{2-y}\text{La}_y\text{RuO}_4$. *Phys. Rev. Lett.*, **99**(18):187001, Oct 2007.
- [99] Takasada Shibauchi, Lia Krusin-Elbaum, Masashi Hasegawa, Yuichi Kasahara, Ryuji Okazaki, and Yuji Matsuda. Field-induced quantum critical route to a Fermi liquid in high-temperature superconductors. *Proc. Natl. Acad. Sci. U.S.A.*, **105**(20):7120–7123, 2008.
- [100] A. Tamai, M. P. Allan, J. F. Mercure, W. Meevasana, R. Dunkel, D. H. Lu, R. S. Perry, A. P. Mackenzie, D. J. Singh, Z.-X. Shen, and F. Baumberger. Fermi surface and van Hove Singularities in the Itinerant Metamagnet $\text{Sr}_3\text{Ru}_2\text{O}_7$. *Phys. Rev. Lett.*, **101**(2):026407, Jul 2008.
- [101] Rok Žitko, Janez Bonča, and Thomas Pruschke. Van Hove singularities in the paramagnetic phase of the Hubbard model: DMFT study. *Phys. Rev. B*, **80**:245112, 2009.
- [102] A. Katanin. Quantum critical behavior of antiferromagnetic itinerant systems with van Hove singularities. *Phys. Rev. B*, **81**:165118, 2010.
- [103] S. Schmitt. Non-Fermi-liquid signatures in the Hubbard model due to van Hove singularities. *Phys. Rev. B*, **82**:155126, 2010.
- [104] S. Chakraborty, D. Galanakis, and P. Phillips. Emergence of particle-hole symmetry near optimal doping in high-temperature copper oxide superconductors. *Phys. Rev. B*, **82**:214503, 2010.
- [105] H. J. Trodahl. Thermopower of the superconducting cuprates. *Phys. Rev. B*, **51**:6175–6178, 1995.
- [106] Y. Ando, S. Komiyama, K. Segawa, S. Ono, and Y. Kurita. Electronic Phase Diagram of High- T_c Cuprate Superconductors from a Mapping of the In-Plane Resistivity Curvature. *Phys. Rev. Lett.*, **93**:267001, 2004.
- [107] R. Daou, N. Doiron-Leyraud, David LeBoeuf, S. Y. Li, F. Laliberte, O. Cyr-Choiniere, Y. J. Jo, L. Balicas, J.-Q. Yan, J.-S. Zhou, J. B. Goodenough, and L. Taillefer. Linear temperature dependence of resistivity and change in the Fermi surface at the pseudogap critical point of a high- T_c superconductor. *Nat. Phys.*, **5**:31, 2009.

- [108] R. A. Cooper, Y. Wang, B. Vignolle, O. J. Lipscombe, S. M. Hayden, Y. Tanabe, T. Adachi, Y. Koike, M. Nohara, H. Takagi, Cyril Proust, and N. E. Hussey. Anomalous Criticality in the Electrical Resistivity of $\text{La}_{2-x}\text{Sr}_x\text{CuO}_4$. *Science*, **323**:603–607, 2009.
- [109] M. Gurvitch and A. T. Fiory. Resistivity of $\text{La}_{1.825}\text{Sr}_{0.175}\text{CuO}_4$ and $\text{YBa}_2\text{Cu}_3\text{O}_7$ to 1100K: Absence of saturation and its implications. *Phys. Rev. Lett.*, **59**:1337–1340, 1987.
- [110] B. Wuyts, V. V. Moshchalkov, and Y. Bruynseraede. Resistivity and Hall effect of metallic oxygen-deficient $\text{YBa}_2\text{Cu}_3\text{O}_x$ films in the normal state. *Phys. Rev. B*, **53**:9418–9432, 1996.
- [111] C. Uher, A. B. Kaiser, E. Gmelin, and L. Walz. Electronic transport in highly doped $\text{La}_{2-x}\text{Sr}_x\text{CuO}_4$ superconductors. *Phys. Rev. B*, **36**:5676–5679, 1987.
- [112] A. J. Schofield. Non-Fermi liquids. *Contemporary Physics*, **40**:95–115, 1999.
- [113] X. F. Sun, Seiki Komiyama, and Yoichi Ando. Heat transport of $\text{La}_{2-y}\text{Eu}_y\text{CuO}_4$ and $\text{La}_{1.88-y}\text{Eu}_y\text{Sr}_{0.12}\text{CuO}_4$ single crystals. *Phys. Rev. B*, **67**:184512, 2003.
- [114] R. K. Williams, J. O. Scarbrough, J. M. Schmitz, and J. R. Thompson. Thermal conductivity of polycrystalline $\text{YBa}_2\text{Cu}_4\text{O}_8$ from 10 to 300K. *Phys. Rev. B*, **57**:10923–10928, 1998.
- [115] M. Gurvitch, J. M. Valles, A. M. Cucolo, R. C. Dynes, J. P. Garno, L. F. Schneemeyer, and J. V. Waszczak. Reproducible tunneling data on chemically etched single crystals of $\text{YBa}_2\text{Cu}_3\text{O}_7$. *Phys. Rev. Lett.*, **63**(9):1008–1011, Aug 1989.
- [116] F. Steglich. *High temperature superconductors and Materials and mechanisms of superconductivity*, page 1010. North Holland, Amsterdam, 1988.
- [117] G. Wiedemann and R. Franz. *Ann. Phys.*, **89**:497–531, 1853.
- [118] Xin Wang, Emanuel Gull, Luca de’ Medici, Massimo Capone, and Andrew J. Millis. Antiferromagnetism and the gap of a Mott insulator: Results from analytic continuation of the self-energy. *Phys. Rev. B*, **80**:045101, 2009.
- [119] M. H. Hettler, A. N. Tahvildar-Zadeh, M. Jarrell, T. Pruschke, and H. R. Krishnamurthy. Nonlocal dynamical correlations of strongly interacting electron systems. *Phys. Rev. B*, **58**:R7475–R7479, 1998.
- [120] N. Blümer. Efficiency of quantum Monte Carlo impurity solvers for the dynamical mean-field theory. *Phys. Rev. B*, **76**(20):205120, Nov 2007.
- [121] J. E. Hirsch and R. M. Fye. Monte Carlo Method for Magnetic Impurities in Metals. *Phys. Rev. Lett.*, **56**:2521–2524, 1986.

- [122] M. Jarrell, Th. Maier, C. Huscroft, and S. Moukouri. Quantum Monte Carlo algorithm for nonlocal corrections to the dynamical mean-field approximation. *Phys. Rev. B*, **64**:195130, 2001.
- [123] C. M. Varma, Z. Nussinov, and W. van Saarloos. Singular or non-Fermi liquids. *Phys. Rep.*, **361**:267 – 417, 2002.
- [124] R. Kubo. *Lectures in Theoretical Physics*, volume **1**, page 120. New York, Interscience, 1959.
- [125] J. A. Stroscio and P. Lipavský. Thermopower in scanning-tunneling-microscope experiments. *Phys. Rev. B*, **42**(14):9214–9216, Nov 1990.
- [126] A. C. Hewson. *The Kondo Problem to Heavy Fermions*. Cambridge University Press, Cambridge, 1993.
- [127] R. S. Markiewicz, S. Sahrakorpi, and A. Bansil. Paramagnon-induced dispersion anomalies in the cuprates. *Phys. Rev. B*, **76**(17):174514, Nov 2007.
- [128] K. Mielson, E. Khatami, D. Galanakis, A. Macridin, J. Moreno, and M. Jarrell. Thermodynamics of the quantum critical point at finite doping in the two-dimensional Hubbard model studied via the dynamical cluster approximation. *Phys. Rev. B*, **80**:140505, 2009.
- [129] A. Kaminski, S. Rosenkranz, H. M. Fretwell, M. R. Norman, M. Randeria, J. C. Campuzano, J-M. Park, Z. Z. Li, and H. Raffy. Change of Fermi surface topology in $\text{Bi}_2\text{Sr}_2\text{CaCu}_2\text{O}_{8+\delta}$ with doping. *Phys. Rev. B*, **73**:174511, 2006.
- [130] A. Bansil and M. Lindroos. Matrix Element Effects In The Angle-Resolved Photoemission Spectrum Of BISCO. *J. Phys. Chem. Solids*, **59**:1879 – 1883, 1998.
- [131] A. Bansil and M. Lindroos. Importance of Matrix Elements in the ARPES Spectra of BISCO. *Phys. Rev. Lett.*, **83**:5154–5157, 1999.
- [132] T. Dahm, L. Tewordt, and S. Wernbter. Spin mode, electrical resistivity, and thermal conductivity for the two-dimensional Hubbard model. *Phys. Rev. B*, **49**:748–751, 1994.
- [133] A. Macridin, M. Jarrell, and Th. Maier. Phase separation in the Hubbard model using the dynamical cluster approximation. *Phys. Rev. B*, **74**:085104, 2006.
- [134] E. Khatami, K. Mielson, D. Galanakis, A. Macridin, J. Moreno, R. T. Scalettar, and M. Jarrell. Quantum criticality due to incipient phase separation in the two-dimensional Hubbard model. *Phys. Rev. B*, **81**:201101, 2010.
- [135] Masatoshi Imada. Universality classes of metal-insulator transitions in strongly correlated electron systems and mechanism of high-temperature superconductivity. *Phys. Rev. B*, **72**:075113, 2005.

- [136] Takahiro Misawa, Youhei Yamaji, and Masatoshi Imada. Quantum Critical “Opalescence” around Metal–Insulator Transitions. *J. Phys. Soc. Jpn*, **75**:083705, 2006.
- [137] Youhei Yamaji, Takahiro Misawa, and Masatoshi Imada. Quantum and Topological Criticalities of Lifshitz Transition in Two-Dimensional Correlated Electron Systems. *J. Phys. Soc. Jpn*, **75**:094719, 2006.
- [138] Takahiro Misawa and Masatoshi Imada. Quantum criticality around metal-insulator transitions of strongly correlated electron systems. *Phys. Rev. B*, **75**:115121, 2007.
- [139] Youhei Yamaji, Takahiro Misawa, and Masatoshi Imada. Quantum Metamagnetic Transitions Induced by Changes in Fermi-Surface Topology: Applications to a Weak Itinerant-Electron Ferromagnet ZrZn_2 . *J. Phys. Soc. Jpn*, **76**:063702, 2007.
- [140] Masatoshi Imada, Takahiro Misawa, and Youhei Yamaji. Unconventional quantum criticality emerging as a new common language of transition-metal compounds, heavy-fermion systems, and organic conductors. *J. Phys.: Condens. Matter*, **22**:164206, 2010.
- [141] M. R. Norman, Jie Lin, and A. J. Millis. Lifshitz transition in underdoped cuprates. *Phys. Rev. B*, **81**:180513, 2010.
- [142] Christoph J. Halboth and Walter Metzner. d -Wave Superconductivity and Pomeranchuk Instability in the Two-Dimensional Hubbard Model. *Phys. Rev. Lett.*, **85**:5162–5165, 2000.
- [143] Hiroyuki Yamase, Vadim Oganesyan, and Walter Metzner. Mean-field theory for symmetry-breaking Fermi surface deformations on a square lattice. *Phys. Rev. B*, **72**:035114, 2005.
- [144] Andrea Damascelli, Zahid Hussain, and Zhi-Xun Shen. Angle-resolved photoemission studies of the cuprate superconductors. *Rev. Mod. Phys.*, **75**:473–541, Apr 2003.
- [145] B. Vignolle, A. Carrington, R. A. Cooper, M. M. J. French, A. P. Mackenzie, C. Jaudet, D. Vignolles, Cyril Proust, and N. E. Hussey. Quantum oscillations in an overdoped high- T_c superconductor. *Nature*, **455**:952, 2008.
- [146] M. R. Norman, H. Ding, M. Randeria, J. C. Campuzano, T. Yokoya, T. Takeuchi, T. Takahashi, T. Mochiku, K. Kadowaki, P. Guptasarma, and D. G. Hinks. Destruction of the Fermi surface in underdoped high- T_c superconductors. *Nature (London)*, **392**:157, 1998.
- [147] H.-B. Yang, J. D. Rameau, T. A. Johnson, P. D. and Valla, Tsvelik, and G. D. Gu. Emergence of preformed Cooper pairs from the doped Mott insulating state in $\text{Bi}_2\text{Sr}_2\text{CaCu}_2\text{O}_{8+\delta}$. *Nature*, **456**:77, 2008.
- [148] H.-B. Yang, J. D. Rameau, Z.-H. Pan, G. D. Gu, P. D. Johnson, H. Claus, D. G. Hinks, and T. E. Kidd. Reconstructed Fermi Surface of Underdoped $\text{Bi}_2\text{Sr}_2\text{CaCu}_2\text{O}_{8+\delta}$ Cuprate Superconductors. *Phys. Rev. Lett.*, **107**:047003, Jul 2011.

- [149] David LeBoeuf, Nicolas Doiron-Leyraud, Julien Levallois, R. Daou, J.-B. Bonnemaïson, N. E. Hussey, L. Balicas, B. J. Ramshaw, Ruixing Liang, D. A. Bonn, W. N. Hardy, S. Adachi, Cyril Proust, and Louis Taillefer. Electron pockets in the Fermi surface of hole-doped high- T_c superconductors. *Nature*, **450**:533, 2007.
- [150] S. E. Sebastian, N. Harrison, M. M. Altarawneh, C. H. Mielke, Ruixing Liang, D. A. Bonn, W. N. Hardy, and G. G. Lonzarich. Metal-insulator quantum critical point beneath the high- T_c superconducting dome. *Proceedings of the National Academy of Sciences*, **107**:6175–6179, 2010.
- [151] I. M. Lifshitz. Neutrino electrodynamics and possible consequences for solar neutrinos. *Sov. Phys. JETP*, **11**:1130, 1960.
- [152] Yoshihiko Okamoto, Atsushi Nishio, and Zenji Hiroi. Discontinuous Lifshitz transition achieved by band-filling control in Na_xCoO_2 . *Phys. Rev. B*, **81**:121102, Mar 2010.
- [153] M. Imada, Y. Yamaji, S. Sakai, and Y. Motome. Theory of pseudogap and superconductivity in doped Mott insulators. *Ann. Phys.*, **523**:629, 2011.
- [154] M. Bercx and F. F. Assaad. Metamagnetism and Lifshitz transitions in models for heavy fermions. *Phys. Rev. B*, **86**:075108, Aug 2012.
- [155] S. G. Ovchinnikov, M. M. Korshunov, and E. I. Shneyder. Lifshitz quantum phase transitions and rearrangement of the Fermi surface upon a change in the hole concentration in high-temperature superconductors. *JETP*, **109**:775, 2009.
- [156] Andreas Hackl and Matthias Vojta. Zeeman-Driven Lifshitz Transition: A Model for the Experimentally Observed Fermi-Surface Reconstruction in YbRh_2Si_2 . *Phys. Rev. Lett.*, **106**:137002, 2011.
- [157] A. Macridin, M. Jarrell, and Th. Maier. Phase separation in the Hubbard model using the dynamical cluster approximation. *Phys. Rev. B*, **74**:085104, Aug 2006.
- [158] D. Galanakis, E. Khatami, K. Mielsons, A. Macridin, J. Moreno, D. A. Browne, and M. Jarrell. Quantum criticality and incipient phase separation in the thermodynamic properties of the Hubbard model. *Phil. Trans. R. Soc. A*, **369**:1670, 2011.
- [159] C. M. Varma, P. B. Littlewood, S. Schmitt-Rink, E. Abrahams, and A. E. Ruckenstein. Phenomenology of the normal state of Cu-O high-temperature superconductors. *Phys. Rev. Lett.*, **63**:1996–1999, Oct 1989.
- [160] C. M. Varma. Pseudogap Phase and the Quantum-Critical Point in Copper-Oxide Metals. *Phys. Rev. Lett.*, **83**:3538–3541, Oct 1999.
- [161] Emanuel Gull, Olivier Parcollet, Philipp Werner, and Andrew J. Millis. Momentum-sector-selective metal-insulator transition in the eight-site dynamical mean-field approximation to the Hubbard model in two dimensions. *Phys. Rev. B*, **80**:245102, Dec 2009.

- [162] Philipp Werner, Emanuel Gull, Olivier Parcollet, and Andrew J. Millis. Momentum-selective metal-insulator transition in the two-dimensional Hubbard model: An 8-site dynamical cluster approximation study. *Phys. Rev. B*, **80**:045120, Jul 2009.
- [163] Nan Lin, Emanuel Gull, and Andrew J. Millis. Physics of the pseudogap in eight-site cluster dynamical mean-field theory: Photoemission, Raman scattering, and in-plane and c -axis conductivity. *Phys. Rev. B*, **82**:045104, Jul 2010.
- [164] E. Gull, M. Ferrero, O. Parcollet, A. Georges, and A. J. Millis. Momentum-space anisotropy and pseudogaps: A comparative cluster dynamical mean-field analysis of the doping-driven metal-insulator transition in the two-dimensional Hubbard model. *Phys. Rev. B*, **82**:155101, Oct 2010.
- [165] Gabriel Kotliar, Sergej Y. Savrasov, Gunnar Pálsson, and Giulio Biroli. Cellular Dynamical Mean Field Approach to Strongly Correlated Systems. *Phys. Rev. Lett.*, **87**:186401, Oct 2001.
- [166] Shiro Sakai, Yukitoshi Motome, and Masatoshi Imada. Evolution of Electronic Structure of Doped Mott Insulators: Reconstruction of Poles and Zeros of Green's function. *Phys. Rev. Lett.*, **102**:056404, Feb 2009.
- [167] Ansgar Liebsch and Ning-Hua Tong. Finite-temperature exact diagonalization cluster dynamical mean-field study of the two-dimensional Hubbard model: Pseudogap, non-Fermi-liquid behavior, and particle-hole asymmetry. *Phys. Rev. B*, **80**:165126, Oct 2009.
- [168] G. Sordi, K. Haule, and A.-M. S. Tremblay. Mott physics and first-order transition between two metals in the normal-state phase diagram of the two-dimensional Hubbard model. *Phys. Rev. B*, **84**:075161, Aug 2011.
- [169] Shiro Sakai, Yukitoshi Motome, and Masatoshi Imada. Doped high- T_c cuprate superconductors elucidated in the light of zeros and poles of the electronic Green's function. *Phys. Rev. B*, **82**:134505, Oct 2010.
- [170] Shiro Sakai, Giorgio Sangiovanni, Marcello Civelli, Yukitoshi Motome, Karsten Held, and Masatoshi Imada. Cluster-size dependence in cellular dynamical mean-field theory. *Phys. Rev. B*, **85**:035102, Jan 2012.
- [171] J. E. Hirsch and D. J. Scalapino. Enhanced Superconductivity in Quasi Two-Dimensional Systems. *Phys. Rev. Lett.*, **56**:2732–2735, Jun 1986.
- [172] Tudor D. Stanescu and Gabriel Kotliar. Fermi arcs and hidden zeros of the Green function in the pseudogap state. *Phys. Rev. B*, **74**:125110, Sep 2006.
- [173] The cumulant interpolation scheme yields the hole pocket in the underdope region [166, 169, 170], the corresponding Lifshitz transition from Fermi liquid to pseudogap will be a "pocket-vanishing" type different from our findings of "neck-collapsing" type with

self energy interpolation scheme. But the two schemes yield transitions at the same critical filling n_c .

- [174] Jouko Nieminen, Ilpo Suominen, Tanmoy Das, R. S. Markiewicz, and A. Bansil. Evidence of strong correlations at the van Hove singularity in the scanning tunneling spectra of superconducting $\text{Bi}_2\text{Sr}_2\text{CaCu}_2\text{O}_{8+\delta}$ single crystals. *arXiv:1205.5540*, 2012.
- [175] Jian-Huang She and Jan Zaanen. BCS superconductivity in quantum critical metals. *Phys. Rev. B*, **80**:184518, Nov 2009.
- [176] Alexandru Macridin, M. Jarrell, Thomas Maier, and D. J. Scalapino. High-Energy Kink in the Single-Particle Spectra of the Two-Dimensional Hubbard Model. *Phys. Rev. Lett.*, **99**:237001, Dec 2007.
- [177] S.-X. Yang, H. Fotsos, H. Hafermann, K.-M. Tam, J. Moreno, T. Pruschke, and M. Jarrell. Dual fermion dynamical cluster approach for strongly correlated systems. *Phys. Rev. B*, **84**:155106, Oct 2011.
- [178] A. N. Rubtsov, M. I. Katsnelson, A. I. Lichtenstein, and A. Georges. Dual fermion approach to the two-dimensional Hubbard model: Antiferromagnetic fluctuations and Fermi arcs. *Phys. Rev. B*, **79**:045133, Jan 2009.
- [179] Th. A. Maier, Th. Pruschke, and M. Jarrell. ARPES Spectra of the Hubbard model. *Phys. Rev. B*, **66**:075102/1–8, 2002.
- [180] Sen Zhou and Ziqiang Wang. *Phys. Rev. Lett.*, **100**:217002, May 2008.
- [181] W. Hanke M. L. Kiesel, C. Platt and R. Thomale. Anisotropic chiral $d + id$ superconductivity in $\text{Na}_x\text{CoO}_2\text{yH}_2\text{O}$. *arXiv:1301.5662*, 2013.
- [182] Guo-qing Zheng, Kazuaki Matano, D. P. Chen, and C. T. Lin. Spin singlet pairing in the superconducting state of $\text{Na}_x\text{CoO}_2\cdot 1.3\text{H}_2\text{O}$: Evidence from a ^{59}Co knight shift in a single crystal. *Phys. Rev. B*, **73**:180503, May 2006.
- [183] R.L. Meng J. Cmaidalka G.-q. Zheng, K. Matano and C.W. Chu. *J. Phys.: Condens. Matter*, **18**:L63, 2006.
- [184] G. Baskaran. Electronic Model for CoO_2 Layer Based Systems: Chiral Resonating Valence Bond Metal and Superconductivity. *Phys. Rev. Lett.*, **91**:097003, Aug 2003.
- [185] Qiang-Hua Wang, Dung-Hai Lee, and Patrick A. Lee. *Phys. Rev. B*, **69**:092504, Mar 2004.
- [186] K. Miyake, S. Schmitt-Rink, and C. M. Varma. Spin-fluctuation-mediated even-parity pairing in heavy-fermion superconductors. *Phys. Rev. B*, **34**:6554–6556, Nov 1986.
- [187] D. J. Scalapino, E. Loh, and J. E. Hirsch. d -wave pairing near a spin-density-wave instability. *Phys. Rev. B*, **34**:8190–8192, Dec 1986.

- [188] Carsten Honerkamp. Instabilities of interacting electrons on the triangular lattice. *Phys. Rev. B*, **68**:104510, Sep 2003.
- [189] Robert Joynt and Louis Taillefer. The superconducting phases of UPt_3 . *Rev. Mod. Phys.*, **74**:235–294, Mar 2002.
- [190] V. Kuznetsova and V. Barzykin. Pairing state in multicomponent superconductors. *Europhysics Letters*, **72**:437, 2005.

Appendix

Permissions

"The author has the right to use the article or a portion of the article in a thesis or dissertation without requesting permission from APS, provided the bibliographic citation and the APS copyright credit line are given on the appropriate pages."

Quoted from the website of the American Physical Society (APS).

Publication List

1. *Role of the van Hove Singularity in the Quantum Criticality of the Hubbard Model*, K.-S. Chen, S. Pathak, S.-X. Yang, S.-Q. Su, D. Galanakis, K. Mikelsons, M. Jarrell, J. Moreno, Phys. Rev. B **84**, 245107 (2011)
2. *Dynamical Cluster Approximation*, H. Fotsos, S. Yang, K. Chen, S. Pathak, J. Moreno, M. Jarrell, K. Mikelsons, E. Khatami, and D. Galanakis, in Strongly Correlated Systems: Theoretical methods, Springer Series in Solid-State Sciences, Ed: Adolfo Avella and Ferdinando Mancini (2011).
3. *Lifshitz Transition in Two-dimensional Hubbard Model*, Kuang-Shing Chen, Zi Yang Meng, Thomas Pruschke, Juana Moreno, Mark Jarrell, Phys. Rev. B **86**, 165136 (2012)
4. *Unconventional Superconductivity on the Triangular Lattice Hubbard Model*, Kuang Shing Chen, Zi Yang Meng, Unjong Yu, Shuxiang Yang, Mark Jarrell, and Juana Moreno, arxiv:1304.7739

Vita

Kuang-Shing Chen was born in 1982 in Taipei Taiwan. He obtained his Bachelor's degree in 2004 and his master degree in physics in 2006 at National Taiwan University. After serving the mandatory military service in the Army Band of Taiwan for one year and one month, he got a job of research assistant in physics in Academia Sinica in Taiwan. Then he went to University of Cincinnati in September 2008 to pursue the PhD degree in physics. In January 2009 he moved to Louisiana State University to continue his PhD training with prof. Mark Jarrell . He is currently a candidate for the degree of Doctor of Philosophy in physics, which will be awarded in the summer of 2013.